Universidade de Santiago de Compostela

Departamento de Física de Partículas

Software development and Performance Analysis of the HADES Resistive Plate Chamber Time-of-Flight Detector at GSI

PABLO CABANELAS EIRAS

Santiago de Compostela,

Xaneiro de 2011

Universidade de Santiago de Compostela

Departamento de Física de Partículas

Software development and Performance Analysis of the HADES Resistive Plate Chamber Time-of-Flight Detector at GSI

PABLO CABANELAS EIRAS

Santiago de Compostela,

Xaneiro de 2011

UNIVERSIDADE DE SANTIAGO DE COMPOSTELA

D. JUAN ANTONIO GARZON HEYDT, PROFESOR TITULAR DO DEPARTAMENTO DE FISICA DE PARTICULAS DA UNIVERSIDADE DE SANTIAGO DE COMPOSTELA,

CERTIFICA:

que a tese titulada:

Software development and Performance Analysis of the HADES Resistive Plate Chamber Time-of-Flight Detector at GSI

foi realizada por **D. PABLO CABANELAS EIRAS** no **LabCAF** do Departamento de Física de Partículas da Universidade de Santiago de Compostela baixo a súa dirección, para acadar o título de Doutor en Física

Santiago de Compostela,
Xaneiro de 2011

Juan Antonio Garzón Heydt
Departamento de Física de Partículas

Contents

List of Figures

List of Tables

Resumo

A Colaboracion HADES é un dos proxectos máis ambiciosos do centro de investigación e acelerador de iós pesados GSI, en Darmstadt, Alemaña. O Espectrómetro HADES (High Acceptance DiElectron Spectrometer) foi concebido para estudiar materia nuclear densa a través de parellas de di-leptóns procedentes da desintegración de mesóns vectoriais lixeiros producidos en colisións núcleo-núcleo.

Dentro dos seus resultados mais importantes, cabe salientar a confirmación experimental do chamado "puzle de DLS" e do incremento de masa dos mesóns vectoriais dentro de materia nuclear densa [1]. Ademáis, foron medidas por primeira vez nun mesmo experimento as propiedades dos mesóns vectoriais e dos mesóns escalares cargados K^+ e K^- [2].

Estes resultados abriron novas expectativas en HADES, e unha mellora do Spectrómetro foi proposta, aceptada e levada a cabo nos últimos anos. Dentro desa mellora do experimento orixinal, a colaboración pretende estudiar colisións de ións pesados ata Au+Au a enerxías cinéticas da orde de 1.5 *A*GeV. Un dos principais piares nos que se apoia dita mellora é a construcción e instalación dun novo detector de tempo de voo a baixos ángulos. Este novo muro de tempo de voo está basado en detectores de Placas Resistivas para medida de tempos ou "timing Resistive Plate Chambers" (tRPCs), un tipo de detectores de ionización gaseosa que está collendo moito pulo nos últimos anos dentro da Física de Partículas e Altas Enerxías. Outras melloras de consideración foron o desenvolvemento de novas Camaras de Deriva e un novo e completo sistema de adquisición de datos.

O traballo que se presento nesta tese forma parte desde proxecto de mellora, e máis concretamente céntrase no desenvolvemento do novo muro de tRPCs, a escritura do seu software de reconstrucción e a análise das súas prestacións.

Tendo en conta as características do Espectrómetro HADES, a nova tRPC debe cumplir os seguintes requisitos:

- Cubrir unha area efectiva de aproximadamente 8 m^2, dividida en 6 partes iguais ou sectores.
- Un nivel de ocupación por debaixo do 20 % en colisións de máxima multiplicidade, e unha alta granularidade.
- Alta capacidade de taxa (ata 1 kHz/cm^2).
- Unha resolución temporal homoxénea por debaixo de 100 ps, cunha baixa presencia de colas e interferencia entre canais (*crosstalk*)
- Alta eficiencia intrínseca e xeométrica, cercana ó 100 %
- Unha electrónica de amplificación e lectura robusta, rápida e compacta
- Un programa (ou *software*) de reconstrucción integrado no experimento

A tRPC de HADES foi diseñada e construida para satisfacer estes requerimentos. Cada un dos seus seis sectores consta de 187 celdas de tRPCs de 4 gaps de 270 μm de espesor (o que asegura alta eficiencia), con vidro como material resistivo (o que permite traballar a taxas altas), doble lectura (o que incrementa a fiabilidade e permite a reconstrucción da posición a partir da diferencia entre as dúas medidas), e dispostas nunha configuración de dúas capas, con tres columnas de celdas por capa, evitando así as posibles zonas mortas (cubrindo prácticamente toda a eficiencia xeométrica). En total, están operativas 1122 celdas the tRPCs e 2244 canais de lectura. A electrónica de adquisición está separada en tres etapas (ou tarxetas): unha primeira etapa de amplificación e dixitalización (a “daughterboard” ou DB), unha segunda

etapa para regulación e transporte de sinais de datos e trigger (a "motherboard" ou MB), e unha ultima etapa de conversión a través de TDCs (Time to Digital Converters) (a "Trigger and Readout Board" ou TRB).

O *software* de reconstrucción para a tRPC foi deseñado e escrito en C++. Está completamente integrado na estructura do experimento. Este *software* realiza dende as tarfas máis básicas ata as máis elaboradas: a reconstrucción comenza co desenpaquetado daqueles datos obtidos polos TDCs (ou *raw data*), que son transformados a valores numéricos, chegando así ó nivel de datos *Raw*; posteriormente, todos este valores numéricos son calibrados de forma que teñan xa unidades físicas alcanzando o nivel de datos *Cal*. Todos os algoritmos necesarios para a completa calibración da tRPC foron desenvolvidos, escritos e probados con datos reais. Foi calibrada a posición, a carga e o tempo de voo; finalmente, a partires destes valores xa calibrados, faise a propia reconstrucción do suceso na tRPC, asignándolle unha posición física dentro do muro e o seu correspondente tempo de voo ("time-of-flight" ou *tof*), entre outras, chegando ó nivel de datos *Hit*. Ademáis, foi escrito tamén un último nivel de datos da tRPC, chamado nivel *Cluster*, no que, mediante un certo algoritmo, se buscan aqueles eventos que deron sinal en dúas celdas xeométricamente solapadas. A partires de esta información, os programas de reconstrucci'on de traxectorias e momentos do experimento chegan ata a información máis básica da partícula.

A tRPC foi evolucionando no seu deseño preliminar ata chagar á súa situaci'on final, onde os seis sectores están xa plenamente integrados en instalados en HADES, preparados para facer Física con eles. Esta evolución pasou por diferentes etapas, nos que os diferentes obxetivos foron alcanzados:

Antes da construcción definitiva, foi construido o prototipo dun sector e probado baixo condicións realistas dentro de HADES, instrumentado cunha versión da electrónica moi similar á definitiva. Os resultados con este prototipo foron moi prometedores, amosando un comportamento moi estable ata altas taxas, alta eficiencia ($\sim$99 %), baixo nivel de ruído e *crosstalk* ($<$1 %) e unha resolución temporal de 77 ps despois das correccións, ben por debaixo do requerimento inicial.

Posteriormente, foi ralizado un experimento no que varias celdas de tRPCs, perfectamente instaladas dentro dunha caixa espcialmente dedicada, traballaron en condicións nominais de alta tensión e fluxo de gas, expostas a feixes de protóns, C^{12} e os seus productos. Así, foron verificadas as súas prestacións para a detección de ións ata Z=6. Foi estudiado o seu comportamento e demostrouse a súa capacidade de identificación a partir das medidas da carga depositada na tRPC. Ademáis, a súa eficiencia foi medida para cada unha das especies amosando unha eficiencia compatible con 100 % para alta Z, mentres que para partículas mínimamente ionizantes (*mips*) coma protóns ou raios cósmicos, esta eficiencia baixou ata niveles do 90 %. Nembargantes, a resolución temporal mantívose sempre por debaixo dos 100 ps independentemente da especie identificada, incluso a altas taxas de radiación.

Unha vez que os sectores definitivos foron construidos, acondicionáronse e validáronse en varias probas realizadas no GSI ó longo de 2009. Os sectores, agrupados de dous en dous, foron colocados horizontalmente, completamente instrumentados coa electrónica, adquisición e fontes de alimentación definitivas, e tomáronse datos de raios cósmicos durante largos períodos de tempo. Obtívose unha resolución temporal media de 80 ps despois da correccións, cun comportamento moi homoxéneo en cada unha das celdas. Comprobouse a mecánica e a estabilidade de todo o sistema baixo períodos prolongados de funcionamento. Finalmente, en Novembro de 2009, os seis sectores con toda a súa instrumentación foron instalados na súa posición nominal dentro do espectrómetro HADES.

A partires de Xullo de 2010, comenzou a verificación definitiva, ou o chamado *commissioning*, no que a tRPC, e outros novos compoñentes da mellora de HADES, foron probados por primeira vez baixo feixes de ións pesados (Ca, Ni, Au e U) a altas intensidades sobre un branco de Au, con e sin campo magnético.

A análise de todos estes datos amosou unha vez máis as execeltes prestacións e a estabilidade da tRPC. A tRPC foi completamente calibrada, o seu comportamento foi estudiado en profundidade, e mantívose a resolución temporal por debaixo dos 100 ps e alta eficiencia.

Gracias ó sistema de recostrucción de traxectorias de HADES a través de Cámaras de Deriva, foi medida a eficiencia de reconstrucción da tRPC en toda a súa área, obténdose un valor medio próximo ó 95 % e unha resolución e posición de preto de 14 mm.

Por primeira vez, tomáronse datos da tRPC baixo campo magnético intenso en HADES, e iniciouse un proceso de análise completo dos datos (*dst*) no que se executan todos os algoritmos e obtéñense os resultados finais. Un dos obxetivos desta *dst* é facer nova física con alta resolución temporal. Para iso, é necesario contar cunha calibración óptima de todos os detectores, principalmente daqueles con medida de *tof*, o que permite a identificación das partículas a partir do seu momento e a súa velocidade. A tRPC foi, unha vez máis, calibrada e esta identificación foi feita recentemente por primeira vez coa tRPC. Nesta primeira toma de contacto obtivéronse resultados moi prometedores, coma se amosa na figura que acompaña este resumo, de cara a futuras tomas de datos e an'alise profundo da física.

Como conclusión final, pódese afirmar que, despois de cinco anos de evolución e desenvolvemento, o muro de tRPCs de HADES está plenamente operativo, con moi boas prestacións, satisfacendo os requerimentos esixidos e esperando para axudar a facer nova e interesante física en HADES.

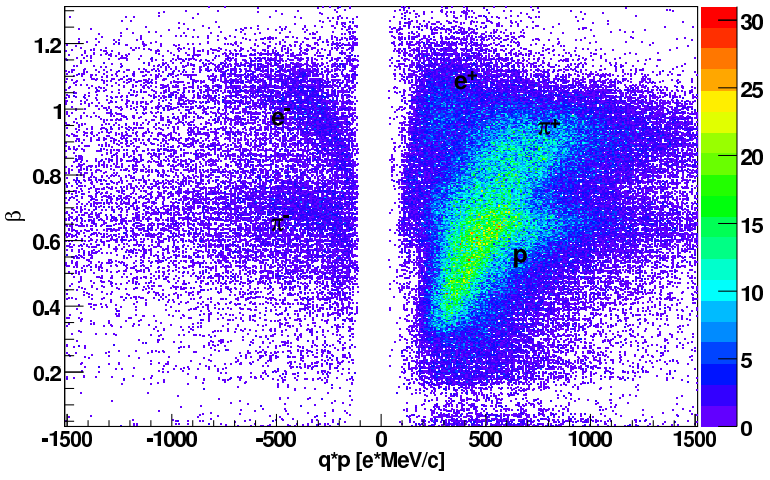

(a)

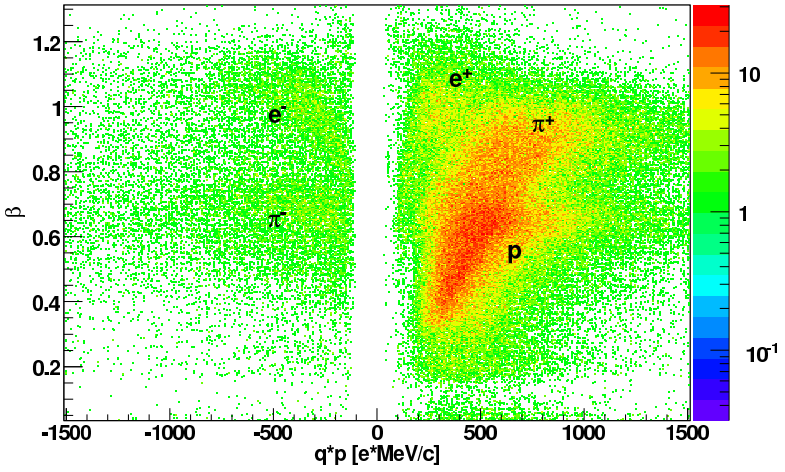

(b)

Figura R.1: Figura do momento multilicado pola polaridade (carga) en función da velocidade β para datos con campo magnético intenso medidos coa tRPC, en escala lineal (a) e logarítmica (b). As especies Protóns, π^+, π^-, e e^+, e^- son identificadas.

Introduction

The HADES spectrometer is perhaps the most sophisticated spectrometer developed until now at GSI (Darstadt, Germany) for the study of the Physics underlying the heavy ion collisions at relativistic energies. Together with KaoS, TAPS and FOPI, HADES takes part of an extensive and ambitious programme of fixed target experiments around the SIS-18 accelerator, aiming to analyze several and complementary aspects of the nuclear collisions at beam energies of about 1-2 *A*GeV.

HADES (High Acceptance Di-Electron Spectrometer) was designed specifically to detect and analyze the properties of the vector mesons (mainly ρ, ω, ϕ) via their decay in electron-positron pairs. At the typical energy ranges of HADES, a considerable modification of the properties of the hadrons is expected due to the possible partial restoration of the so-called chiral symmetry at the hot and dense matter (reached inside the reaction zone). Among those particles, the ρ-meson and, to some extent, the ω-meson, would decay within the compressed collision zone due to their short life times. The electromagnetic decay of the vector mesons into an electron and a positron would allow the direct determination of the masses through the reconstruction of the quadrimomenta. The leptons, unlike hadrons, does not react with the nuclear matter and can leave the reaction zone undisturbed keeping information of the meson masses. As the dilepton branching ratio of vector mesons is very small, a high acceptance and able to work at very high beam rates device was necessary.

The development of the HADES spectrometer was a big challenge in order to get the best possible and suitable tool for carry out the detection and analysis of dileptons. Among others, it should have a big acceptance with small dead-zones in order to, as far as possible, detect all the leptons produced within the total solid angle, should offer a lepton momentum resolution better than 1% over a wide range (from 100 MeV/c to 1000 MeV/c), should be able to process data at rates up to one million of events per second and finally should offer a good rejection capability of close electron pairs coming from Dalitz decays (mainly from π^0 decays). All this requirements lead to the development and construction of a new type of detection system composed with a set of dedicated detectors, with advanced processing electronics and trigger systems.

One of the essential components of the spectrometer is a time-of-flight (*tof*) wall which, placed after the magnetic lever arm, contributes to the first and second trigger levels providing also multiplicity and *tof* signals. In the lower polar angle region (between 12^0 and 45^0), the outgoing particles reach the highest densities and so it is a region with great interest. The requirements for such *tof* wall was not only to deal with the current setups but also to work with the light ions and high rate that will be produced in the future SIS100 at FAIR (Facility for Antiproton and Ion Research). The wall should provide time resolutions below 100 ps, with a granularity of the order of $\sim 2cm^2$ and at rates up to $1kHz/cm^2$. In order to cope with that, the Collaboration decided to develop and install a detector based on timing Resistive Plate Chambers (tRPC) technology. This kind of detector did became recently very popular due to the excellent performances that they offer at an affordable price.

Thus, the HADES tRPC wall has been designed, developed and built by a collaboration of the GSI, the LIP of Coimbra, the LabCAF of the Univ. of Santiago de Compostela and the IFIC of Valencia. The first viability document was written in 2002 and, after several tests done at the GSI, facing the improvement of the prototype cells, the project got European funds to be built in 2005. The project did required, among others, the development of specific shielded tRPC cells with very low crosstalk, a dedicated amplifying, digitizing and low power supply front-end electronics (FEE) and the development of a new data acquisition board, the TRB,

that has been recently incorporated also by other HADES detectors. All this achievements make the development of the tRPC wall a very interesting and fruitful initiative.

Today, the detector, composed by six identical sectors (plus one spare sector) covering a total surface of about $8m^2$, and with a total of 2244 FEE channels, has been already installed and commissioned in the HADES spectrometer and it is ready to participate in the forthcoming Physics runs.

We present here the work we have done related with the software development and performances analysis under different conditions is presented.

In the first two chapters, a description of the HADES experiment, including its physics and main results and the spectrometer and its upgrade is given, and an overview of Resistive Plate Chambers detectors is offered.

Then, in Chapter 3, the HADES timing Resistive Plate Chamber (tRPC) wall is described in detail. Its design, specifications and components are presented.

The description of the dedicated software for the tRPC is offered in Chapter 4. That software was written in C++ and developed under the HADES event reconstruction framework (HYDRA) in order to fully integrate the wall in the Spectrometer.

Then, the main results of performances analysis are presented. In Chapter 5 are presented the results obtained with a previous tRPC wall prototype under realistic conditions. Results from a dedicated experiment with some tRPC cells under different ion species up to Z=6 are presented in Chapter 6, and a deep discussion of results is offered. Once all tRPC sectors were built, they were validated in dedicated setups at GSI with cosmic ray data. The description and main conclusions of this setup are presented in Chapter 7.

Finally, Chapter 8 shows the performances and behaviour of the tRPC fully integrated in HADES, working at nominal conditions, under different beam setups both with and without magnetic field. The first attempt for Particle Identification with the HADES tRPC wall is offered.

A final Chapter at the end of the document is devoted to the conclusions and to summarize the main achievements.

Chapter 1

The HADES Experiment

The investigation of hadron properties inside nuclear matter at normal and high densities and temperatures is one of the main goals of current nuclear physics studies. Hadron induced reactions on heavy nuclei (e.g. Au, Pb) are the proper tool to probe particle properties in long-living ground state nuclear matter. Heavy ion collisions at energies of 1-2 AGeV can be used to create a reaction region of increased density for as long as 10 fm/c. Under these conditions, considerable modifications of basic hadron properties (masses, decay widths, etc.) are expected and probably can be verified for the first time experimentally by high resolution lepton pair decay measurements. Such investigations can be essential to understand processes like, for example, those giving birth to the Universe in the Big Bang and its later evolution, since at those moments the medium was one of very temperature and density. This line of investigation contributes also to obtain the equation of state of nuclear matter which is not only important in Nuclear Physics, but also to understand physical processes taking place during the latest stages of stars evolution.

In order to investigate these phenomena, the electron-positron pair spectrometer HADES [3] was set up and an international collaboration was started. This Collaboration is composed of 19 institutions from 9 European countries, with almost two hundred of scientists working to-

gether. HADES, High Acceptance Di-Electron Spectrometer, is the name of the full detector system. It consists on a variety of instruments working in harmony in only one spectrometer. The HADES central headquarters is placed at the GSI (Gessellschaft für SchwerIonen forschung) institute in Darmstadt, Germany. The spectrometer and the needed particle accelerator, the GSI-SIS18, are also there. The focus of HADES is the study of in medium modifications to the properties of the vector mesons coming from di-lepton decays.

A summary of the Spectrometer, its physics and the latest corresponding results, and the near future of the collaboration is given in the following sections.

1.1 The HADES Physics

The physics program of HADES is broad and includes the study of electron-positron pair emission in relativistic heavy ion (HI) collisions, dielectron production in elementary reactions and experiments aimed at studying the structure of hadrons. With the available beam energies (4.5 GeV protons, 1-2 AGeV heavy ions) the interest is focused on the pair invariant masses up to $\sim$1 GeV/c^2.

As leptons do not undergo strong interactions but interact only electromagnetically, they are considered penetrating probes of compressed hadronic matter formed within the collision zone of relativistic heavy ion reactions. Predominant dilepton sources for $m_{e^+e^-} > 500 MeV/c^2$ are two-body decays of the light vector mesons ρ, ω and ϕ produced in these collisions (Table 1.1). The very weak final state interaction allows to reconstruct their invariant mass distributions in the hot and compressed hadronic environment by means of quadrimomentum measurements. This provides the possibility to test various theoretical predictions for hadron mass modifications at moderate temperatures ($T < 80$ MeV) and nuclear densities up to 3 times as large as compared to the ground state nucleus.

There is an exciting and fundamental idea behind this measurement. It is connected to a question of the mass origin of light hadrons (made from *u*,*d* quarks). It is commonly accepted that only a small part of a hadron mass is provided by the rest mass of it constituents. For

Meson	Mass $(\frac{MeV}{c^2})$	Width $(\frac{MeV}{c^2})$	$c\tau\ (fm)$	Dominant channel	e^+e^- branching ratio
ρ	775.49	149.1	1.3	$\pi\pi$	4.72×10^{-5}
ω	782.65	8.49	23.4	$\pi^+\pi^-\pi^0$	7.28×10^{-5}
ϕ	1019.45	4.26	44.4	K^+K^-	2.95×10^{-4}

Table 1.1: Light vector mesons life times [4]

example taking an average current mass of the *u*,*d* quarks of 10 MeV/c^2 one arrives to the conclusion that $\sim$97% of the nucleon mass is dynamically created by strong interactions. The main mechanism responsible for this spectacular phenomenon is related to the spontaneous chiral symmetry breaking, a basic feature of the vacuum structure of QCD, signaled by the appearance of quark and gluon condensates. Formation of the condensates is a non-perturbative QCD phenomenon, and its studies are very difficult. They are performed via lattice QCD or model approaches based on effective field theories.

QCD inspired models predict the decrease of the quark condensate as a function of temperature and/or baryon density of the nuclear matter. Although the quark and gluon condensates are not an experimental observable, QCD sum rules relate their expectation values to the integral over hadronic spectral functions and therefore open a possibility (though not direct) to study their behavior in the nuclear matter. In the early '90s, it was suggested ([5]) a scaling low which relates the drop of the quark condensate with hadron masses as a function of the nuclear density. This suggestion has triggered widespread theoretical ([6]) and experimental activities.

The experimental strategy of dielectron experiments is twofold:

1. extract dilepton (e$^+$e$^-$ or $\mu^+\mu^-$) radiation from hot and dense phase (in-medium part), later called "enhancement"

2. identify the contribution from ρ/ω decay and determine the relevant spectral function

The dilepton spectrum measured in heavy-ion collisions, however, contains contributions integrated over the whole time evolution of the system. The in-medium part can be experimentally derived if the contribution form the freeze-out stage is subtracted. Such procedure has been successfully applied in high energy experiments performed at the CERN Super-Proton-Synchrotron (SPS) and RHIC. Enhanced low mass (M $<$ 1 AGeV/c^2) dilepton pair production in nucleus-nucleus collisions were reported by CERES [7], NA60 [8] at $\sqrt{s} \approx 17$ GeV and recently at $\sqrt{s} \approx 200$ GeV by PHENIX [9] collaborations.

The findings at SPS energies have been successfully explained by theoretical models assuming substantial broadening of the in-medium ρ-meson spectral function. At lower beam energies (1-2 AGeV), similar enhancements were measured by the DLS and HADES collaborations, but, in contrast to the SPS energies, they were lacking full theoretical explanation.

The DLS collaboration at BEVALAC [10], studied as well in the 90's the di-electrons from pseudo-vector mesons coming from the fire-ball. Whereas the invariant mass spectra obtained for $p+p$ interactions could be reasonably well described by theoretical calculations neglecting *in medium* effects, a very distinct situation arose even in light systems as $C+C$ and $Ca+Ca$ at 1 AGeV. Under such conditions neither calculations assuming free di-electron decays nor those including *in medium* effects could describe the observed spectra. In particular an enhancement above a factor 2 was observed in the intermediate invariant mass region of 150-500 MeV according to different transport models. This discrepancy of a factor 2 still remains unexplained and has been denoted as "DLS puzzle", justifying new experimental and theoretical efforts (like HADES).

Figure 1.1 shows the dielectron invariant mass distribution recently measured by HADES in C+C collisions at 2 AGeV [1]. The distribution is compared to the sum of expected decays of long-lived hadrons ($\pi^0 \rightarrow \gamma e^+e^-$, $\eta \rightarrow \gamma e^+e^-$, $\omega \rightarrow e^+e^-$, $\omega \rightarrow \pi^0 e^+e^-$) after the freeze-out (line A). A strong enhancement over these sources (for $M > M_{\pi^0}$ = 0.15 GeV/c^2), shown on the right side, indicates the importance of contributions from short-lived sources. It can only partially be explained by additional Dalitz decays from nuclear resonances $\Delta(N*) \rightarrow Ne^+e^-$ abundantly excited at these energies and much more rare $\rho/\omega \rightarrow e^+e^-$ de-

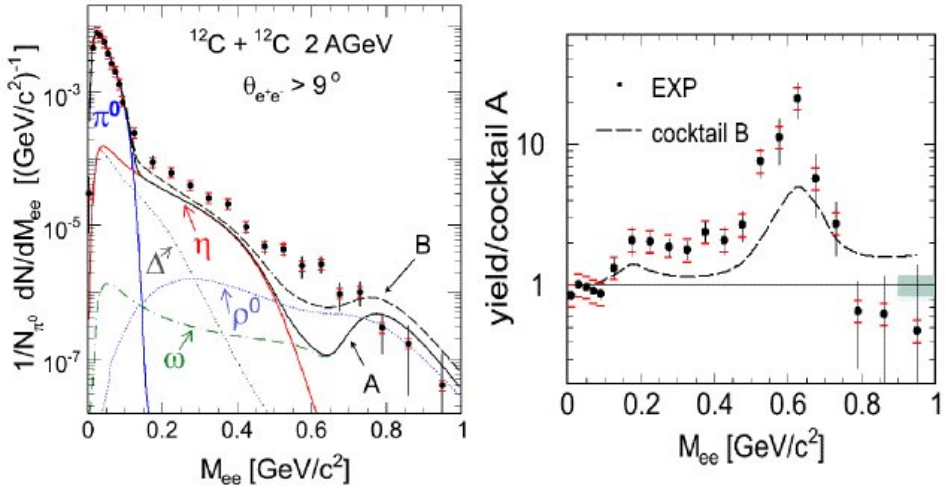

Figure 1.1: Left: Invariant e^+e^- mass distribution measured in C+C collisions at 2 AGeV compared to the contributions expected from decays of: (i) long lived hadrons after freeze-out (cocktail A) and (ii) short lived resonances (ρ, Δ) (cocktail B). Right: Ratio of data and cocktail A, and cocktail A and B (dashed line). The latter shows expected contribution from ρ, Δ decays inside the fireball.

cays (dashed line B). However, the interpretation of this excess is far from trivial due to lack of complete understanding of the dielectron production in nucleon-nucleon interactions $NN \rightarrow NNe^+e^-$ at these energies. In particular inelastic nucleon-nucleon interactions with resonance ($N*/\Delta$) excitation and its subsequent Dalitz decay were never measured. These reactions can generally be regarded as the bremsstrahlung process, where the emitted virtual photon comes from the nucleon vertex. This elementary process has been theoretically studied in the framework of One Boson Exchange (OBE) models, but also needs dedicated experimental investigations to fix model uncertainties. In particular, vector meson production (which can also be treated as the bremsstrahlung) and the role of meson-baryon couplings are additional important processes which require detailed studies. Such investigations are currently performed with the HADES spectrometer using proton, deuteron and HI beams.

Studies of in medium vector meson spectral functions are also possible at normal nuclear density using proton, pion or photon induced reactions. Results obtained by CB-TAPS with γ-A collisions indicate significant modification of the ω spectral function [11]. On the other hand experimental data [12] on the ρ meson are controversial. For this reason the HADES collaboration has launched a dedicated programme of vector meson production in proton and pion induced reactions. The low proton beam energy of 3.5 GeV (or 1.2 GeV for pions) allows to increase the sensitivity to the in-medium meson decays and will allow to tackle this interesting alternative.

The programme will be continued at higher beam energies (8-10 *A*GeV) available at the future FAIR facility. HADES operation at higher beam energies will allow to study the hadronic matter at even larger baryonic densities and hence will provide complementary information on the spectral function evolution as a function of density and temperature. Thus, data from HADES will allow to extend the experimental information on the in-medium physics offered by dielectron probes from URHIC down to 1-10 *A*GeV range and hence to cover the full phase space diagram of the nuclear matter.

In the last two years, the collaboration has done also an effort in the analysis of strangeness production. In [2] are presented the phase space distributions and multiplicities of K^+, K^- and ϕ mesons produced in Ar+KCl reactions at a kinetic beam energy of 1.756 *A*GeV measured with HADES. The percentage of K^- mesons coming from ϕ decay was found to be $18 \pm 7\%$. In the same run, large statistics has been collected for the produced K^0_S and Λ in the phase space region around mid-rapidity. The high quality of these data allowed to comparisons with theoretical models as reported in [13]. Also, the momentum spectra and rapidity distributions of π^- has been measured and the reconstructed K^0_S suggested a strong repulsive in-medium K^0 potential of about 40 MeV strength [14].

1.2 The HADES Spectrometer

HADES is a second generation experiment in high resolution dilepton spectroscopy. It intends to precisely measure the invariant mass of lepton pairs produced by the decay of vector mesons in heavy ion collisions. That goal puts a number of requirements on the design of HADES, shaping it.

The design of HADES is governed by the high-multiplicity environment of heavy ion collisions, the production cross sections below threshold, and the small branching ratio for the dilepton decay channel due to the electromagnetic coupling constant. Only one of $10^5 - 10^6$ central Au+Au collisions will produce an e^+e^- pair from a meson decay.

HADES features six identical sectors defined by the superconducting coils producing the toroidal geometry magnetic field. The spectrometer has 85% azimuthal acceptance and covers polar angles between $\theta = 18^o$ and $\theta = 85^o$. The angular momentum acceptance has been optimized for the detection of dielectron decays of hadrons produced in the SIS energy regime. It provides a single electron efficiency of 50% and a vector meson mass resolution of $\sim$2.5%. For a more detailed description, the reader can have a look at [15].

Fig. 1.2 shows an schematic view of the HADES spectrometer. The detector systems in HADES are, from inner to outer:

- Start and Veto detectors located 75cm before and after the target respectively. These are two fast CVD[1] diamond detectors, with high-rate capability, radiation hardness and low noise; they provide a 'start' signal for the Spectrometer's TDCs and do the veto for the events with no interaction in the target. For the HADES upgrade, the Start detector has been replaced by a new design (see Section 1.3). Nevertheless, for light beams like proton or pion beams, since the deposited energy in Start and Veto is too small, it is necessary the use of an alternative system of five scintillating fiber detectors [16] tracking the beam before and after the target.

[1] Chemical Vapour Deposition

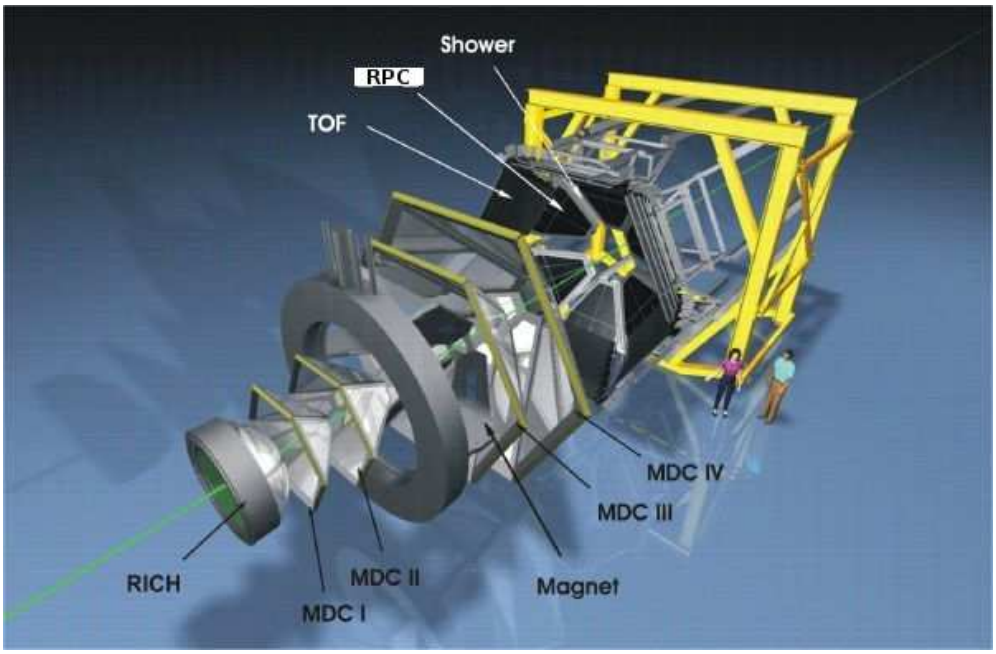

Figure 1.2: 3D view of the HADES Spectrometer

- A Ring Imaging CHerenkov (RICH) detector surrounding the target. This detector works in the threshold mode and provides electron identification, since it is blind to hadrons. It consists in a low Z gaseous radiator, C_4F_{10}, whose Cherenkov light emitted is reflected by a spherical carbon fiber mirror to the back part of the system being focused as a ring image. There, the light is collected by photosensitive CsI cathodes of six Multi-Wire Proportional Chambers operated with CH_4.

- A magnetic tracking system composed of two sets of two Multi-wire Drift Chambers (MDCs) separated by a superconducting magnet made up of six coils shaping a toroidal field embedded in the space between the chambers. Each MDC holds 6 planes of wires with different orientation in space and all together determine the track's direction and position before and after the magnet, as the magnet provides the deflection between

them. The field strength goes from some tens of mT in the borders up to 3.5 T in the middle region.

- A Time Of Flight (TOF) wall for large polar angles ($45^o < \theta < 85^o$) consisting in 64 plastic scintillator rods (BC408) read at both ends by EMI 9133B photo-multipliers. The system contributes to the fist level multiplicity (LVL1) trigger and performs time-of-flight measurements with an accuracy of $\sigma \simeq 100 - 150$ ps.

  For low polar angles (below 45^o), the four provisory big plastic scintillators per sector (TOFino detector) were replaced by a timing Resistive Plate Chamber (tRPC) Wall by the end of 2009 as a part of the HADES upgrade. This RPC system is described carefully in the next chapters as its development, testing and commissioning is the major issue of this work.

- A SHOWER detector made of three gaseous chambers separated by lead converters with signal pick-up in pads of squared shapes, placed behind the RPC Wall. It is able to separate electromagnetic and hadronic showers helping in the Particle Identification procedures increasing hadron rejection.

In addition to the detectors themselves, highly advanced electronics for trigger, read-out and data acquisition is also available, as well as a complete software framework, called HYDRA (See Section 4.1), for the whole event reconstruction, data storage and analysis.

1.3 The HADES Upgrade

A new Proposal was written by the Collaboration [17] and new Physics is expected in HADES both in the near future and by the time it is integrated in FAIR (the so-called "HADES-at-FAIR" project). Thus, during 2009 data taken was suspended in HADES in order to install and commission new spectrometer components and to upgrade part of the data acquisition (DAQ) system. With all new systems in place, HADES will be able to take data for Au+Au collisions at a rate of 20 kHz and up to a factor two faster for lighter systems.

Among the detector parts replaced are all six MDCs of the inner plane, the lower-angle time-of-flight system, new Start detector, new Front-End-Electronics for the remaining systems, the forward wall system and a new DAQ system. Some of the most important features of that upgrade are explained in the following.

1.3.1 The new Plane I Mutiwire Drift Chambers

The innermost tracking plane of HADES receives the same integral dose of radiation while having substantially smaller dimensions than the outer planes, although at same granularity. To guarantee stable operation at the much higher rates and multiplicities expected for the upcoming runs, it was decided to rebuilt the MDC-I chambers by introducing several design changes compared to the original concept. Among those changes are: Cu/Be field wires providing less critical constraints on the mechanical wire tension and long-term stability, and an optimized frame design.

Together, a new front-end and read-out electronics have been installed with the chambers.

1.3.2 The new time-of-flight assemble for lower angles

A major improvement of the spectrometer in terms of granularity and particle identification capability was achieved once the TOFino detector was replaced by the new Resistive Plate Chamber (RPC) detector, including the installation of its front-end electronics, multiplicity trigger and read-out boards and power supplies.

As already mentioned, the development of this detector constitutes the main topic of this document, so that it will be detailed in the next chapters.

1.3.3 The new Start detector

The new Start detector, tested under beam in September 2010, consists in a mono crystalline diamond mounted on a PCB as shown in Fig. 1.3. It is divided in eight small pads of different

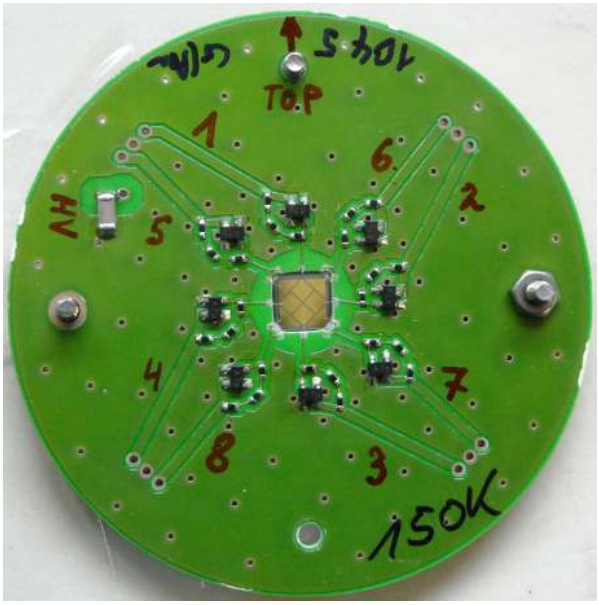

Figure 1.3: The new Start detector: the mono crystalline diamond is mounted on the PCB (metalization in the middle of PCB). The pad-segmented structure is also apparent.

shape with a total size of 4.7×4.7 mm^2 and a diamond thickness of 50 μm. The readout is directly performed with a TRB board working in high resolution 25 ps/bin mode.

A second polycrystalline diamond detector of 8×8 mm^2 is also foreseen and is currently under development.

1.3.4 The Forward Wall

The new HADES Forward Wall (FW) was installed with the purpose of measure the spectators in the nuclear reactions, since the reaction plane is determined from all the participants. With this, the goal is to measure the asymmetry in the production of di-lepton pairs with respect to the reaction plane.

(a) (b)

Figure 1.4: Two details of the HADES Forward Wall: the FW placed in its nominal position at the back side of the spectrometer (a), and the FW scintillators (b)

The FW, adapted from a part of the KaoS hodoscope [18], consists of 288 BC-408 plastic scintillator cells of 2.54cm thickness, with variable sizes of 140 small cells (4×4 cm^2) close to the symmetry axis, 64 middle cells (8×8 cm^2) and 84 big cells (16×16 cm^2). It is positioned 6.5 meters downstream from the target, and covers a polar region of $0.33^o < \theta < 7.7^o$ (See Fig. 1.4).

It was tested for the first time in 2007 under p+p @ 3.5 and d+p @ 1.25 *A*GeV collisions with high proton efficiency. The occupancy of single cells has been studied using simulations and stays below 0.5 in all cases.

1.3.5 DAQ upgrade

In the scope of the data acquisition upgrade [19], essentially all read-out controllers and trigger boards were replaced, introducing a modular system integrating trigger distribution, data transfer and slow-control data traffic to the same optical link. A generic protocol called TrbNet was developed, providing different channels for the different tasks to facilitate the communication. The read-out and trigger distribution boards are based on the universal HADES-TRB

board equipped with TDCs, FPGAs and optical transceivers described in section 3.3.4, one of the major items in the full HADES upgrade project. A detailed description of the new HADES DAQ network can be found in [20].

Chapter 2

Resistive Plate Chamber Detectors

RPC is the acronym for *Resistive Plate Chamber*. These detectors are playing an important role nowadays not only like counter detectors but also like timing detectors (tRPCs). RPC physics and their performances are presented in this chapter.

RPCs are gas ionization detectors with an uniform electric field produced by two parallel electrode plates, where at least one of them is covered by a material with high resistivity. The advantage of such material is that that avoids for sparks or permanent discharges in the chamber, limiting the current In the gap between the plates, a mixture of gases is circulating at atmospheric pressure (see for instance [21] or [22] for a detailed description).

2.1 Historical RPC Introduction

2.1.1 First RPCs

The first RPC, developed in 1981 [23], consisted in two parallel copper electrodes covered with a high resistance plates made of a phenolic resin known as Bakelite, with a volume resistivity $\rho \approx 10^{10}\Omega cm$. The ensemble delimited a gap of 1.5 mm filled with a gas mixture of Argon/iso-butane in a proportion 1:1. The very fast drifting electrons produce a signal that can

be used for timing purposes, whereas the ions drift to the cathode at much smaller velocities, due to their higher mass. The signal was measured with pick-up strips, separated from the High Voltage through PVC. The HV has to be applied through a non-perfect conductor in order to be transparent to the induced signal (see Fig. 2.1 (a)).

In an RPC, the electrons and the ions created by the incoming particle are accelerated by the HV towards the anode and the cathode respectively. During the travel, secondary electrons are created leading to the formation of an avalanche, and a pulse signal is induced in the electrodes and picked up by a readout system. In this simple way is possible to produced a measurable charge from a reduced number of initial charges produced by the incoming particle.

The large resistivity of the electrodes limits the current avoiding the progress of damaging processes like sparks or permanent discharges. But the high resistance of the electrodes also represents one of the main limitations of this detectors. Once the signal is produced, the area where the streamer develops is blind during a given transit time ($\sim$ ms for bakelite electrodes), and during this time the effective field in the region where the avalanche develop will be lower. As a consequence, if the counting rate is very high, one can expect fluctuations in the local field caused by earlier avalanches. The consequence is a reduction in efficiency and time resolution.

Some years later, in 1988 [24], the double gap structure was introduced, and the gap width increased up to 2 mm. The setup was symmetric with the ground electrode in the center and the HV applied over the outer layers (see Fig. 2.1 (b)). This 2-gap configuration allowed for an increase in efficiency and confirmed the time resolution at the level of 1 ns (σ).

2.1.2 Operation modes

RPCs may operate either in the *streamer mode* or in the *avalanche mode* [21].

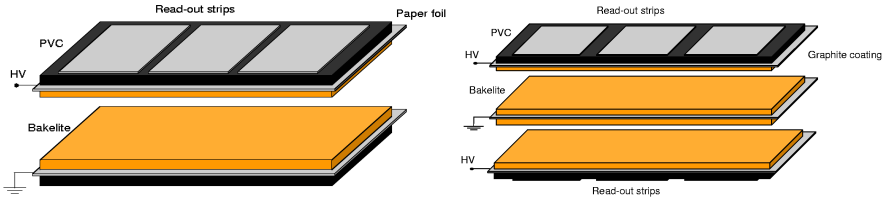

(a) Single gap RPC (b) Double gap RPC

Figure 2.1: Examples of a single gap RPC (a) and a double gap RPC (b) according to their original designs. Dimensions are not realistic, in particular, the gap has been enlarged (pictures from [21])

2.1.2.1 Streamer mode

A streamer is a process of a different nature than avalanche multiplication, releasing a high amount of charge as compared to the one of a normal avalanche. It requires high operation voltages; the secondary ionizations are so large that the charge created distorts the electric field, causing eventually a streamer in the detector gas. This approach has the advantage of providing larger signals that can be discriminated without amplification. The read-out electronics is simplified as compared to the one needed in the avalanche mode. RPCs in streamer mode are well suited for trigger purposes and also for cosmic ray experiments.

2.1.2.2 Avalanche mode

Avalanche mode was introduced as an attempt to improve the rate capability by reducing the charge released per avalanche. Because of the low amplification of the gas mixtures used in this mode, the gain has to be compensated by using high-gain fast amplifiers integrated in the read-out electronics, which is more complex than in the streamer mode.

Originally, RPCs have been operated in streamer mode, but nowadays, RPCs operating in avalanche mode have found application in high energy physics, not only like trigger detectors but also like timing detectors providing resolutions below 100 ps (see Chapter 5).

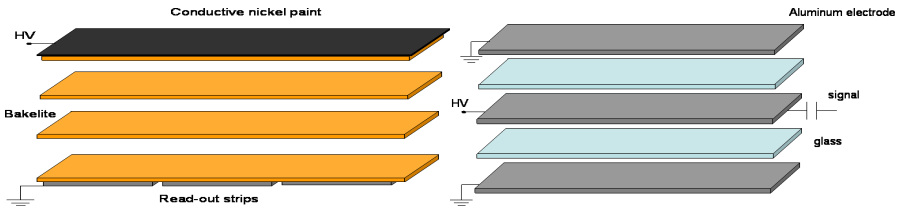

(a) (b)

Figure 2.2: Example of two multi-gap RPCs: a 3-gaps design (a) and the 4-gap design timing RPC studied in the next Chapters (b) (pictures from [21]).

2.1.3 Multi-gap RPCs

This construction method, proposed in 1996 [25], consists on a set of equally-spaced resistive plates that divide the gas volume into a number of individual gaps. HV can be applied to external surfaces and internal plates get a voltage which is the voltage applied to the external ones (see Fig. 2.2 (a)). This is why they are usually called as *floating* plates.

Multi-gap RPCs have been used to construct large area time-of-flight detectors reaching a time resolution of the order of 60 ps (σ) for MIPS with high efficiency [26], [27]. It can be roughly expected that the multi gap allows for an increase in the efficiency as:

$$\varepsilon = 1 - (1 - \varepsilon_N)^N \tag{2.1}$$

where N stands for the number of gaps and ε_N denotes the efficiency per single gap. This value, ε_N, is around 75% in a typical timimg RPC [21]. On the other hand, the time resolution slightly increases, in a first approach, as:

$$\sigma_T = \frac{\sigma_{T,N}}{\sqrt{N}} \tag{2.2}$$

which is the expected if the fluctuations in time response have a Gaussian origin [21].

2.1.4 Timing RPCs

The realization of the importance of the mechanical uniformity of the gap in relation with high precision timing together with the development of fast amplification electronics, made possible to operate a multi-gap RPC in avalanche mode with thin gaps of 0.3 mm and glass electrodes. A new branch in the field was open [28], achieving a time resolution at the level of 120 ps, although the possibility to go down to the level of 50 ps for small detectors was soon confirmed. The use of large size tRPCs was also later confirmed [26], providing resolutions well below 100 ps, with reasonable homogeneity.

Soon after the first development, it became popular the use of standard window glass[1] in RPCs. It is widely available, affordable and still with a resistivity $\rho \simeq 10^{12-13}\Omega$cm, allowing for operation rates up to around 500 Hz/cm^2.

2.1.4.1 Gas mixture

Modern RPCs working in avalanche mode use mostly mixtures of tetrafluorethane ($C_2H_2F_4$) with 2% to 5% of isobutane ($iso-C_4H_{10}$) and 0.4% to 10% of sulphur hexafluoride (SF_6). $iso-C_4H_{10}$ is an UV quencher which prevents from the appearance of secondary avalanches from gas photoionization, and the addition of (SF_6) has been shown to extend the streamer free operation region. Such addition also produces a shift in the efficiency plateau to higher voltages and an improvement in the time resolution [29].

Most of the timing RPCs used nowadays work with the so-called standard mixture, where the proportions are 85% of $C_2H_2F_4$, 10% of SF_6 and 5% of $iso-C_4H_{10}$, or with slight deviations around it [21],[30].

2.1.4.2 Operation voltage

One of the factors which mainly determines the performances of an RPC detector is the electric field applied. Timing RPCs usually work at fields of 100 kV/cm [28], [21]. In principle,

[1] Also called soda-lime-silica glass or just float glass

the efficiency of a tRPC is higher with high voltages, but the problem is that the higher the field, the higher the probability of streamers. Then, the working point has to reach a compromise between high efficiency, good time resolution and low probability of streamers.

2.1.4.3 Read-out electronics

The fast signals induced in the readout electronics of the tRPCs have rise-times at the level of the ns. Then, very fast amplifying electronics are required, with a bandwidth up to 1-2 GHz [31], [32]. Read-out electronics (or Front-End Electronics, FEE) plays a very important role in the time resolution that can be achieved. The intrinsic time resolution of a tRPC detector is very good ($\sigma \sim 50$ ps [29]), therefore the total time resolution will be a quadratic sum of the intrinsic and electronics resolution. Different electronics chains have been developed in order to reduce this contribution to the total time resolution (see for example [33] or [34]). A detailed description of the acquisition electronics of the tRPCs of the HADES wall can be found in [35] and a summary of those is given in Section 3.2.4.

2.2 Timing RPC physics

As timing RPCs is the design used in the HADES RPC wall, its description will be developed in more detail in this section. However, most of the characteristics mentioned in the following can be extrapolated to standard RPCs.

2.2.1 Efficiency and primary ionization

The efficiency of an RPC is related to the average number of ionization clusters produced per unit length n_0/g=1/λ, being n_0 the average number of clusters, g the gap width and λ the mean free path for ionization of the primary particle. In the ideal limit where any cluster is detected, the intrinsic efficiency of the RPC is [21]:

$$\varepsilon_{int} = 1 - e^{-g/\lambda} = 1 - e^{-n_0} \tag{2.3}$$

and, by analogy, the efficiency measured in the laboratory is:

$$\varepsilon_{exp} = 1 - e^{-n_0^{'}} \tag{2.4}$$

where $n_0^{'}$ can be interpreted as the "effective" cluster number. The measured efficiency is smaller that the theoretical one because the lowest value achievable for the threshold of the discriminator is limited by the noise level and the avalanches that induce signals compatible with noise can not be measured. Furthermore, there is always a probability that the electrons in a cluster are attached before arriving at the anode and no electron signal is collected.

2.2.2 Time response

There is a model [36] that explains the main dependencies of the intrinsic time response of an RPC. It allows to obtain the time response function in terms of $n_0^{'}$ (related to the measured efficiency) and the growth coefficient $S = (\alpha - \eta)v_e$ (α is the Townsend coefficient, η is the attachment coefficient and v_e is the drift velocity):

$$\rho_T(t) = \frac{n_0^{'}}{e^{n_0^{'}} - 1} \frac{e^{(\tau_{th}-St)-\exp(\tau_{th}-St)}}{\sqrt{n_0^{'} e^{(\tau_{th}-St)}}} I_1\left(2\sqrt{n_0^{'} e^{(\tau_{th}-St)}}\right) \tag{2.5}$$

where τ_{th}=ln[m_t(1-η/α] and I_1 is the modified Bessel function. The rms[2] (time resolution) can be extracted from Eq. 2.5:

$$rms_T = \frac{K(n_0^{'})}{S(V)} \tag{2.6}$$

$K(n_0^{'})$ has an analytic expansion as function of $n_0^{'}$ that can be found in [37].

Therefore, the time resolution can be separated in two different contributions: on one hand, the fluctuation due to the primary and multiplication statistics $K(n_0^{'})$ that depends on the primary interacting particle and, on the other hand, the growth coefficient of the gas S that depends on the applied field and the particular gas mixture. The effect of τ_{th} in Eq. 2.5

[2]Root Mean Square.

(equivalently, the threshold of the discriminator) is just a global shift that will not affect any moment of order larger that one around the mean of the distribution, in particular the time resolution.

The maximum field applied in a timing RPC is limited by the apparition of streamers, that start to deteriorate the capabilities due to the large charge released. In a first approach, this situation can be identified with the Raether condition $\alpha g \simeq 20$ [38] (where g is the gain of the detector), which is an experimental limit for the maximum gain attainable in wide gaseous detectors before the streamer can progress:

$$m = e^{\alpha g} \simeq e^{20} = 5 \times 10^8 \tag{2.7}$$

this is called *Raether limit*. Replacing α in Eq. 2.6, it is possible to infer that the best time resolution achievable in a given configuration behaves as:

$$rms_T|_{min} \sim \frac{K(n_0^{'})}{v_e} g \tag{2.8}$$

The dependence on the gap size is also present through the number of primary clusters $n_0^{'}$ but, being this dependence relatively small [21], the dominant effect is that the time resolution worsens with the increase in the gap size. This effect is well established experimentally [29], showing deviations for very small gaps (g<0.3 mm).

Eq. 2.5 has tails towards delayed times, becoming gaussian for high $n_0^{'}$. In this limit, $K(n_0^{'}) \simeq \frac{K}{\sqrt{n_0^{'}}}$, ([21]), and Eq. 2.8 can rewrite as:

$$rms_T|_{min} \propto \frac{1}{v_e(E)} \sqrt{\frac{\lambda g}{N}} \tag{2.9}$$

being v_e the drift velocity at the field corresponding to the beginning of the streamers, g the gap size, N the number of gaps and λ the mean free path for ionization.

2.2.3 Time-charge correlation

As it was explained above, Eq. 2.5 stands for the intrinsic response of the RPC and no attempt is done to describe the extra jitter coming from the electronics. Besides the unavoidable electronic jitter, a systematic shift of the time of flight (*tof*) measured at fixed velocity of the primary particle is always present and it depends on the avalanche size. This shift can be subtracted, if the charge is measured, through a procedure called 'slewing correction'.

There is a part of the time-charge correlation coming from electronics, but it has been suggested also that there is an intrinsic correlation coming from the avalanche physics [26]. Typically, the slewing correction allows to improve the time resolution by 20-60 ps (see Table 2.1 and Fig. 5.7).

2.2.4 Space-charge

Space-Charge is crucial for interpreting the charge spectra and efficiencies of both RPCs [39] and tRPCs [40]. It reduces the released charge by several orders of magnitude as compared to the one expected from a proportional regime. Moreover, it allows to reach very high values of α before streamers start to be important, resulting in a very narrow time response (Eq. 2.6).

The avalanche grows until reaching a critical number of electrons, related to the situation where the avalanche self-field is comparable to the applied one, resulting in a reduction of the effective field in a large region of the avalanche development. Further ionizations are highly reduced for a large fraction of the secondary electrons. The average field created by the avalanche is proportional to the number of carriers (neglecting diffusion effects):

$$\overline{E}_{avalanche} \propto \overline{n}_e \propto \overline{q} \tag{2.10}$$

According to the assumptions made, the avalanche will grow up to the point the local field is equal to the applied field E, $\overline{E}_{avalanche}$=E. This implies that $\overline{q} \propto E$. In a parallel geometry $E \propto V$ and therefore:

$$\overline{q} \propto V \tag{2.11}$$

For low voltages, i.e., before the onset of the Space-Charge regime, the growth of the average charge $\overline{q}$ with V will be the one expected for a proportional counter:

$$\overline{q} \propto e^{\alpha(V)g} \tag{2.12}$$

For high fields, the behaviour of α as a function of V can be approximated by a linear trend [41], so the growth of the $\overline{q}$ with V is well described by an exponential.

2.2.5 Prompt charge vs induced charge

The charge induced during the drift of the electrons along the gap is denoted as prompt/electronic charge q_{prompt}, a process that takes place in the first 3 ns after cluster formation ($v_e \simeq 100\ \mu m$/ns, $g/v_e \simeq 3$ ns). The drift time of the ions is considerably larger, at the level of μs. The *induced charge* $q_{induced}$ is used to denote the charge induced during both the drifts of the electrons and the ions of the gap.

The total charge released, denoted as the *total charge* q_{total} or simply q, cannot be accounted for before the flow in the resistive plates takes also place (at the scale of its relaxation time). The average ratio $\overline{q}_{prompt}/\overline{q}_{induced}$ is often evaluated, as it has a dependence in the case of a parallel plate chamber in the proportional regime:

$$\frac{\overline{q}_{prompt}}{\overline{q}_{induced}} \simeq \frac{1}{\alpha g} \tag{2.13}$$

indicating that most of the collected charge is induced during the ions drift, as these are mainly produced close to the anode, drifting along the whole gap g. In the presence of Space-Charge effects, the ratio is modified and different descriptions of this regime can be evaluated [40].

2.3 Timing RPCs in the world

Due to the outstanding time performances and low price, some different timing RPC walls, in construction stage or already finished that have been developed, are described in the following. The main experiments that are nowadays applying this technology to the field of nuclear and particle physics are: HARP [42], ALICE [43], STAR [44], FOPI [45] and HADES [15], although others like CBM [46] foresee to use this technology in the future. Main features of these timing RPC walls are summarized in Table 2.1.

2.3.0.1 HARP

Located at the T9 beam of the CERN-PS, the tRPC wall of the HARP experiment is the first timing RPC wall to operate in a HEP experiment (it took data in 2001 and 2002) and the only one taking data so far[3]. The RPC system was designed to measure TOF for particle momenta in the range of a few hundred MeV with a time resolution of $\sigma_T < 200$ ps which is considered adequate despite the short particle flight distances of 0.5-2 m. In line with the goal to measure differential cross-sections at the 1.2% level, the detection efficiency was required to be $\sim$99%. There were no particular requirements on rate capability and spatial resolution given the low event multiplicities in HARP ($<$1 Hz/cm^2).

The design and construction of the whole cells (368 channels) and the electronics was done between December 2000 and April 2001. It is based on the original design by [28], consisting in 4 gaps, 0.3mm wide, operated at 3 kV/gap, with resistive plates made of standard float glass in a double layer configuration for avoiding geometric losses. The chambers operated with a gas mixture of $C_2F_4H_2$/SF_6/iso-C_4H_{10} in a proportion 90/5/5. The glass is 0.7mm thick with a specific resistance of $\sim 10^{13}$ Ωcm, over an area of 192×10.6 cm^2 per tRPC module, being each module divided in 64 pads, grouped in 8 strips per FEE channel.

Typical efficiency is at the level of 99% and time resolutions around 150 ps, that can be reduced to 105 ps for a single pad. Crosstalk was reported below the level of 10%. Although

[3] Besides that the HADES tRPC is already taking data, there was developed no major physics with it

rate capability was not a tight requirement, a test was performed at Φ=2 kHz/cm^2 at CERN-PS, showing a slight deterioration of the performances.

2.3.0.2 ALICE

The construction of the ALICE tRPC wall was foreseen in 2000 in the framework of the new Large Hadron Collider facility (LHC) at CERN. One of the techniques used by ALICE for PID is the measurement of their time of flight, which combined with the particle momentum and track length, gives the particle mass.

ALICE is a huge project for covering 150 m^2 with 160000 electronic channels and a time resolution below 100 ps, with a high overall efficiency. The detector element is a long MRPC (up to a total of 10 gaps of 250 μm) with 96 readout pads of 2.5$\times$3.7 cm^2 arranged in two rows, with an applied high voltage of V=2.5 kV/gap. The resistive plates are commercial glass as thin as 400 μm.

This MRPC design completely satisfy the requirements of the ALICE TOF wall, providing an efficiency up to 99.9%, resolutions better than 50 ps and an excellent rate capability around 1 kHz/cm^2 but measured under spot illumination during the construction and commissioning of the whole project in 2007 and 2008 [47].

2.3.0.3 STAR

The tRPC wall for STAR at RHIC was born at CERN with some of their members coming from the ALICE tRPC group. This TOF detector replaces the existing 120 trays of the Central Trigger Barrel (CTB). Its main technical requirement is to provide a time resolution below 100 ps over a large area of 60 m^2. The detector is constituted by modules of 9.4$\times$21 cm^2, picking up the signals in pads of 6.3$\times$3.15 cm^2. It is made of 6-gap tRPCs of thin glass (550 μm) and very narrow gaps of 220 μm, allowing the operation at $\pm$7.5 kV between the electrodes.

Tests with a pulsed beam (0.3 ms) over a single tray at CERN-PS seem to guarantee performances at the rates of around 10 Hz/cm^2 expected for the STAR experiment. The

efficiency is at the level of 95-97%, plus additional 5% losses due to geometric inefficiency. Regarding time response, 60-70 ps of resolution were achieved, fulfilling the requirements. Furthermore, measurements under a pulsed beam gave an idea that the rate capability could be higher than 500 Hz/cm^2 and other in-beam measurements for p-p and d-Au collisions have shown also good performances [48].

2.3.0.4 FOPI

FOPI detector is located at GSI-SIS in Darmstadt (Germany). During the last years a ToF wall based on Multi-strip MRPCs [25], [28] has been developed as an upgrade of the existing detector. The ToF barrel has an active area of 5 m^2 with 2400 individual strips (900×1.6 mm^2) which are readout on both sides by a custom designed electronics [49]. The detector design is segmented in a 16 strip anode Multi-strip with an active surface of 4.6×90 cm^2. They use eight gaps defined by 220 μm finishing the line in a double stack configuration (2×4). The anode is placed in between the two glasses. This configuration allows to operate the counters at a moderate high voltage $U_{RPC}\leq$9.6 kV at a high electric field ($E\leq$109 kV/cm).

The cells are optimized for a single-ended readout electronics with an input impedance of 50 Ω. To minimize the internal reflection probability and the signal losses due to impedance mismatch the signal path was adapted to 50 ± 3 Ω.

First developments with 6-gap tRPC (0.3 mm) have reached efficiencies of 97 ± 3% and time resolutions of 73 ± 5 ps [45], using the standard mixture. Its performance has been tested under different conditions: ^{60}Co, proton and deuterium at rates of 50-100 Hz/cm^2. The final tests of mass produced Multi-strip MRPCs showed that the best performance is reached between 1 and 150 Hz/cm^2 with efficiencies above $\varepsilon\geq$99% at time resolutions $\sigma_T\leq$60 ps at an electric field $E\geq$107 kV/cm. The system resolution for the electronics is $\sigma_e\leq$25 ps. The ToF barrel was installed and commissioned in 2007 and FOPI's physics program started.

Detector	HARP	ALICE	STAR	FOPI	HADES
N_{gaps}	4	10	6	8	4
gap size [mm]	0.3	0.25	0.22	0.22	0.28
gas [$C_2F_4H_2$/SF_6/iso-C_4H_{10}]	90/5/5	90/5/5	90/5/5	85/10/5	90/10/0
electric configuration	an-cat-an	an-cat-an	an-cat	an-cat-an	an-cat-an
cell size [cm×cm]	22×10.6	2.5×3.7	6.3×3.1	90×4.6	variable
detector size	10^2	150 m^2	60 m^2	5 m^2	8 m^2
$N_{channels}$ (detector)	368	160000	23000	5000	2000
HV/gap	3 kV	2.4 kV	2.35 kV	3.3 kV	3.2 kV
ε (intrinsic)	99%	99.9%	95-97%	99%	99%
plateau length	300 V	2000 V	500 V	600 V	400 V
σ_T [ps/ch]	-	90	120	-	100
σ_T [ps/ch] (after slewing corr.)	150	40	60	60	73
crosstalk/neighbour	<10%	-	-	-	<2%
3-σ tails	-	-	-	<2%	2%
experiment rates [Hz/cm^2]	1		10	50	700
dark rate [Hz/cm^2]	<0.1	-	<0.3	<1	2-3
rate capability [Hz/cm^2]	≤2000	≤1000	-	-	350
resistive material	float glass	float glass	float glass	float glass	float glass

Table 2.1: Comparison between different timing RPC walls, showing some of their characteristics (Updated table from [35]).

Chapter 3

The HADES tRPC Time-of-Flight Wall

As already mentioned in previous sections, one of the main parts of the HADES upgrade project was the design, development, construction and installation of the new tRPC time-of-flight wall for lower angles. The design of this wall was developed by Dr. D. González-Díaz (at the LabCAF, USC) in his PhD Thesis [21]. The manufactured of the proper chamber was carried out in LIP Laboratory, at Coimbra, Portugal, as well as the gas system. All the electronics, Front-End (FEE), high and low voltage supplies and read-out, was developed as a collaboration of the GSI, Darmstadt, Germany, the IFIC, Valencia, Spain, and our group in the University of Santiago de Compostela [50, 35]. All the previous tests, the cosmic rays and beam commissionings and the final installation were developed by all the involved groups. Finally, the dedicated software was developed by the author.

In this chapter, a summary of the design and wall's features is offered, while the results of the main tests and software development are explained in detail in next chapters.

3.1 Specifications of the HADES tRPC Wall

Fig. 3.1 shows a lateral profile of one of the six HADES sectors, focused on the detectors close to the tRPC wall. The *laboratory* reference system is centered at the nominal target

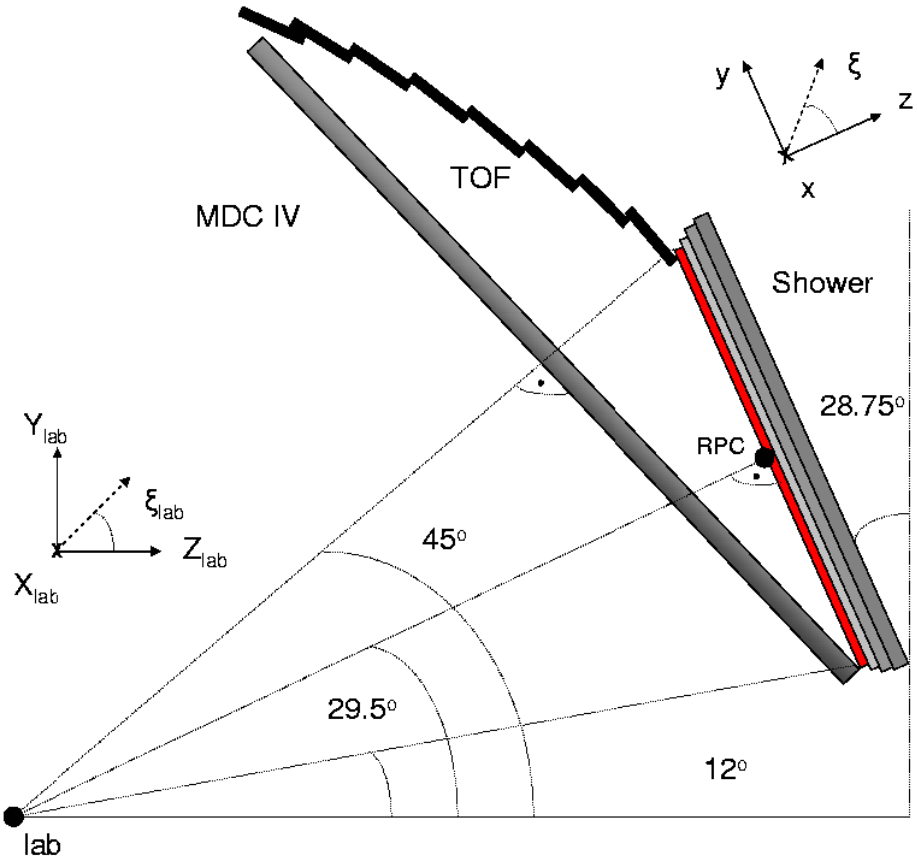

Figure 3.1: Location of the tRPC Wall with respect to the HADES laboratory reference system

position (defined as vertex), with Z coordinate defined along the beam axis and Y defined perpendicular to the floor.

The tRPC wall covers the low polar angle region from 12° to 45° and, practically, the whole azimuthal area. The small angle 12° arises from the necessity to measure positive charged tracks that are bent towards low θ_{lab}. Each sector covers approximately 1.3 m^2 (a total area of $\sim$8 m^2) and it is placed over the Shower detector and both are mechanically attached to the same frame (see Fig. 3.16).

The design of the HADES ToF wall at low angles was optimized for handling the highest rates and multiplicities foreseen at the HADES spectrometer, for the maximum energies available at SIS18 (up to 8 GeV/A). On one hand, this means that the wall must be operational for Au beam intensities up to I=10^8 ions/s impinging over a Au target with 1% interaction probability, according to the technical proposals [51, 17] (for technical reasons it was decreased to I=2×10^7). On the other hand, the detector must have enough granularity to cope with the highest multiplicities foreseen (central Au+Au collisions with a kinetic energy E_{kin}=1.5 GeV/A). Summarizing, the main requirements that the tRPC wall fulfills are:

- Covered area of $\sim$8 m^2.
- Cell occupancy below 20%, recommended below 10% for lepton detection.
- Rate capability up to 1 kHz/cm^2 in the innermost part for higher intensities.
- Granularity determined by a robust multi-hit capability, with a hit-loss probability below 20% for the heaviest system considered.
- High time resolution ($\sigma_T \simeq$100 ps) for separating e^+e^- pairs from fast pions [51] and kaons identification, together with crosstalk level below 1%.
- High both intrinsic and geometric efficiency, close to 100%.
- Equipped with fast, low noise, compact and robust FEE operating a large number of channels under stable conditions.

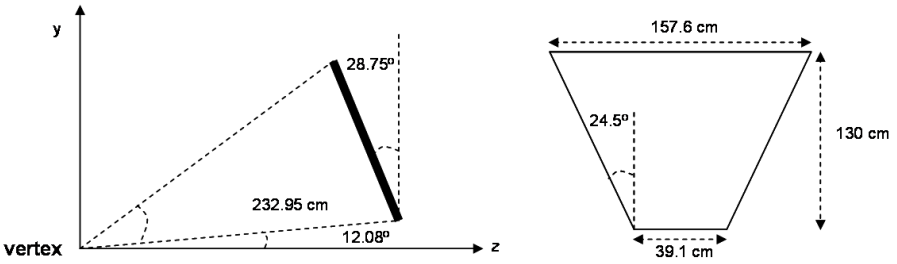

Figure 3.2: Geometric acceptance at the tRPC in the laboratory reference system.

3.1.1 Acceptance

The geometric acceptance of the HADES spectrometer at the tRPC position has been defined by generating all possible tracks from a nucleus-nucleus simulation over it, imposing the condition that such track provides a valid hit in all the MDCs and the Pre-shower (ideal MDC and Pre-shower response was assumed). The dimensions of the geometric acceptance obtained from such procedure are shown in Fig. 3.2, together with its position in the 'lab' reference system. For design purposes, the geometric acceptance is defined at the plane of the last gap of the RPC in the downstream direction.

3.1.2 Expected Rate

The most high expected rate at the tRPC wall as a function of Y (averaged over X) is shown in Fig. 3.3 left. It corresponds to Au-Au at 1.5 AGeV collisions with primary intensity of 2×10^7 ions/s (1% of interaction probability). According to previous works on glass timing RPCs [26], [52], the expected maximum rate reached for the low polar angle region ($\Phi \simeq 700$ Hz/cm^2) is already at the limit where glass tRPCs can offer good performances.

3.1.3 Occupancy

The linear occupancy density is defined as the average number of tracks over the tRPC acceptance per primary interaction per unit length along the y direction. Fig. 3.3 right shows the occupancy for the highest multiplicity environment expected in HADES: central Au+Au collisions at 1.5 AGeV, yielding N=30$\times$6 charged particles over the tRPC.

The requirement of 10-20% occupancy per cell could be fulfilled, at low y, by strips having widths in the range of 3-6 mm. Besides the large cluster sizes observed, it was decided to keep the cell width at the cm scale by mechanical reasons, and the required occupancy levels can be obtained by an additional segmentation of the sector in small sub-sectors or columns. Each segmentation produces an inefficient region due to the separation between the tRPCs columns, that reduces the geometric acceptance. Then, a large number of columns is not advisable. On the other hand, by symmetry, an even-fold segmentation places an inefficient region at the middle of the sector, a zone where an important fraction of the low momentum particles is strongly focused at the tPRC plane [21], [53] due to the inhomogeneities of the magnetic field. Thus, a 3-column segmentation was chosen.

3.2 Design

According to the requirements of the wall and the arguments already commented, a 3-column segmentation (see Fig. 3.4) with cells electrically isolated which keep the occupancy at $\sim$20% in the worst scenario, was a reasonable choice.

The problem of this configuration is that a 1-layer layout constituted by electrically isolated cells requires some spacing between the active volumes of each cell for placing the shielding. Such an approach has been implemented through the use of aluminum profiles. Results of the prototype test developed at 2003 [21] indicate that the loss in geometric acceptance can be almost 15% for perpendicular incidence, even in the very tight configuration chosen, where the active regions were separated by only 3 mm.

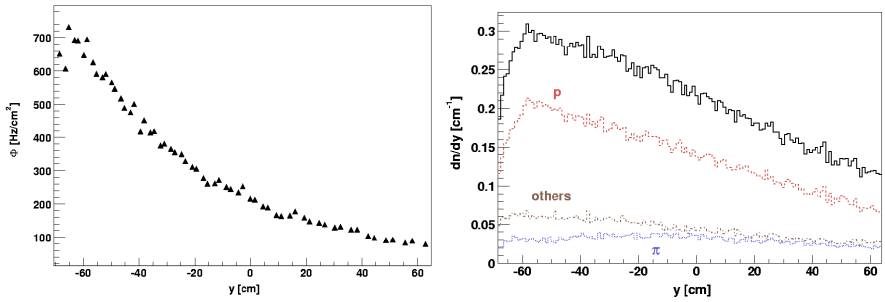

(a) (b)

Figure 3.3: (a) Rate over the tRPC wall for the most unfavorable environment expected at HADES, minimum biased Au+Au collisions at 1.5 GeV/A, I=2×10^7 ions/s, P_{int}=1% and B=0.72×B_{max}. A maximum value Φ=700 Hz/cm^2 is reached at the lower polar angles. (b) Occupancy density at the tRPC wall (full line) for the same environment. The contributions of protons (dashed), pions (dots) and others (dash-dotted) are also shown, being the latter dominated mainly by electrons. The reduction of the number of protons at low y is caused by the MDC frames (pictures from [21])

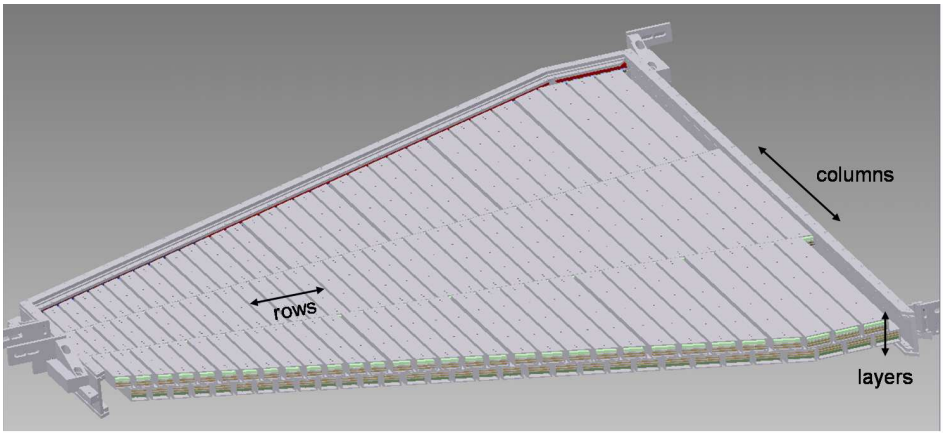

Figure 3.4: View of the final tRPC design. The two layer configuration as well as the column distribution of cells is apparent

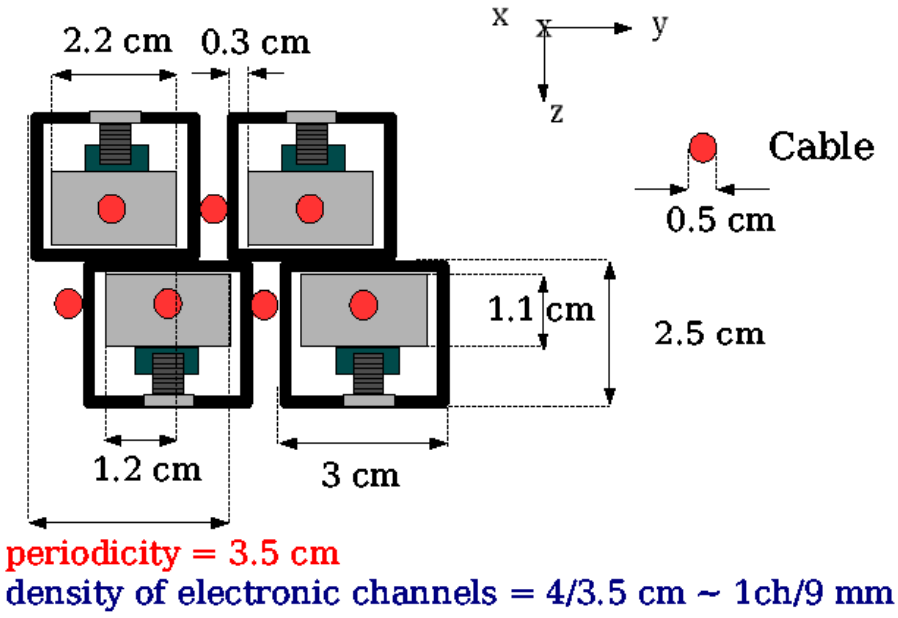

Figure 3.5: Detail of the tRPC cells projected over on of the sides of the wall. Dimensions for the lower polar region and cabling space are shown [21]

3.2.1 Two layers lay-out

For avoiding dead regions, the use of a 2-layer configuration was chosen. The overlap between the two layers was determined in a such a way that all the possible tracks within the spectrometer coming from vertex and with a momentum between 100 MeV and 1000 MeV go through, at least, four tRPC gaps (providing an $\varepsilon \geq 99\%$).

For simplifying the design, other parametrization was also done: in the lower part of the sector, the change in the overlap as a function of y was implemented as a global shift of 1 mm of all the cells in one layer every 10 cm along the y direction.

3.2.2 Geometric Constraints

The final integration of the HADES tRPC wall was performed during last months of 2009. It was an important issue of the wall design, including the final shape and dimensions of the gas box of the required electronic channels room. A full description of all these topics is out of the present work, but let's summarize the three more important geometric constraints [21]:

1. The tRPC gas box must be not thicker than 10 cm in order to not collide with MDC IV frames. In the final 2-layer configuration the thickness can was kept at the level of 10 cm.

2. For solving the high proximity between the TOF photomultipliers and the tRPC gas box (see Fig. 3.6 left) at intermediate polar angles ($\theta_{lab} \simeq 45^\circ$), it was decided to cut the gas box because of practical reasons.

3. The available room for the FEE boards became as small as $v \simeq 4 \times 3 \times 1$ cm^3 per channel. Thus, it was decided to place the FEE boards parallel to the slanting sides of the gas box, allowing for an easier cooling of the electronics. In that case, the available area per channel is approximately 1×4 cm^2 in the low polar angle region. Furthermore, this region is critical for the FEE boards, because the available room between two tRPC sectors is as small as $\sim$1 cm (see Fig. 3.6 right). In order to fit to the available space, the FEE was separated in two different boards (See more details in section 3.2.4)

3.2.3 The Cells

The detector is composed by individually shielded strip-like RPC cells, organized in two partially overlapping layers. Each layer is composed by 31 rows (or cells) and three columns, except the center column of back layer which has 32 cells[1], ranging the widths of the cells between 2.2 and 5 cm and the lengths between 12 and 52 cm [54], being the ones placed in

[1] although the first cell of that column remains as a spare not connected to the FEE

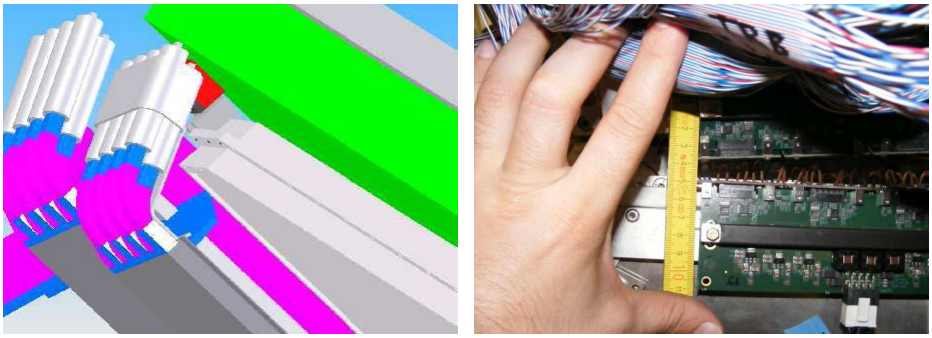

(a) (b)

Figure 3.6: Two critical tRPC Space Constraints: (a) corners of the wide region of the box close to the TOF detector PMs and (b) the Front-End in two different sectors when they are placed in the nominal position. Only 2 or 3 mm are available.

the lower polar angle region smaller than the ones placed in the higher polar angle area, as it is shown in Fig. 3.4.

There are in total 1116 useful cells and 6 spare cells, one per sector. The cells are symmetric timing RPCs with 4 gaps of 270 μm each, made of three aluminum electrodes and two glass electrodes, all of 2 mm thickness (Fig. 3.7 (a)). The resistivity of the glass is $\rho \sim 2 \times 10^{12}$ Ωcm. The gap is defined by PEEK[2] monofilaments, spaced between 5 and 10 cm along the cell. The ensemble is housed inside individual shielding tubes and compressed by the three springs that apply a controlled force to a PVC plate that distributes the force. This layout tries to keep good mechanical uniformity of the gap (any variations above 10% are likely to perturb the time resolution [55]), while minimizing the total glass thickness for optimum count-rate capability. The cells were closed at both ends by Al caps making a very compact and robust piece and easy to handle (Fig. 3.7 (b)).

High-Voltage (HV), 5.5 kV in the nominal operation, is applied to the central electrode via 330 Ω resistors and high voltage cables, while the outer electrodes are connected to ground. The glass electrodes are kept electrically floating [25]. Insulation to the shielding tube walls

[2]Polyetheretherketone.

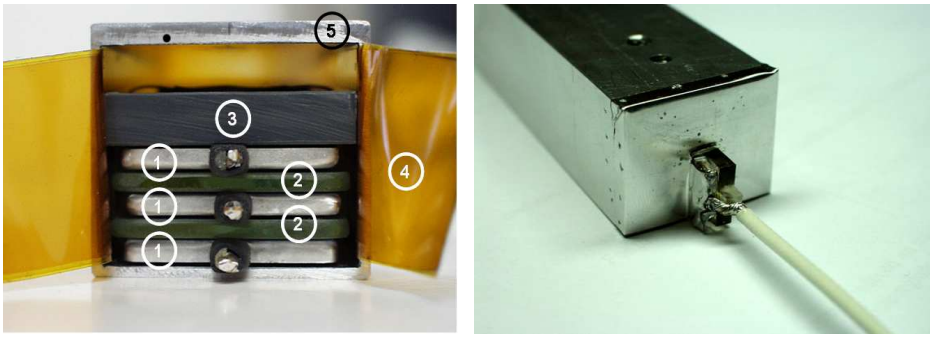

(a) (b)

Figure 3.7: View of the tRPC cells: (a) internal structure with the Al electrodes (1), glass electrodes (2), pressure plate (3), kapton insulation (4) and Al shielding tube; (b) cell with Al foil shielding end-cap and HV cable.

is assured by a triple-layer KAPTON^{TM} adhesive laminate. An end-shield made of aluminum foil is spot-welded on the shielding tubes. The signals are collected by the HV cable and fed out via a 2 nF coupling capacitor and 50 Ω Printed Circuit Board (PCB) stripline feedthroughs that cross the lateral wall of the gas box. Regarding detector-cable impedance matching, no attempt was made.

Fig. 3.7 shows two details of the cells.

3.2.4 The Front-End Electronics

The FEE chain has been designed aiming to fulfill all the wall's requirements regarding space constraints, crosstalk, timing resolution, power consumption and stability. The chain requires a large bandwidth to deal with very narrow RPC pulses, a precise timing and charge information in one digital output signal, one multiplicity output signal for the HADES trigger logic stability, reliability and a compact design minimizing noise.

The FEE is divided in two boards, the *Daughterboard* (or DB) and the *Motherboard* (or MB), attached one to each other in a 90^{o} connection.

The DB consists in a small board ($5 \times 4.5 cm^2$) with two main stages: an analog one and a digital one. In the analog part, the signal is amplified and discriminated. In the digital part, the signal is split in two branches and translated into a single digital pulse giving both the Time-of-Flight and the charge informations[3] of the primary signal. Each DB has four channels, whose input is directly connected to the RPC cell. There are in total 2244 operative channels. The DB was designed by Dr. D. Belver (at LabCAF, USC) in his PhD Thesis, and more details can be found there [35] (Also in [33]).

The MB holds 8 DBs so that there are 32 channels per MB. It provides voltage regulation, threshold DACs, test pulse inputs, route for the outgoing digital and trigger signals and read-out for slow control. In the higher polar region, the short MBs are placed, with the same features as the normal ones but with only three DBs each. MBs are mechanically attached to the gas box. The MB was designed by Dr. A. Gil (at IFIC, Valencia) in his PhD Thesis, and more details can be found there [50].

Fig. 3.8 shows the DBs connected both to the tRPC cells through mini coaxial cables and to the MBs, while those are mechanically attached to the box.

3.3 Other features

3.3.1 The gas system

The gas mixture is applied to the chambers through a recirculating circuit as shown in Fig. 3.9. Besides, a small fraction of gas is being continuously renovated (although the recirculating pump can be easily by-passed so that all gas inside the chambers is always new. This is the usual procedure when upping the chambers to the working point after a break). All the parameters are continuously monitored. Inside the cave, before entering the gas into the chambers, the flux can be controlled via manual fluximeters, one per sector, and also individual bubblers are presented at the output.

[3] The TOF is given by the leading time of the pulse, and the width is related with the charge through a "Charge-to-Width" (QtoW) measurement

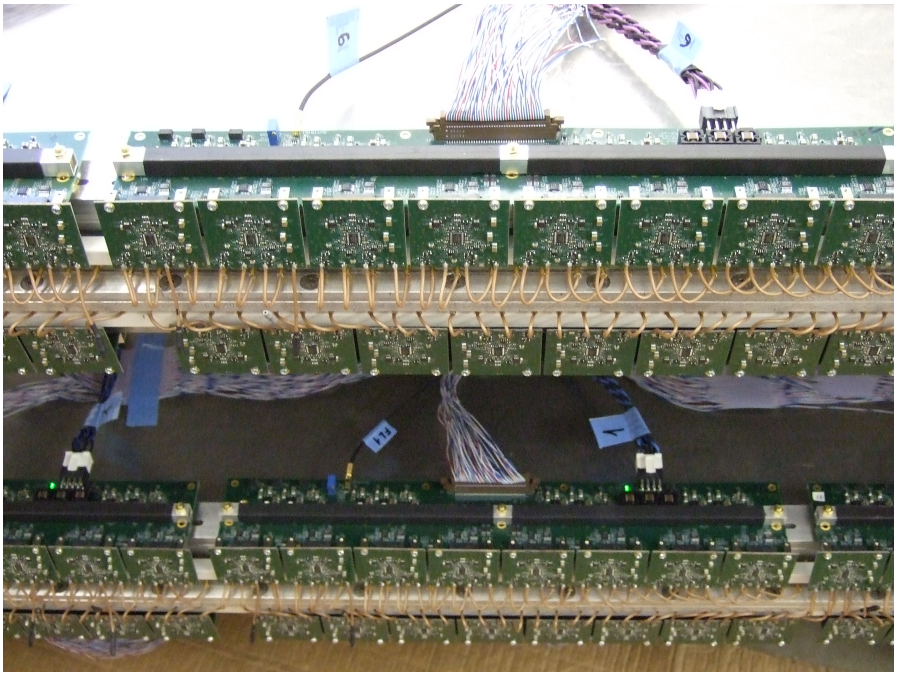

Figure 3.8: Detail of the two FEE boards: the DBs connected both to the tRPC cells and to the MBs in a 90^{o} connection, while the MBs are mechanically attached to the box.

In each sector, the gas is fed through the gas-in connector in one of the layers, taken to the upper part of the sector, and then it is removed through the gas-out connector from the bottom part of the sector but in the second layer. The location of those connectors is different on each sector, depending on the final position of the sector in the spectrometer, to ensure an homogeneous distribution of gas, which means that the sectors can not be exchanged in terms of inner gas distribution.

The final gas mixture used is composed of 90% of $C_2H_2F_4$ (freon R-134a) and 10% of SF_6, running in normal operation at a flow of 50 cc/min.

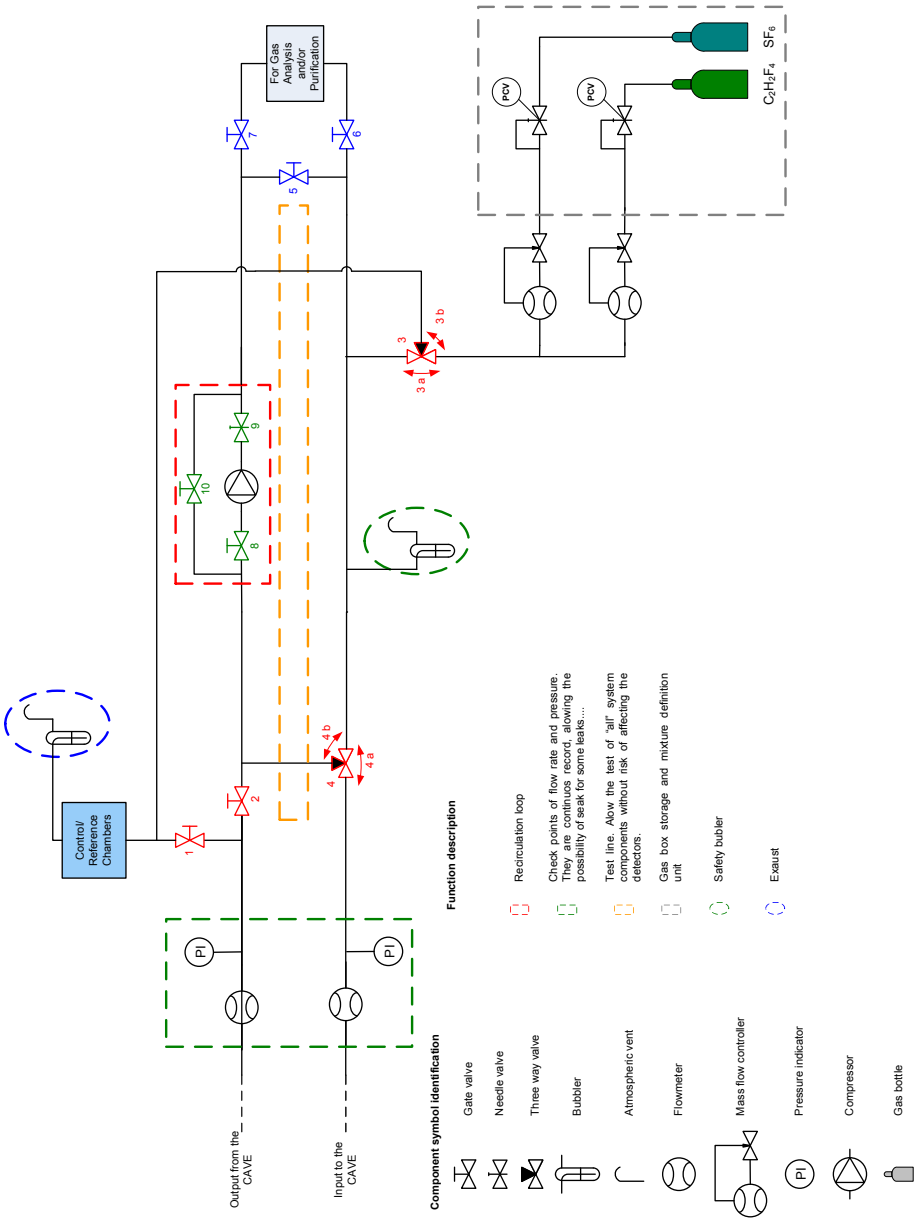

Figure 3.9: Schematics of the tRPC gas system

3.3.2 The Low Voltage Power Supplies

The FEE boards are powered by low voltage (LV) and low ripple custom made boards [56], which are located behind the sectors, directly attached to the main frames (see Fig. 3.10 (a)), based on switching DC-DC converter modules, featuring also voltage and current monitoring. The voltages provided by the low-dropout regulators are +5V, -5V and +3.3V, managing currents of 80 mA, 40 mA and 35 mA per channel, respectively. Two of these boards are enough to feed a whole RPC sector.

At the same time, the LV power supplies are fed through commercial programmable DC TDK-Lambda Power Supplies giving up to 48 V and 30 A. Two of these power supplies are enough for the six tRPC sectors.

3.3.3 The High Voltage Power Supplies

The high voltage (HV) is provided to the tRPC by CAEN A1526 power supplies, mounted on a SY1527 crate, housing 6 channel 15kV per slot in double width boards available with either positive or negative polarity (see Fig. 3.10 (b)). The output voltage can be programmed and monitored in the 0-15 kV range with 1 V resolution. The current full scale can be fixed via internal jumpers either at 100 μA or at 1 mA. The maximum output voltage can be also fixed. The power supply is controlled by the Slow Control system via ethernet.

As each slot houses 6 channels, for the full tRPC two slots are enough since each layer is fed independently. The third slot is used for powering the reference chambers of section 3.3.7.

3.3.4 Read-Out: The TRB board

The Read-Out and data acquisition (DAQ) of the tRPC is controlled via the new Trigger and Read-Out Board (TRB) [57], which was designed at GSI as a general purpose board with on-board DAQ functionality. Each TRB houses four HPTDC from CERN working either in high resolution mode (8 channels per TDC) or low resolution mode (32 channels per TRB). For the tRPC, the low resolution mode is used so that four TRBs are needed to instrument a

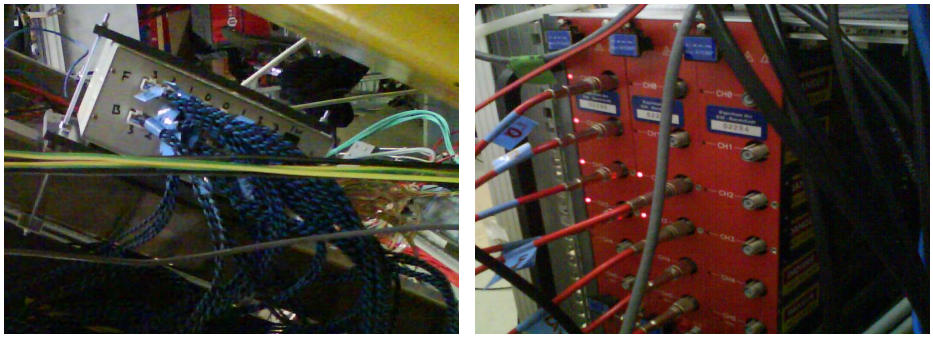

(a) (b)

Figure 3.10: Detail of the LV power supply (a), placed over the main frames behind the sectors, and back view of the HV power supply (b)

full sector (32 channels $\times$ 4 HPTDCs $\times$ 4 TRBs = 512 channels per sector). Although the first version was designed to readout the tRPC detector, the second version has been thought in a way to be detector independent. To broaden the spectrum of possible future applications, a very high data-rate digital interface connector (15 Gbit/s) has been included. It gives the possibility of attaching add-on boards which provide the detector-specific interfaces or FEE (like ADCs) and additional computing resources (FPGAs). The TRB supports EPICS to allow the integration into the HADES Slow Control System (see section 3.3.6). The TRB is also responsible for the FEE discriminator thresholds setting via Serial Peripheral Interface (SPI) by programming the voltage values of the DACs located at the MBs, as well as the same for the BLR (see section 3.3.5).

The TRB includes the following functionalities:

- An ETRAX-FS processor for DAQ and slow control tasks, running Linux kernel in the 128 MBytes of memory and is directly connected to the 100 MBit/s Ethernet link. The integrated three co-processors (200 MHz each) allow to a high IO bandwidth without main CPU intervention.

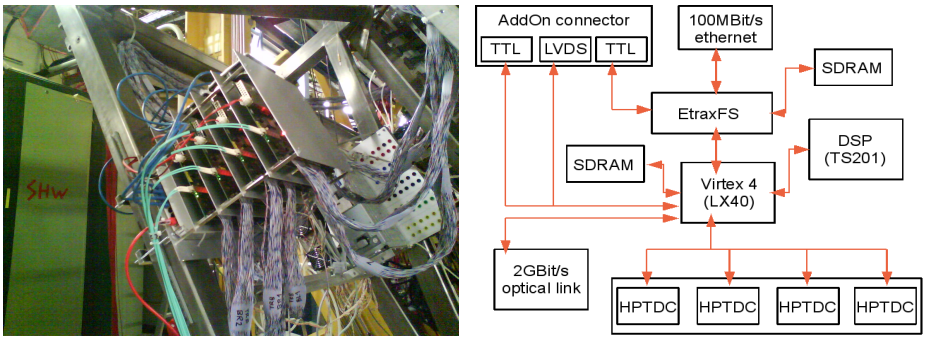

(a) (b)

Figure 3.11: (a) TRB tower housing four boards, placed behind the sectors and mechanically attached to the main frames. (b) Block diagram of the TRB board

- A large FPGA (Virtex 4 LX40) and a Tiger Sharc DSP which can be used as on-board resources for trigger and on-line analysis.
- An optical link with 2 GBit/s connectivity, serialized by the TI TLK2501, as a replacement of the HADES trigger bus and for high speed data transport.

The TRBs stacks are also mechanically attached to the main frames, behind the sectors, as shown in Fig. 3.11 (a), and are powered by the same commercial power supply as the LV system. The TRB block diagram is sketched in Fig. 3.11 (b), and the full FEE+DAQ chain is sketched in Fig. 3.12.

3.3.5 The Base-Line Restorer Multiplicity Trigger board

The Base-Line Restorer board (BLR), recently designed at GSI by Dr. W. Koenig, is being currently used by the tRPC wall for collecting and delivering the multiplicity trigger signal (although it is foreseen to be used also by other systems in HADES like the TOF detector). Each board collects the 16 analog multiplicity signals from the MBs (one full sector) and produces as an output the analog sum of all of them. The most important feature is that such

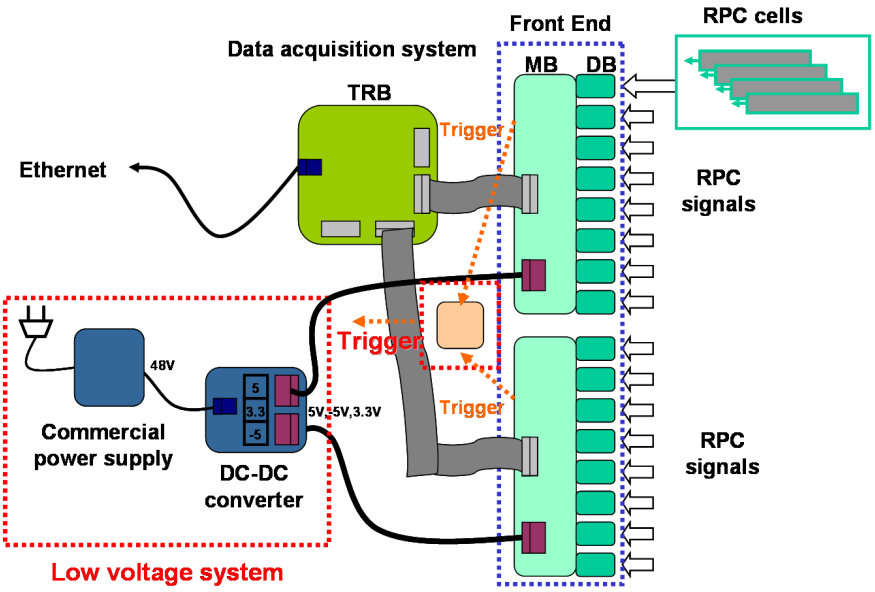

Figure 3.12: Block diagram of the FEE and Read-Out (DAQ) system where groups of four tRPC cells are connected to one DB, eight DBs to a MB and finally, four MBs per TRB. From each MB, the trigger signal output is connected to one channel of the trigger board (BLR).

procedure is performed in a DC-Level independent way from the inputs. The DC level of the analog output is also restored to zero. This feature is achieved via discriminators (monitoring fast signals) and analogue switches which turn off the baseline restorer once a fast multiplicity signal exceeds the threshold.

Each BLR (six in total) is attached to one TRB through a special connector and it is powered with the same 48V power supply. It houses 19 comparators (DACs) controlled and programed via SPI. 16 of those comparators are used for the inputs while the other three are used for three different digital outputs. One can program such outputs to different levels so that one can have three different multiplicity rates at the same time. The BLR also houses multiplexers for sniffing purposes and integration in the Slow Control system.

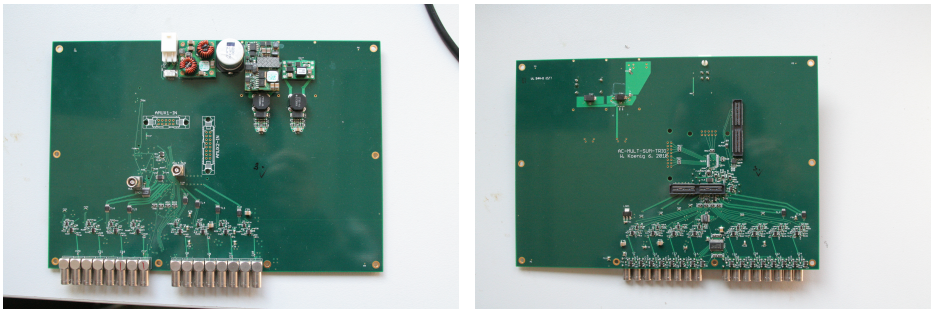

(a) (b)

Figure 3.13: Front (a) and back (b) views of the BLR board. In the front side, the 16 inputs are apparent, as well as the two lemo outputs corresponding to the analog sum and digital outputs. In the middle of the back side, the special connectors for attaching the board at the TRB are placed.

Front and back view of the BLR are shown in Fig. 3.13, while an scheme of its operation is shown in Fig. 3.14.

3.3.6 The Slow Control Interface

The tRPC slow control (SC) system controls/monitors about 6500 variables and is being implemented using the Experimental Physics and Industrial Control System (EPICS) tool [58]. A MEDM graphical interface is developed for the client system. All the tRPC SC system is integrated into the main HADES SC system.

The control and monitoring attends four different systems: FEE, LV and HV systems, detector and gas system. Each system communicates itself via a different and independent hardware interface, but the user interacts with a common application:

- The FEE control requires threshold setting using the LTC2620 chip via SPI
- The LV control and monitors voltages and currents via 1-Wire systems. The TDK-Lambda power supplies are also monitored using their own commercial hardware

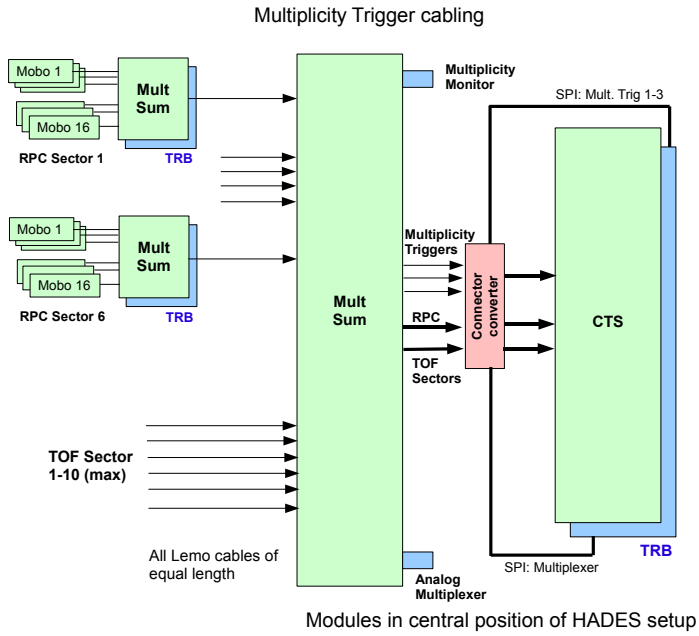

Figure 3.14: Block diagram of the BLR board used also for the Central Trigger System (CTS): such BLR gets inputs from the RPC BLRs and directly from TOF detector and perform the trigger selection.

- The HV is controlled using the commercial hardware already integrated in the power supply
- The detector temperature is monitored through DS18B20 chips placed in different locations on each sector. There are 12 of those chips per layer, 24 per sector, which means 144 lecture channels in total
- The gas mixture is foreseen to be controlled via Analog Devices transceivers, as well as the O_2 levels inside the chambers

A detailed description of the tRPC SC system can be found in [59].

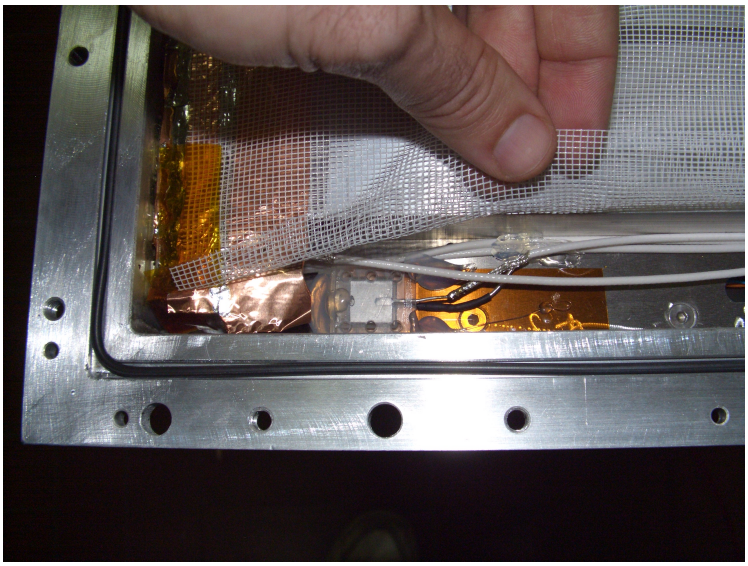

Figure 3.15: Detail of one of the reference chambers (1-gap 1×1 cm^2 tRPCs) located close to the corner of the main box

3.3.7 The Reference Chambers

In addition to all the mentioned in the previous sections, some smalls tRPC cells of 1×1 cm^2, called as *reference chambers*, has been included in each sector, inside the proper tRPC chamber, located in the corners and in the borders of the box, for monitoring purposes (See Fig. 3.15). There are 15 such cells per sector, 8 in the front layer and 7 in the back layer. Those cells are 1-gap timing RPCs of 280 mm gap and glass plates. The electrodes are thin Cu films directly stiked to the glass. The HV is applied in one of those electrodes while the other one is kept to ground. The signal is collected through the HV line and the readout is done by the FEE from [60] allocated in small Al boxes placed in the lower part of the main box. The analysis of such signals is done by digital osciloscopes with ethernet control and they are expected to be integrated in the SC as well.

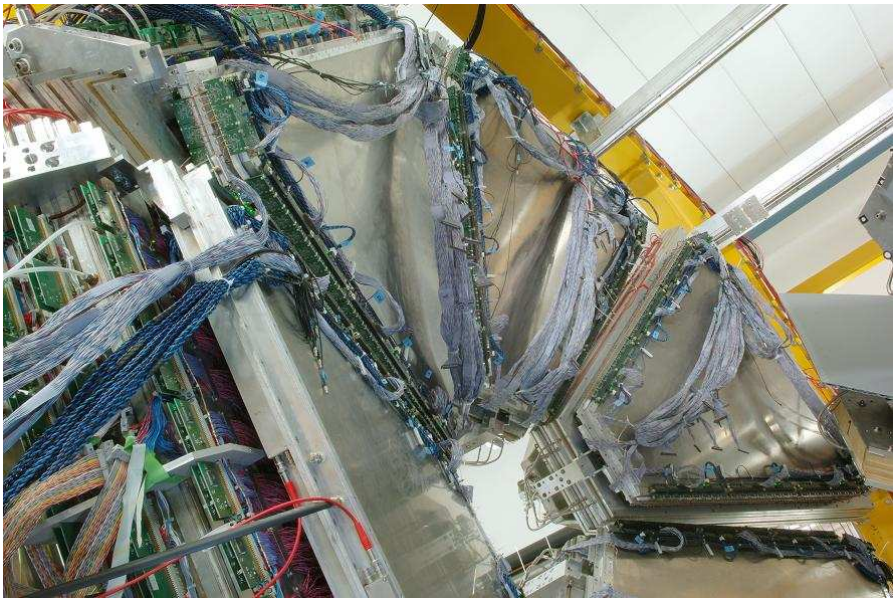

Figure 3.16: View of the tRPC sectors already installed, together with all the FEE and cabling, in their nominal position at HADES, over the Shower detector.

A picture of the final installation of all the six sectors of the HADES tRPC wall, in their nominal positions over the PreShower detectors, is shown in Fig. 3.16. The FEE position over the RPC box is also shown, together with the LV, data acquisition system and trigger and read-out cabling.

Chapter 4

The HADES tRPC Software

Within the tRPC Wall upgrade project of HADES, the needed reconstruction and analysis software for the wall and its integration in the HADES framework was also an important goal. Some software is always needed for enabling us to make use of the detector and transform the low level provided information into some high level data, with higher level physical content. The development of the tRPC software is the subject of this chapter. First, a small description of the main HADES software is given. Then, a detailed description of the tRPC software is offered together the most important features. Some of the most important algorithms are also described.

4.1 The HADES event reconstruction software

HYDRA[1] [61] is the name of the *framework* for the event reconstruction program in HADES. We can say a framework is a set of rules, interfaces and services put at the disposal of programmers, users, physicists..., who can extend it to perform a set of tasks.

In the case of HYDRA, the main goal is the processing of events recorded in the spectrometer. That is, we read input data and those data are processed by a set of algorithms wich

[1] Hades sYstem for Data Reduction and Analysis

depend on parameters and need access to the data in some structured way. As a result, new, elaborated data, are produced.

The reconstruction proceeds in steps. Each algorithm reads some input data, maybe the output of another algorithm, and takes it to a new level of elaboration. In that sense we can speak of *data levels*, wich correspond to the different levels of elaboration.

HYDRA is written in C++, an Object Oriented Programming language. Object oriented represents a new paradigm for software modeling, including the design, evaluation and implementation and enforces the code modularity, reusability and readability. These features allow the management and maintenance of large and complex programs, made by distant collaborators. The concept of the object, a significant representation of a real or abstract entity, which is the element of a class composed of a set of related entities, is a semantic approximation, closer to our minds organization.

HYDRA software is based in ROOT, an Object Oriented Data Analysis Framework [62, 63]. ROOT has been developed at CERN and is specially designed for its use in High Energy Physics experiments. It is made by a set of frameworks and a C++ interpreter (CINT is the C++ interpreter used by ROOT). Main features ROOT has are:

- Provides an user interface
- Provides several systems for storing objects into output files
- Makes graphics and histograms
- Generates documentation automatically from code comments

As disadvantage, ROOT interpreter is not fully compatible with C++. It imposes some restrictions in the software that users can develope in HYDRA.

HYDRA touches five main areas:

1. Data Input; either raw or partially reconstructed
2. Data Output in a suitable form for further analysis

3. Management of algorithm's parameters, like geometry, calibrations...

4. Data structure

5. Management of algorithms

Besides that, one also needs a component to coordinate the different subsystems, where each subsystem is defined by a set of classes.

A new and modern HYDRA version, called HYDRA2, is currently under development in HADES. The tRPC software presented in the following is already integrated in HYDRA2, although its development has started within the old HYDRA.

The full description of HYDRA can be found it in [61].

4.2 The tRPC software

The reconstruction software for the tRPC is integrated in the so-called *rpc* module of HYDRA. It is designed and written in order to take the lowest level of date given by the tRPC and process them to the highest level. The main goal is to provide the hit information to the tracking, matching and momentum reconstruction algorithms of HYDRA. Such hit information consists mainly, among others, in the (X,Y) and (θ,ϕ) coordinates of the hit over the tRPC wall and the Time-of-Flight (tof) measurement.

Several steps are therefore needed to reach that level of information: first, the raw data must be translated into "numbers" in a procedure called *unpacking*; then, some algorithms like calibration are applied to those numbers reaching the so-called *calibrated level* of data; the proper hit finding is then performed and finally a cluster finding algorithm allows to a better selection of data.

Once a data level is reached, all the information is stored so that the user can have access to it at any time.

These steps are described in detail in the following paragraphs, as well as all other features of the framework.

4.2.1 Global Features

4.2.1.1 Detector definition

The definition of the tRPC wall is done through the class `HRpcDetector`. There, the number of active tRPC cells, modules/columns and sectors is set. `HRpcDetector` inherits from the global HADES class `HDetector`. We say that the first *is a daughter* of the last. When this happens, the daughter can use directly all the methods of the mother and can have access to her public or protected data members.

Besides, `HRpcDetector` class is also in charge of create the tRPC categories. A *category* is nothing else but an object container. Main property of categories is that all objects within a category have to instantiate exactly the same class. The reader can advise how each level of elaborated date is then stored in a different category. All categories for the tRPC wall are built in an matrix-like structure, and they are initializated through method `HRpcDetector::buildMatrixCategory()`, giving back an object from class `HCategory`, so that each tRPC category can inherits methods from the global `HCategory` class. There are currently five tRPC categories, namely: `HRpcRaw`, `HRpcCal`, `HRpcHit` and `HRpcCluster` for different levels of real (or simulated) data, and `HGeantRpc` for storing the tRPC output of the HADES simulation package (see Section 4.2.6).

4.2.1.2 Task Set

The list of tasks to be performed is inlcuded in HYDRA via `HTaskSet`. The proper tRPC tasks are set with the class `HRpcTaskSet`, which inherits from `HTaskSet`. Such tasks are set through method `HRpcTaskSet::make()`. If no tasks are specified, only the unpacking procedure is performed. If the option contains “real”, then all the tRPC tasks are performed up to the highest data level, that is, unpacking, calibration, hit finding and cluster finding, while if it contains “simulation”, the digitization procedure is started (see Section 4.2.6) and the simulated data is analyzed up to cluster level. A single task can be also added to the

list of task by method `HTaskSet::add("task.name")`, which is a public method of `HTaskSet`.

4.2.1.3 Parameter Containers

In order to do any kind of event reconstruction, several numeric parameters are needed. Each of these sets of numbers is represented by a subclass of `HParSet` class known as parameter container. The interface class responsible for managing parameter sets in HYDRA is the `HRuntimeDb` class. It implements a runtime database, which has to manage parameter input and output. Each container in the runtime database is identified by a name, and the method `HRuntimeDb::getContainer()` can be used to retrieve a pointer to a container given its name.

There are three accepted formats for the parameter files: root files, ascii files and they can also be retrieved from the ORACLE database. The class in charge of create the tRPC parameter containers is `HRpcContFact`, and each of the accepted formats has its own interface respectively: `HRpcParRootFileIo`, `HRpcParAsciiFileIo` and, common to all systems, `HParOraIo`.

All parameter containers in HYDRA are written in two different ways: the so-called *tree style* and the so-called *condition style*. Tree style containers have the parameters structured in different levels while in condition style each parameter is treated as an element of a one-dimension array. The last are less complex and are used for storing small sets of numbers, while the first are used for storing those parameters which depend on a single detector element.

The tree style containers written for the tRPC are:

`HRpcTrb2Lookup` This is a two level container which links the TRB Id and the TRB channel to the corresponding physical address, that is, sector, column, cell and side. It is used in the unpacking task.

HRpcCalPar Here are stored all the parameters needed by calibration. It is a three level container which links sector, column and cell with the corresponding parameter. It is called in the calibration task.

The condition style containers written for the tRPC are:

HRpcDigiPar This container stores those parameters needed by the digitization task in order to treat the simulated data (for example, the efficiency, the signal propagation velocity, the time and position resolutions, etc).

HRpcQtoWPar Here are stored the parameters for the Charge-to-Width calibration (see Section 4.2.3.2).

HRpcGeomCellPar In this container is stored the geometrical information of each individual tRPC cell, that is: position of the left-down corner of the cell with respect to the *module* coordinate system (see section 4.2.3.1), length and width. As the six sectors are identical since the point of view of the *module*, the container only stores the information corresponding to the cells of one sector.

HRpcHitFPar This container stores those parameters needed in the hit finding task, inlcuding those for the *slewing correction* (see section 4.2.4).

HRpcClusFPar This container is called in the cluster finding task, and stores some needed parameters like the number of hits in a cluster, number of sigmas to be consider a cluster, etc.

In addition, the container `HRpcGeomPar` stores all the geometric information of the tRPC wall. This container is written in an specific way and it is also used by the simulation package in order to create the virtual detector.

There are foreseen also two additional containers for the tRPC: `HRpcCorrPar`, which will store the time-charge correlation parameterization, and `HRpcHitFPar`, which will store additional parameters needed by the hit finding procedure.

4.2.2 Unpacking and Raw Data Level

The unpacking of the raw data, stored in binary *hld* files, is the procedure under which the encoded binary data provided by the Data Acquisition System are translated into readable values. Thus, we reach the so-called *raw* data level in HYDRA. The procedure is carried out by the unpacker codes. There is a common unpacker in HYDRA, called `HTrb2Unpacker`, that must be called by all systems read out through the TRB board. Then, each system, has its own unpacker for filling their respective categories.

As the tRPC is read-out by the TRB, the `HRpcTrb2Unpacker` class was developed. This class inherits from `HTrb2Unpacker`, which is the class that really unpacks the data through the method `HTrb2Unpacker::decode()`. The `HRpctrb2Unpacker` is instantiated in its constructor by the corresponding subsystem identification number (*subEvtId*). Then, the tRPC data is unpacked by the mother class and retrieved by the `HRpcTrb2Unpacker`. The last writes the information into objects of class `HRpcRaw`, which constitutes the category for the tRPC raw data level. The parameter container `HRpcTrb2Lookup` is mandatory for matching the TRB channel with the corresponding physical detector address.

The `HRpcTrb2Unpacker` has two proper features:

`HRpcTrb2Lookup::storeSpareChannelsData()` allows to store also the data delivered by the spare channels (open FEE channels).

`HRpcTrb2Lookup::disableTimeRef()` allows to disable the on-flight TRB reference time subtraction.

By default, the data from the spares are not stored, and the reference time is subtracted.

4.2.3 Calibration and Cal Data Level

Once the data is unpacked and the raw level is reached, the calibration task is performed and the already calibrated output data is then stored in the category `HRpcCal`. We assume that calibrated data are those data with are given in physical units so that they have some meaning.

The full tRPC calibration is done by the class `HRpcCalibrater`. This class takes the data from `HRpcRaw` category, runs the algorithms and saves the output in `HRpcCal`. Three main magnitudes have to be calibrated, namely: position, charge and time-of-flight:

4.2.3.1 Position Calibration

The longitudinal position along each tRPC cell is calculated by the time difference between both ends (left and right ends). The X coordinate of a hit in the cell reference system is the given by:

$$X_{cell} = \left[\left(\frac{t_{left} - t_{right}}{2} \right) + postionOffset \right] \cdot V_{prop} \tag{4.1}$$

where t_{left} and t_{right} are the two measurements of a cell (in ns), V_{prop} is the signal propagation velocity (in mm/ns) and the $positionOffset$ is the parameter to be calculated (which depends only on the cable lengths).

The first step is the conversion of the TDC bin units into time units. This is done by applying the conversion factor of the TRB working in low resolution mode, which is 0.097 ns/bin.

The signal propagation velocity is calculated in the following way: the left-right time difference is histogrammed, in ns, for each cell and the width of such distribution is calculated as the width at one third of the maximum; then, this value is plot for each cell versus its real length, in mm, obtained from geometry. The slope of the linear fit is the propagation velocity in mm/ns. The average for all cells was calculated to be about 181 mm/ns, and the value of 180 mm/ns ($0.6c$) was taken as standard, according with previous measurements [29, 30]. Fig. 4.1 show two of these fits for two different columns in the same sector. The data set corresponds to cosmic rays. Note that the signal propagation velocity is a feature that depends mainly on the dielectric properties and not on the cell geometry.

The position offset for each cell is also calculated as the middle of the left-right time difference histogram so that X_{cell} distribution is centered at zero.

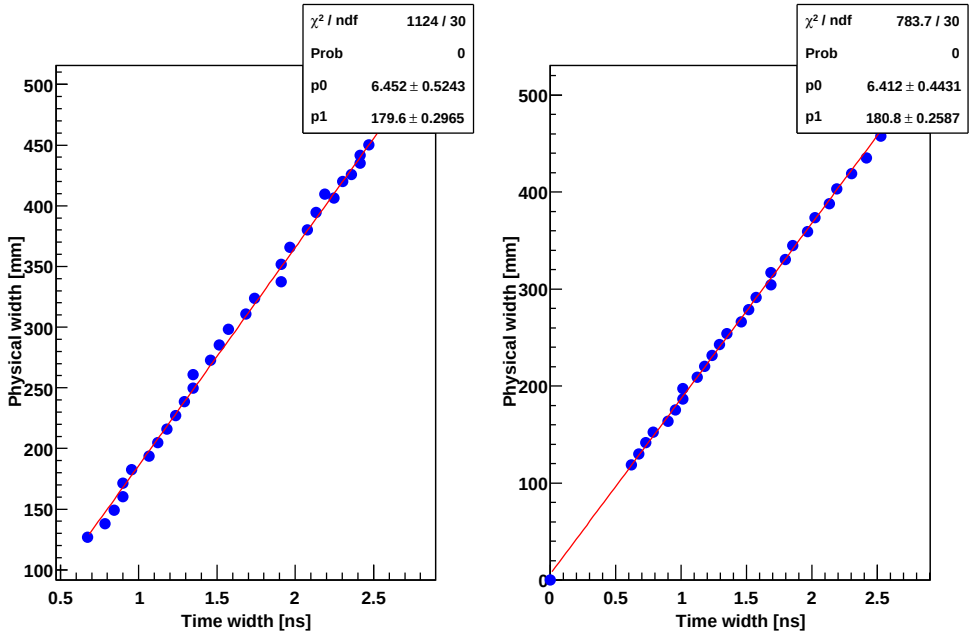

Figure 4.1: Two fits for calculating the Signal Propagation Velocity with cosmic ray data in two different random columns. The velocity is given by the slope of the fit.

Then, by means of geometry, the X_{cell} coordinated is translated into X_{module} coordinate, which gives the position referred to the so-called *module* coordinates system centered in the wall at the perpendicular point from the vertex. Coordinates Y_{module} and Z_{module} are directly obtained from geometry, that is, from the position of a single cell in the wall.

Finally, the coordinates in the so-called *laboratory* reference system are obtained. Thus, X_{lab}, Y_{lab} and Z_{lab} are referred to the vertex position.

Fig. 4.2 shows the reconstructed hit position in the laboratory reference system after the full position calibration procedure for real data.

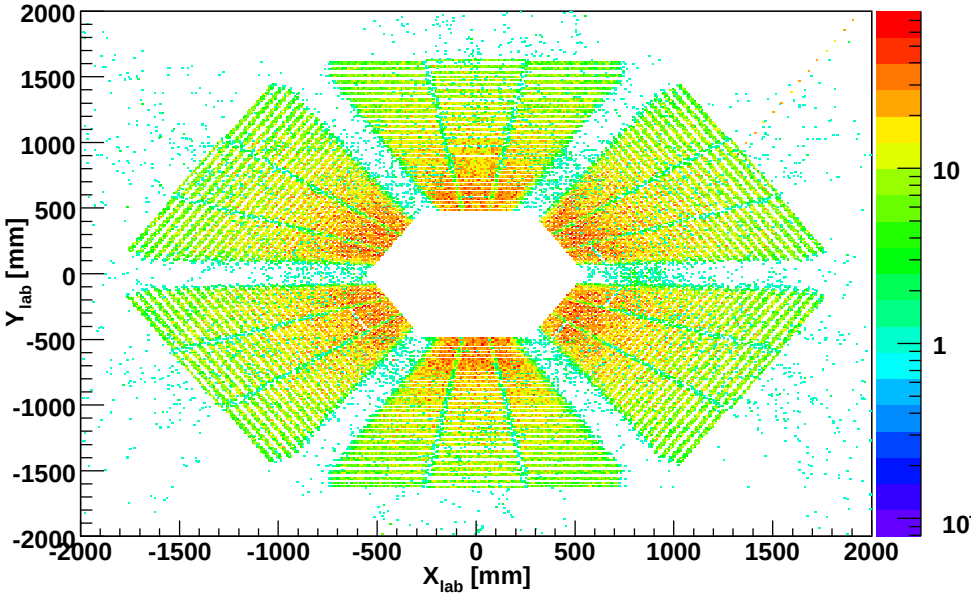

Figure 4.2: tRPC Hit Position in laboratory system for no field data

4.2.3.2 Width to Charge Calibration

The induced charge (see Section 2.2.5) by a particle giving signal in the tRPC cells is encoded in the width of the FEE (LVDS) output signal through the "charge to width" algorithm [35, 33] and is referred as *QtoW*. The QtoW measurement is therefore delivered in TDC bin units. That is why the reverse process is mandatory: first, as each single FEE channel has a slightly different behaviour, the QtoW pedestal is subtracted to all measurements. These pedestals are calculated by a method that searches for the beginning of the QtoW histogram on each channel. As they are cell-depending, they are stored as parameters in the `HRpcCalPar` container; then, the TDC bin units are first translated into ns (multiplying by the TDC-time conversion factor) and then into physical units (fC) through the parameterization performed

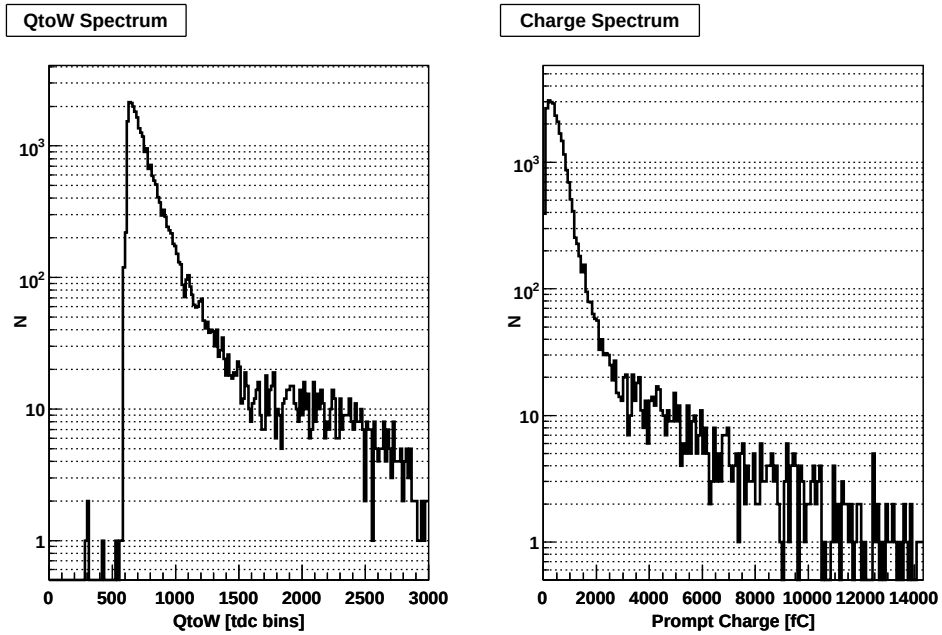

Figure 4.3: QtoW and Charge Spectra for beam 17 sep 2010

in [35]. Such parameterization is stored in a dedicated condition-style parameter container called `HRpcQtoWPar`.

Fig. 4.3 shows a typical QtoW spectrum before the calibration, in raw units (left), and after this calibration procedure (right).

4.2.3.3 Time-of-Flight Calibration

The Time-of-Flight Calibration (*tof*) is also applicated to the data in the `HRpcCalibrater`, so that the `HRpcRaw` category contains the already calibrated *tof* values. Although a new *tof* calibration algorithm is foreseen for the tRPC wall, by means of the overlap information between layers, the calibration for the current beamtimes was performed in a cell-by-cell way.

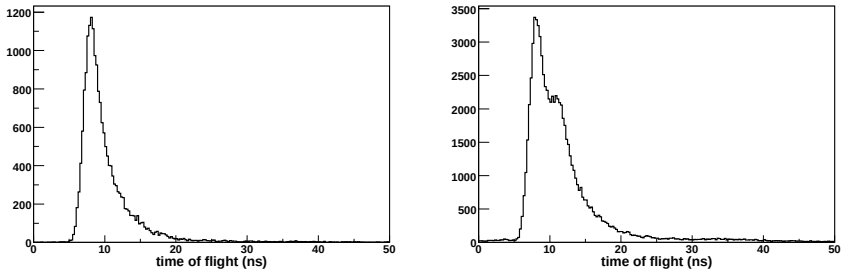

(a) (b)

Figure 4.4: Calibrated Time-of-Flight Spectra for real data: (a) no magnetic field data and (b) high magnetic field data, where the effect of the field is apparent

It was developed in two main steps. At the very beginning, the data must be translated from TDC bin units into ns in the usual way. Then, in the first step calibration, the time measurements per each cell are hitogrammed. The time measurement is calculated as the sum of both time ends divided by two. The "fast" peak of such distribution is placed roughly at 7 ns, which is the time for the fastest particle to travel from the interaction point to the tRPC wall, and the corresponding *timeOffset* is calculated. In the case that the Start detector time is available, it is subtracted to the tRPC measurement. Thus, the *tof* is calculated as:

$$tof = \left[\left(\frac{t_{left} + t_{right}}{2} \right) + timeOffset \right] \tag{4.2}$$

where all values are given in ns. The result of the first step calibration for real data (*sep10* beamtime) is shown in Fig. 4.4, both for no magnetic field data (left) and high magnetic field data (right).

In the second step of *tof* calibration, a fine tunning of the parameters is done. For doing that, those tracks that match with a ring in the Rich detector are selected, that is, a lepton selection is performed. Then, the *normalized* time-of-flight, $\overline{tof}$, spectra are drawn for each cell. The $\overline{tof}$ is calculated to be independent of the traveled track length as it is given by:

$$\overline{tof} = tof \cdot \frac{2100mm}{track\ lenght} = 7ns \tag{4.3}$$

The offset of each of the $\overline{tof}$ with respect to the value of 7 ns is then calculated, and the correction is applied to the previous set of parameters. Note that 7 ns is the *tof* of an electron that travels along 2100 mm with a velocity of $\beta \approx 1$, and 2100 is the average distance from the META detectors (TOF+tRPC+Shower) to the target.

4.2.4 Hit Finding and Hit Data Level

Once the *cal level* is reached, the hit finding task can be called. Such task is performed in the class `HRpcHitF`. This class gets the data from the `HRpcCal` category, run the corresponding methods, and stores the output in the `HRpcHit` category. Thus, the *hit level* is reached.

Basically, `HRpcHitF` performs two main operations:

Hit Position Finding The X_{cell} coordinate is calculated by multiplying the calibrated left-right time difference stored in `HRpcCal` by the signal propagation velocity. Then, the corresponding coordinate transformations are applied and the hit coordinates in *module* and *laboratory* systems are calculated and stored in the `HRpcHit` category, as well as the corresponding angular coordinates θ_{lab} and ϕ_{lab}.

Hit *tof* Finding The hit *tof* is calculated by correcting the calibrated *tof* from `HRpcCal`. In the current design, only a correction depending on the cell geometry is applied, but it is foreseen to include also the charge and position corrections.

The geometry parameter container `HRpcGeomPar` is mandatory for initialize the hit finding task.

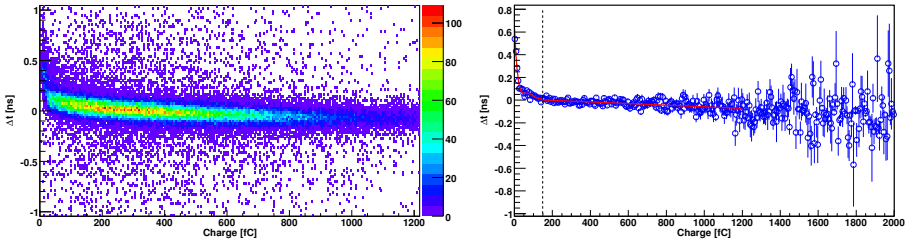

(a) (b)

Figure 4.5: Slewing Correction: (a) dependency of the time measurement (time difference between overlapped cells in this case) with the charge and (b) polynomial fitting (red line) to the same data as in (a) averaged per each bin (blue points). A good agreement between fit and data is achieved. The dashed black line shows the cut point for the two different fits.

4.2.4.1 Slewing Correction

Besides, in the hit finding task is performed the so-called *slewing correction*. This correction tries to minimize the time-charge dependency of the measurements (see sections 2.2.3 or 6.5.2 for a description of the effect) improving the final time resolution of the system in $\sim$20 ps.

An example of the time-charge dependency is shown in Fig. 4.5 (a): the time difference between two overlapped cells is plotted versus the charge of one of them. As the stronger deviation occurs at very low charges, it was parameterized in two segments, where the value of $Q = 150$ fC was chosen to separate them. Before that breaking point, the dependency was fit to a 5th order polynomial function, and a straight line (1st order polynomial function) was used for the fit of the outer region, as it is shown in Fig. 4.5 (b). Thus, six plus two parameters are enough to parameterize the correlation per each cell.

In order to really obtain the contribution of the charge of a single cell, first the charge contribution of the second cell is removed from the time difference (in fact, by using the same parameterization) and then, the final parameterization is done.

4.2.5 Cluster Finding and Cluster Data Level

The last level of elaborated tRPC data is the so-called cluster level, stored in the category `HRpcCluster`. The cluster finding task is run via the class `HRpcClusterF`. There, a cluster searching algorithm is developed.

A cluster is defined when a particle crosses two overlapped cells and both have a hit within a given position and time window (specified in the `HRpcClusFPar`). Then, both the position and the `tof` of the cluster are calculated as the average of the single measurements.

If there is an overlapped hit which fulfills the searching algorithm requirements, the cluster size is 2 and the cluster is labeled, otherwise, the single hit is also treated as a cluster of size 1 in the `HRpcCluster` category, and simply the `HRpcHit` values are copied there.

4.2.6 Digitization and Simulated Data

HGeant is the simulation package for HADES, built upon the GEANT program from CERN [64]. The purpose of HGeant is to simulate the detector response of the HADES spectrometer to the passage of charged particles.

HGeant does not simulate any ion collision. For that purpose, external programs called event generators, like PLUTO or UrQMD are used. HGeant reads information given by event generators and propagate the outgoing particles through the HADES spectrometer. It is also allowed to generate simple tracks by hand, using the C++ interpreter embedded in HGeant, either in an interactive session or with a macro.

HGeant provides a way to read the geometry describing the spectrometer, including both the geometrical shapes and material composition of detectors. It makes that we can simulate the different physical effects affecting particles passing through matter, like energy loss, multiple scattering, secondary particles production, bremsstrahlung emission, etc.

HGeant mostly records information about the particle transversing the different detectors and uses the HYDRA facilities to write its output in different categories depending on the sys-

tem. That category for the tRPC is called `HGeantKine`. There, the simulated hit information over the wall is stored.

In order to analyze the simulated data within the full HYDRA chain, they must be first transformed into detector-like output, that is, for instance, from the charge given by geant to a QtoW measurement. That task is the *digitization*, and it is called for the simulated data. The class which does the task for the tRPC is the `HRpcDigitizer`.

In the current design, the `HRpcDigitizer` connects the simulated data with the cal level, storing the output in the categroy `HRpcCalSim`, which inherits from `HRpcCal`, and then the data is propagated to `HRpcHitSim` and `HRpcClusterSim` as if they were real events. At the end, the user can compare the simulated values from `HGeantRpc` with the result of analyze them within HYDRA.

Basically, in the `HRpcDigitizer`, the simulated data (tof, X, Y, Z, charge, etc) are transformed into left and right time measurements for each cell, as well as both QtoW measurements, and the tRPC intrinsic fluctuations are added. More details of the digitization method for the tRPC can be found in [65].

The `HRpcDigiPar` parameter container is mandatory for the digitization task.

It is foreseen a modification for this design as two different digitization tasks are going to be developed. On the one hand, the main, and "official", `HRpcDigitizer` will connect simulated data directly with the hit level; on the other hand, an new class `HRpcDigitizer2` must be written in order to connect the simulated data with the raw level. This new variation can be used for private debugging of the tRPC wall.

4.2.7 On-line Monitoring

A new framework for HADES On-line Monitoring has been recently developed at GSI and included within HYDRA in the *online* module. The server is based in ROOT tools with a custom-made format for an easy implementation. Each detector has its own monitor where the developer adds the histograms and calls for the main methods

`createHistsDetectorname()` and `fillHistsDetectorname()`. Then, the histograms have to be added to the Monitor Graphical User Interface (GUI). This is done through an eXtensible Markup Language (XML) application. Thus, the GUI with the defined histograms is created dynamically by parsing an xml file.

Within this new framework, the most important histograms for the tRPC have been included. That set of histograms allows to a quick online diagnosis of the tRPC wall just by having a look at the histograms. Each tab of the tRPC GUI window is clearly labeled and ranges from the very raw data, like TDC channel counting, to the most elaborated data, like hit distribution in lab frame. Fig. 4.6 (a) shows the first window (main window), where the multiplicity histograms are drawn, while Fig. 4.6 (b) shows the $X-Y$ distribution in the *module* reference system per sector. All other windows are labeled in the tabs at the top.

4.2.8 Quality Assessment Plots

One of the HYDRA modules is fully dedicated to perform the quality assessment plots (QA) during the so-called Data Summary Tape (DST) process: when a set of files with raw data, taken during an specific beamtime, is ready to be processed (all necessary algorithms and parameters are available), starts the physics analysis itself. Then, a DST is carried out. The analysis is processed via analysis macros that contains the necessary parameters and the task list that one wants to run. The diagnosis plots are needed to check in a reasonable fast way the quality of the analysed DST files. It is expected to have better parameters and improved algorithms per each DST generation for the same run. The output of the QA is saved both in root files and in a pdf file.

The QA plots for the tRPC were included in the *qa* HYDRA library. Those includes the multiplicity per event, the hit distribution per sector and in the laboratory reference system and the tof spectrum, as the reader can see in page 80, where the main tRPC qa page is included.

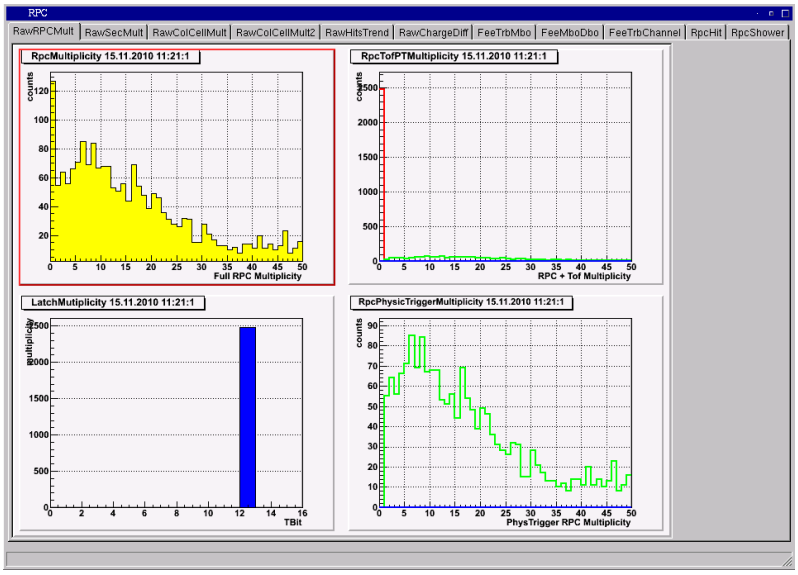

(a)

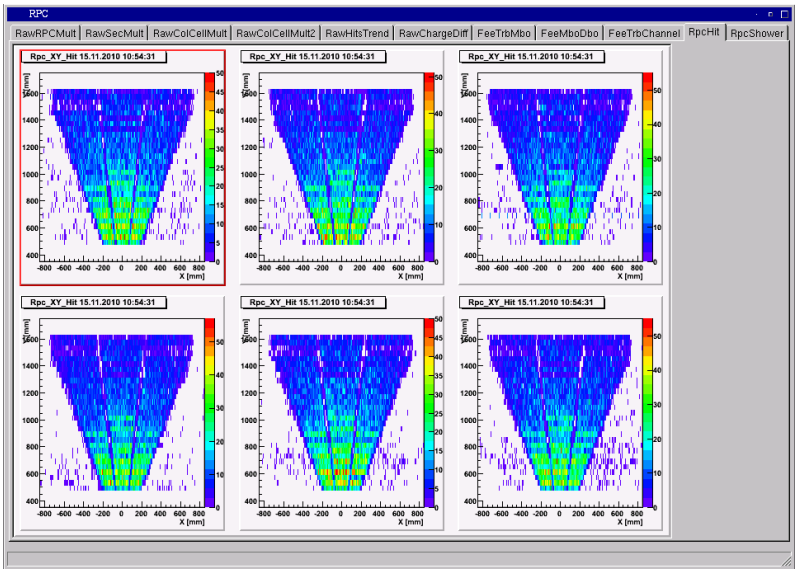

(b)

Figure 4.6: (a) Main tRPC online window. There, the basic multiplicity information is plotted, in this case for beam data when the tRPC was not in the trigger. (b) X-Y distribution per sector in the *module* reference system for the same set of beam data. All the tRPC plots can be reached from the tabs in the upper part of the window

In addition, some Particle Identification plots with the tRPC are included in the so-called *Particle Candidate* page. There, the tof for leptons, the correlations with Shower detector or matched tracks info are also drawn.

4.3 Reconstruction initialization

In the following lines, an example of a macro for initializing the tRPC event reconstruction within HYDRA is given. There, among others, the tRPC tasks are set to "real", which means by default that all the chain will be reconstructed up to *cluster* level. If no tasks are set at all, only the unpacking is performed.

```
//-------------------------------------------------------------------------
//-------------------------------------------------------------------------

//
// Author: P.Cabanelas
// Description: Macro for initializating the tRPC event reconstruction
//
// usage:
// root[0] .L macro.C
// root[1]  run()

Bool_t run()
{
//-------------------------------------------------------------------------
// CHANGE ONLY THIS SECTION
//-------------------------------------------------------------------------

//Parameter ascii file input
TString ParInputFilename1("/path/asciiParFile.txt");

TString asciiParFile =ParInputFilename1;
```

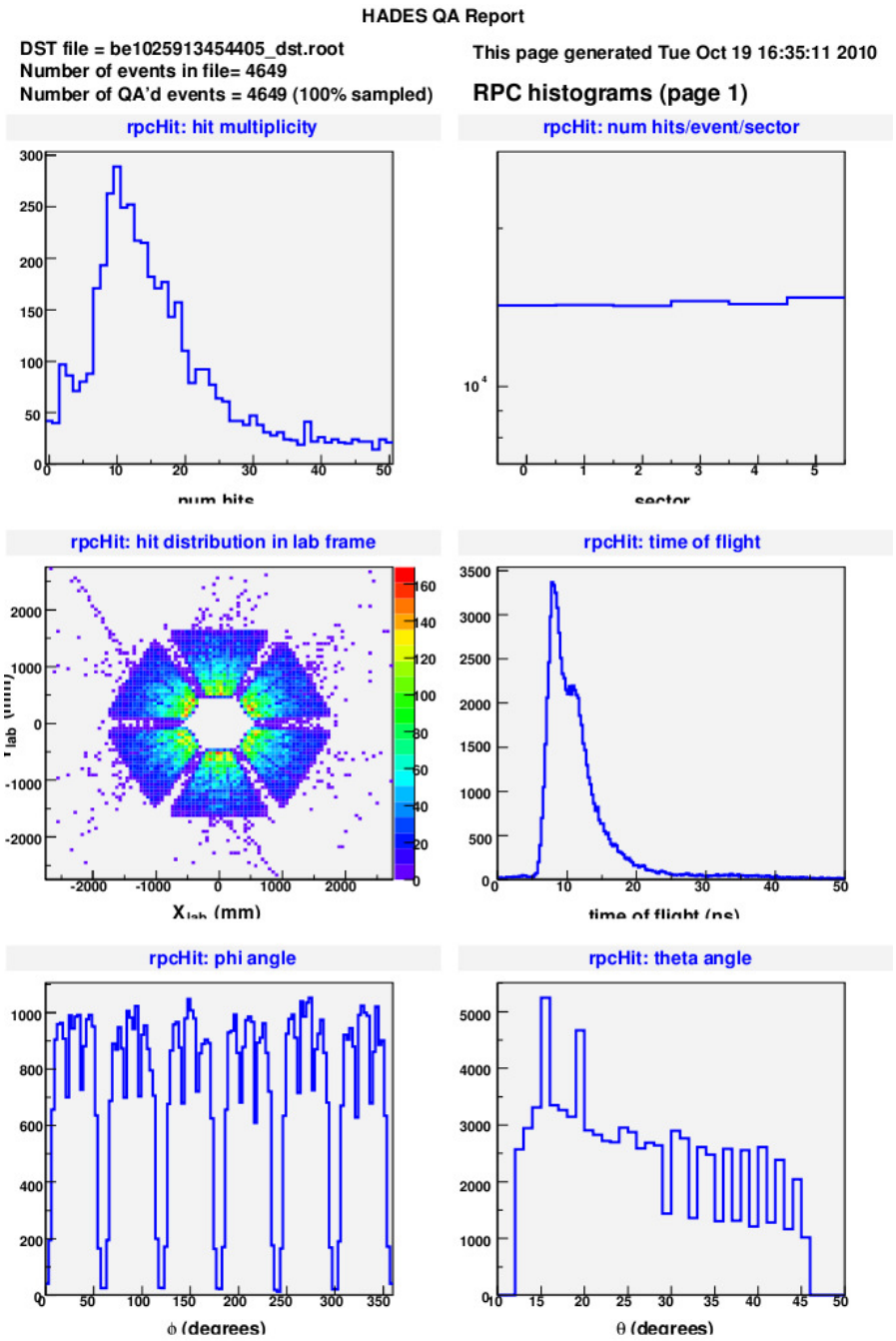

Figure 4.7: tRPC QA histograms main page: hit category multiplicity (up-left), hit numbers per sector (up-right), X-Y ditribution in lab system (mid-left), time-of-flight spectrum (mid-right), ϕ coordinate in lab (down-left) and θ coordinate in lab.

```
//Parameter root file input
TString rootParFile  ="/path/rootParFile.root";

//ORACLE parameter input
Bool_t ora_input =kFALSE;
Bool_t param_file=kFALSE;

//Directory of raw data
TString inDir("/data_path/");

//Raw data file number
TString inFile("bexxxxxxxxxxx.hld");

//Number of events to be proccessed
Int_t nEvents=800000000;

//Set output file
Hades *myHades   = new  Hades;  //pointer to the main HADES class object
myHades->setOutputFile("/out_path/outFile.root","RECREATE","Test",2);

//------------------------------------------------------------------------
//------------------------------------------------------------------------
// NO NEED TO CHANGE FROM HERE ON
//------------------------------------------------------------------------

Int_t nStartEvent=1;
Int_t nRefId = 1;

//Rpc TRB-HUBs IDs
Int_t rpcUnpackers[2] = {0x8400,0x8410};

//Rpc active modules per sector
Int_t rpcMods[1] = {1};

//Getting runtime database
```

```
HRuntimeDb *rtdb = myHades -> getRuntimeDb();

//Getting spectrometer
HSpectrometer* spec = myHades->getSetup();

//Rpc configuration
spec->addDetector(new HRpcDetector);
for(Int_t sec=0;sec<6;sec++) {
 spec->getDetector("Rpc")->setModules(sec,rpcMods);
}

//Parameters input
if (!asciiParFile.IsNull()) {
 HParAsciiFileIo *input1=new HParAsciiFileIo;
 input1->open((Text_t*)ParInputFilename1.Data(),"in");
 rtdb->setFirstInput(input1);
}

if (!rootParFile.IsNull()) {
 HParRootFileIo *input2=new HParRootFileIo;
 input2->open((Text_t*)rootParFile.Data(),"READ");
 rtdb->setSecondInput(input2);
}

if(ora_input) {
 HParOra2Io *ora=new HParOra2Io() ;
 ora->open();
 ora->setHistoryDate("now");

 if (!ora->check()) {
  Error("ora->check","no connection to Oracle \n exiting...!");
  exit(EXIT_FAILURE);
 }

 if (asciiParFile.IsNull() && rootParFile.IsNull()) {
```

```
  rtdb->setFirstInput(ora);
 } else {
  rtdb->setSecondInput(ora);
 }
}

if(param_file) {
 if (!rtdb->makeParamFile("oraParFile.root","sep10test",
         "20-AUG-2010 00:00:00","30-SEP-2010 00:00:00")) {
  delete myHades;
  exit(EXIT_FAILURE);
 }
}


//Data source
HldFileSource *source=new HldFileSource;
source->addFile((Text_t*)(inDir+inFile).Data(),nRefId);

myHades->setDataSource(source);

//Rpc unpackers
for(UInt_t i=0; i<(sizeof(rpcUnpackers)/sizeof(Int_t)); i++)
{
 HRpcTrb2Unpacker *rpcTrb2Unpacker = new HRpcTrb2Unpacker(rpcUnpackers[i]);
 rpcTrb2Unpacker->setQuietMode();
 rpcTrb2Unpacker->setDebugFlag(0);
 rpcTrb2Unpacker->setDebugFlag1(1);
 //rpcTrb2Unpacker->storeSpareChannelsData();
 //rpcTrb2Unpacker->disableTimeRef();
 source->addUnpacker(rpcTrb2Unpacker);
}

//----------------------- Task Set -------------------------
HRpcTaskSet *rpcTaskSet = new HRpcTaskSet();
```

```
//asking by default for all tasks up to cluster finding
HTask *rpcTasks = rpcTaskSet->make("real");

HTaskSet *masterTaskSet = myHades->getTaskSet("real");
masterTaskSet->add(rpcTasks);

//Initilize reconstruction
myHades->makeCounter(10000);

if (!myHades->init()){
 Error("init()","Hades did not initialize ... once again");
 exit(1);
}
rtdb->print();

//Getting pointer to the current event
// and disabling categories to the output
HEvent *event = gHades->getCurrentEvent();
event->getCategory(catRpcCal)->setPersistency(kFALSE);
event->getCategory(catRpcCluster)->setPersistency(kFALSE);

//Enabling root Tree in the output
myHades->makeTree();

//Printing info
Int_t nProcessed = myHades->eventLoop(nEvents,nStartEvent);
printf("Events processed: %i\n",nProcessed);

delete myHades;

}
//-------------------------------------------------------------------
//-------------------------------------------------------------------
```

In addition to what was exposed in this chapter, there were also developed the needed tools and methods (or macros) to analyze the data whatever it was their level. Such tools allows to the user to have, for instance, a quick and easy view of the quality of data and detector status at any time, giving information about noisy channels, hot spots in the detector, left-right cell counting or preliminary resolution and efficiency analysis, just by analyzing a few recorded events.

Chapter 5

First Full Prototype Testing

5.1 Introduction

During October 2008, a prototype sector of the final HADES tRPC Wall design was fully instrumented and mounted at the nominal position. The system was then exposed to the realistic particle environment present at the HADES experiment.

The most important features of the HADES RPC Wall were measured showing very good performances and stability. Two small scintillators were placed before and after the RPC Wall in order to get the intrinsic efficiency of the detector. Besides, the HADES tracking system as well as the Shower detector were operative. This allowed to perform the full track reconstruction through the spectrometer and therefore to perform also tracking efficiency measurements for the RPC Wall.

The results from this test were shown at the X International Workshop on Resistive Plate Chambers, at Mumbai, India, in 2009, and are also published in [30].

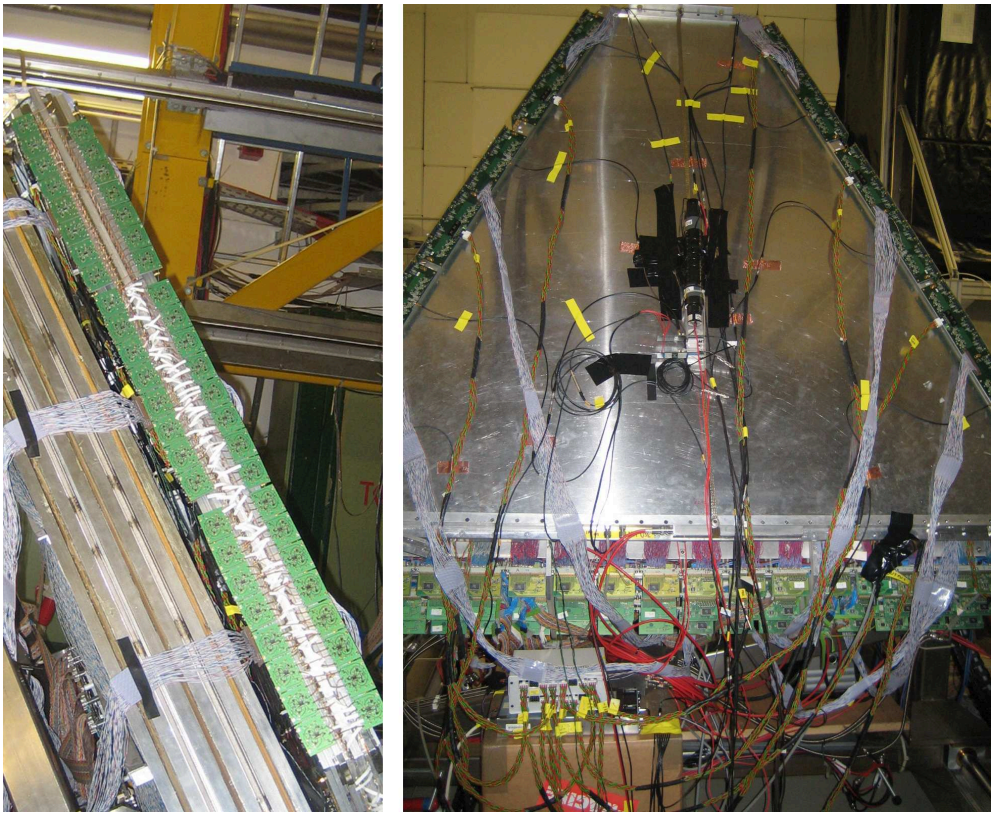

Figure 5.1: Lateral and front view of the tRPC sector on its support, standing over the Pre-Shower detector.

5.2 Setup

Data was taken with an RPC sector (sextant) exposed to secondaries from reactions of a C beam of 2 AGeV, with an effective spill duration of ~ 6 s, on Nb and Be targets. A detailed description of the structure can be found on [54]. It was mounted on its support (see Fig. 5.1) and placed approximately at the nominal position, between the Pre-Shower (RPC downstream) and MDC (MultiWire DriftChambers) detectors. The RPC was operated with a gas mixture composed of 90% $C_2H_2F_4$ and 10% SF_6 under a continuous gas flow of 50

cc/min at a nominal High Voltage of 5800V. 162 cells, distributed in 27 rows, were readout by the Front End Electronics (FEE) and Data Acquisition System described on sections 3.2.4 and 3.3.4. The last four rows of cells in the region at high polar angle were not read out due to a technical problem. Additionally, some of the electronics channels, on random locations, were not operative.

The last outer MDC chamber (MDCIV) was operational together with the Pre-Shower detector belonging to the same sector, allowing for the selection of reference particle tracks over the RPC wall. The magnet and RICH were off. In order to provide a reliable reaction trigger, we operated the present TOF and TOFino walls (with exception of the sector instrumented with the RPC) with a low-bias trigger in multiplicity larger than 4 ($\langle N \rangle \simeq 10$). Some low statistic runs were also taken with triggers from 2 reference small scintillators directly sticked before and after the RPC, as one can see in Fig. 5.1 right, covering a small vertical region belonging to 4 RPC cells.

5.3 Methods

5.3.1 Definition of the reference tracks and alignment

A set of reference tracks was defined as those tracks that matched both the MDC tracking system and the Pre-Shower detector within a window of $\Delta X_{match} = \pm 35$ mm in X (along the azimuthal angle) and $\Delta Y_{match} = \pm 35$ mm in Y (along the polar angle).

Due to the non standard position of the RPC, a few centimetres backwards from the nominal position, it was necessary to make a careful alignment. This was done by minimizing differences between the position of the reference tracks on the RPC plane and the position given by the RPC itself, X_{res} and Y_{res}. The RPC hits were associated with a given track selecting the one at the minimum distance R_{res}, defined as $R_{res} = \sqrt{X_{res}^2 + Y_{res}^2}$. The complete procedure can be summarized as follows:

1. X and Y position of a reference track given by the RPC was calculated as:

$$X_{rpc} = \frac{t_l - t_r}{2} v_{prop} + X_{offset} \tag{5.1}$$

where t_l and t_r are the measured times left and right for each cell, v_{prop} is the signal propagation velocity in the cell and X_{offset} is an offset calculated individually for each cell. Y_{rpc} was calculated as the centrer of the hit cell obtained from its physical position. The propagation velocity was calculated as:

$$v_{prop} = \frac{2D}{W(t_l - t_r)} \tag{5.2}$$

where $W(t_l - t_r)$ is the width of the distribution of $t_l - t_r$ and D is the physical dimension of the cell.

2. The RPC was aligned by centring and minimizing the rms of the X_{res} and Y_{res} distributions. The free parameters in this procedure are: Z (RPC position downstream along the sector rails), Y (RPC position along the polar angle) and Θ (angle that quantifies the deviations from the perfect parallelism with respect to the Pre-Shower). The other 3 free parameters needed for positioning a volume in space were assumed to be fixed for the sake of different symmetries.

3. After the alignment procedure, the propagation velocity was re-obtained by correcting the remaining residual dependence of X_{res} with X. Small deviations from the previously obtained value were identified and corrected.

5.3.2 Matching and Intrinsic Efficiencies

The matching efficiency was obtained on a given region as the ratio of the number of RPC hits, within a position window $\Delta Y = \pm 35$ mm and a time window ΔT of 400 ns, and the number of reference tracks. T represents the time with respect to the trigger signal given by the TOF + TOFINO wall (no start detector available). This time did not represent a time of flight but could be used to suppresses random matches.

The intrinsic efficiency was calculated as the fraction of RPC hits in coincidence with the scintillators, within a time window of 400ns.

The matching efficiency is shown in two different representations. The 2D representation, which corresponds to the efficiency as a function of X and Y, and the 1D representation, which corresponds with the projection of the 2D representation on the Y axis.

5.3.3 Intrinsic spatial resolution

The intrinsic spatial resolution was calculated for those tracks that cross two overlapping cells by obtaining the σ of the distribution:

$$\Delta X_{up-down} = \frac{v_{prop}}{2}\left[(t_l - t_r)\,|_{up} - (t_l - t_r)\,|_{down}\right] \tag{5.3}$$

where *up* and *down* denote the two overlapping cells on different layers. Assuming equal resolution for both cells, the spatial resolution for a single cell is $\sigma_x = \sigma(\Delta X_{up-down})/\sqrt{2}$.

For those cells that geometrically overlap with two cells, the distribution of $\Delta X_{up-down}$ was merged together and the σ_x of the resulting distribution was calculated. A similar procedure was used to calculate the average spatial resolution of the entire sector or for a region of special interest.

5.3.4 Time resolution

The time resolution was calculated for those tracks that cross two overlapping cells by characterizing the distribution:

$$\Delta T_{up-down} = \frac{1}{2}\left[(t_l + t_r)\,|_{up} - (t_l + t_r)\,|_{down}\right] \tag{5.4}$$

In order to characterize the resulting non Gaussian distribution, the σ of a Gaussian fit within $\pm 1.5\sigma$ about the mean of the original distribution, $\sigma\Delta T_{up-down}|_{\pm 1.5\sigma}$, as well as the amount of events beyond $\pm 3\sigma$ (named "3σ tails") were calculated. Events beyond ± 700 ps are also reported, as this is the expected π and K Time-of-Flight difference [66]. Assuming

equal resolution for both cells, the time resolution for a single cell is

$$\sigma_t = (\sigma \Delta T_{up-down}|_{\pm 1.5\sigma})/\sqrt{2} \tag{5.5}$$

This distribution was calculated after performing two corrections, as a function of position and charge. For cells overlapping with two other cells and for regions of special interest, a similar procedure as described on sec. 5.3.3 was used.

5.3.5 Dependence on rate

A few runs were taken at different beam intensities. Moreover, as the rate within the sector varies exponentially as a function of the polar angle, it was possible to measure different rate values on the RPC for the same run.

Cells were grouped in 6 regions, with equal number of events, along the polar angle. For each region, the rate was calculated as the average rate in the region, the time resolution was calculated as the σ_t of the merged distributions of $\Delta T_{up-down}$ for the cells in the region and the matching efficiency was calculated as the average of the matching efficiency in the region. The intrinsic efficiency was just calculated for the available runs at different rates.

Owing to the low statistics available for these runs, the position as well as charge corrections were parametrized from runs with higher statistics and applied to these.

5.4 Results

Fig. 5.2 shows the X_{res} distribution for the reference tracks, within a ΔY window of ± 35 mm, after RPC alignment. The σ of the distribution, $\sigma_{X_{res}}$, including tracking and RPC resolution, is 10.2 mm.

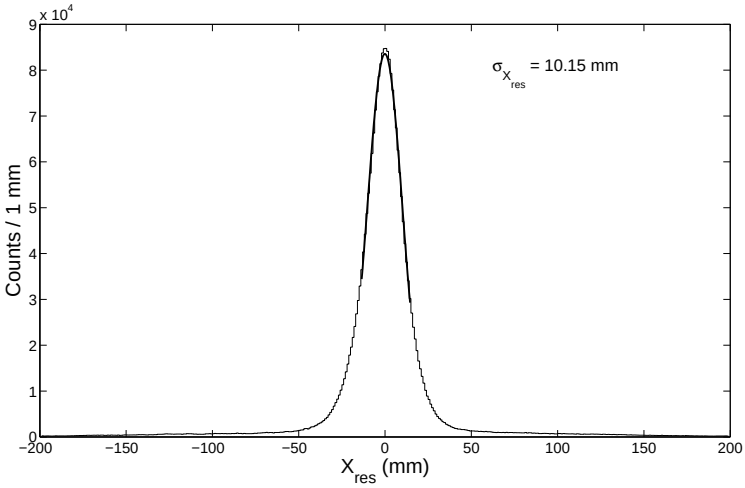

Figure 5.2: X_{res} (difference between the X coordinate of the reference track and the RPC X coordinate, see 5.3.2), distribution for the reference tracks, after RPC alignment. A tracking resolution of $\sim$10 mm (σ) is obtained.

5.4.1 Efficiency

Fig. 5.3 shows the 2D matching efficiency for reference tracks within a ΔY window of $\pm$35 mm. The slanting lines separating the 3 columns are non-active regions in the RPC (counts in this region come from the imperfect resolution of the reference tracks).

Fig. 5.4 shows the 1D matching efficiency for each of the columns. The average efficiency is 97.4% (excluding non-operative channels). It also shows the intrinsic efficiency obtained with the scintillator for the same conditions (black short line at the middle of the centre column) reaching a value of 99%.

Fig. 5.5 shows the matching efficiency for different values of the window ΔY, showing an almost constant value for windows larger than $\pm$35 mm. The smooth increase for large windows can be attributed to double hits, which contribute to the efficiency as the window increases. It also shows the efficiency when a matching windows in X, $\Delta X = \pm$50 mm, is required. In this situation the efficiency drops down to 96.5%. The difference can be

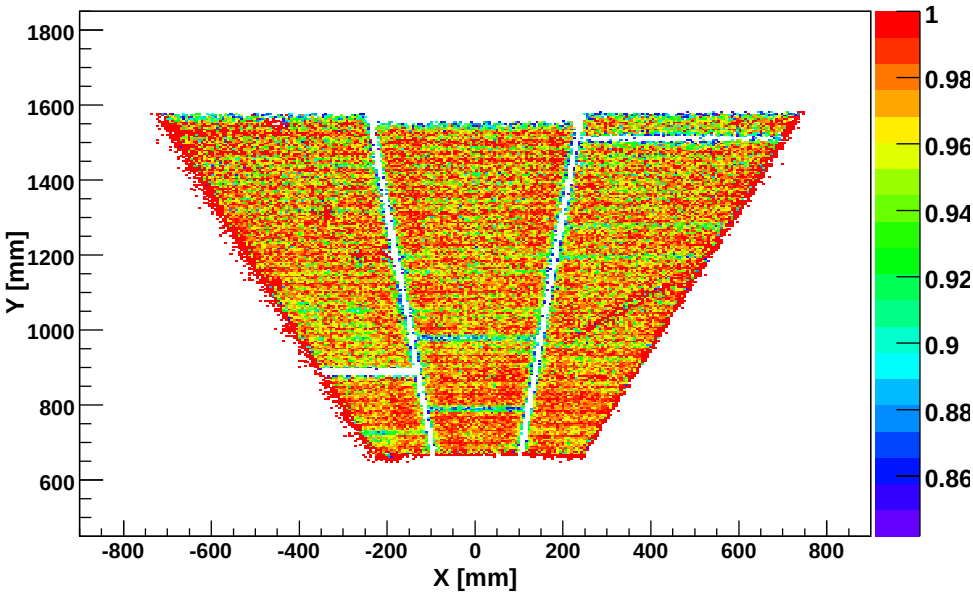

Figure 5.3: 2D matching efficiency scan. Dead regions between columns are visible.

attributed to the small amount of double hits (occupancy per event $= 1.5\%/\text{cell}$) excluded when this window is imposed and the position misidentification error on X in the cells where only one of the signal (left or right) is available.

5.4.2 Intrinsic spatial resolution

Fig. 5.6 shows the uncertainty σ_x as a function of the row number and Y for left, centre and right columns. Rows lower than 5 are not shown because the sector was a few centimetres backward from the nominal position and this region was shaded by the frame of the tracking system. In addition some cells were not available because the respective FEE channels were inoperative (to calculate position or time both t_l an t_r for each cell are required). There are two regions clearly identified for rows higher and lower than 20, the latter being characterized by

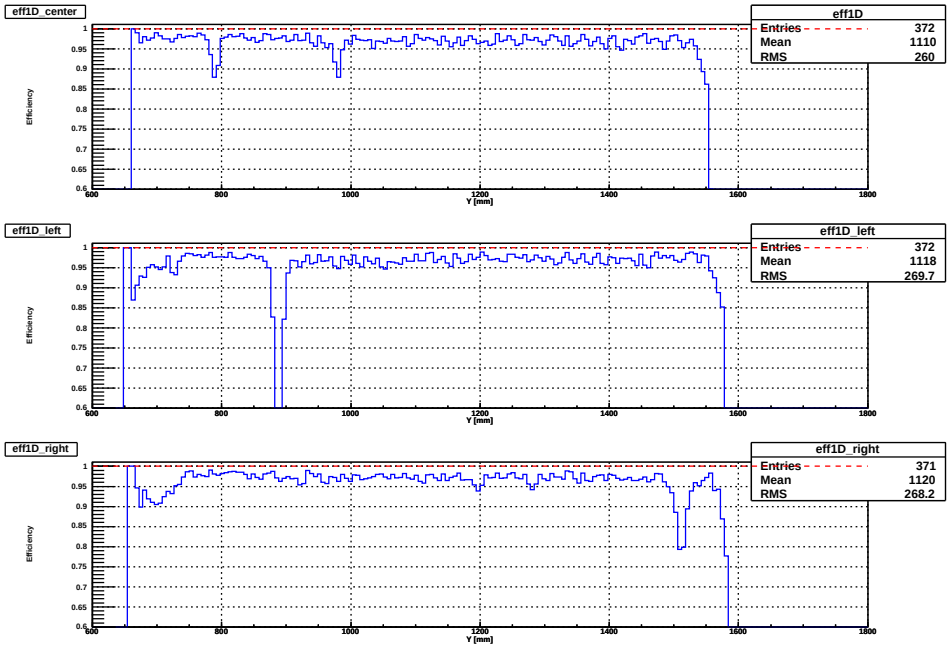

Figure 5.4: 1D matching efficiency for the three different columns. The average values are 97.4% excluding the non operative channels. The value of intrinsic efficiency obtained with the scintillators, 99%, is also shown.

non-perfect shielding of the signal feed-throughs, which results in a higher level of crosstalk by roughly a factor 3 [54]. The difference, although not critical is ~ 2 mm (the upper numbers on each plot on Fig. 5.8 denote the σ_x of the merged distributions for the cells belonging to each region separated by the vertical black line). The global spatial resolution for the whole sector is 7.7 mm (σ). This number can be compared with $\sigma_{X_{res}}$, 10.2 mm, suggesting a good resolution of the tracking system as it is strongly influenced by the intrinsic spatial resolution of the RPC.

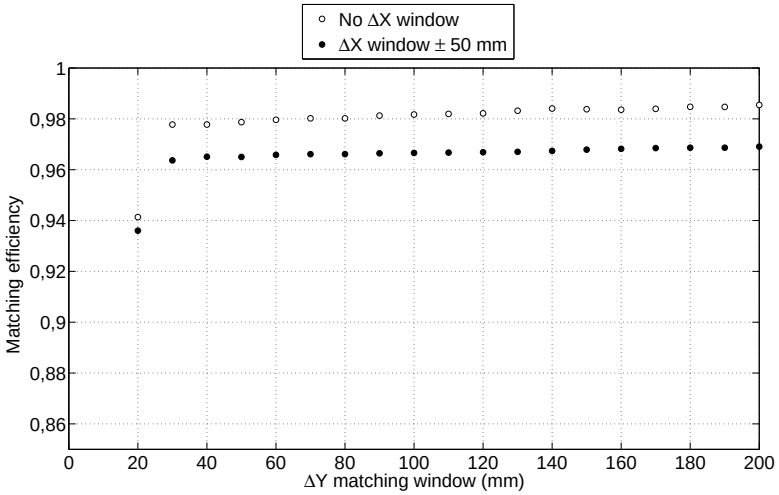

Figure 5.5: Average matching efficiency as a function of ΔY window with and without ΔX window.

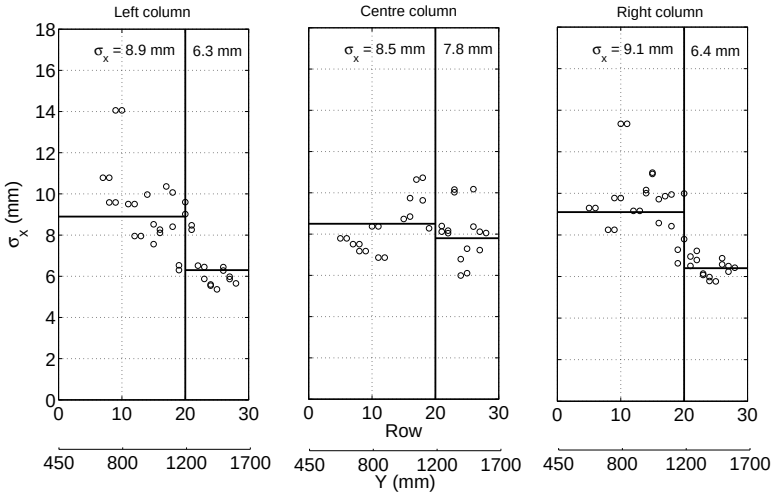

Figure 5.6: σ_x as a function of row number and Y for the three columns. Numbers on the upper part of the plots correspond to σ_x of the merged distribution of the rows left and right of the vertical line. The horizontal lines illustrate these numbers.

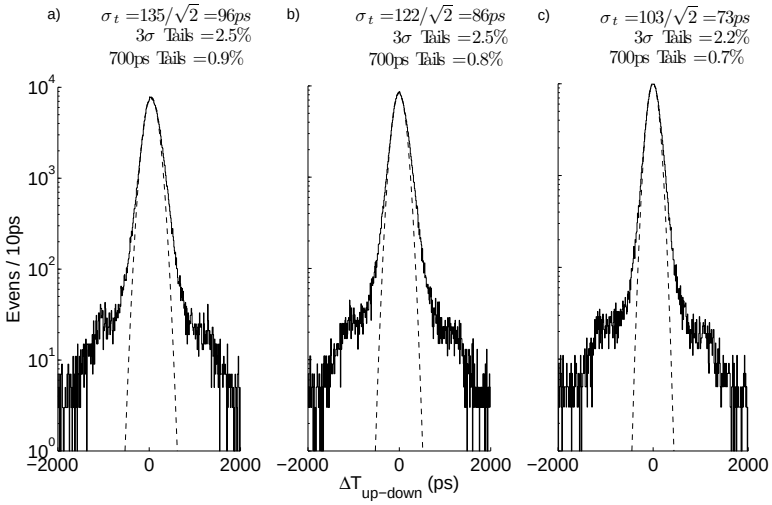

Figure 5.7: $\Delta T_{up-down}$ distributions a) without corrections b) after position correction and c) after charge correction for the entire sector.

5.4.3 Time resolution

Fig. 5.7 shows the $\Delta T_{up-down}$ distribution a) without corrections b) after position correction and c) after charge correction for the whole sector, showing an improvement of σ_t from 96 to 73 ps. Tails are at a level of 0.7% above 700 ps and 2.2% above 3σ. The partial overlap of the layers completely eliminates longer-time tails for a large fraction of the hits [67].

Fig. 5.8 shows the time resolution σ_t as a function of the row number and Y for left, centre and right columns. Again the difference between rows higher and lower than 20 is clear (see sec. 5.4.2), mostly on the lateral columns. Although the worsening is not dramatic, it is consistently at a level of 10 ps (the upper numbers on each plot on Fig. 5.8 denote σ_t of the merged distributions for the cells belonging to each region separated by the vertical line). There are a few randomly positioned cells with clearly worse resolution $\sigma_t > 100$ ps, some of them correlated with a degradation of the spatial resolution: an observable directly depending

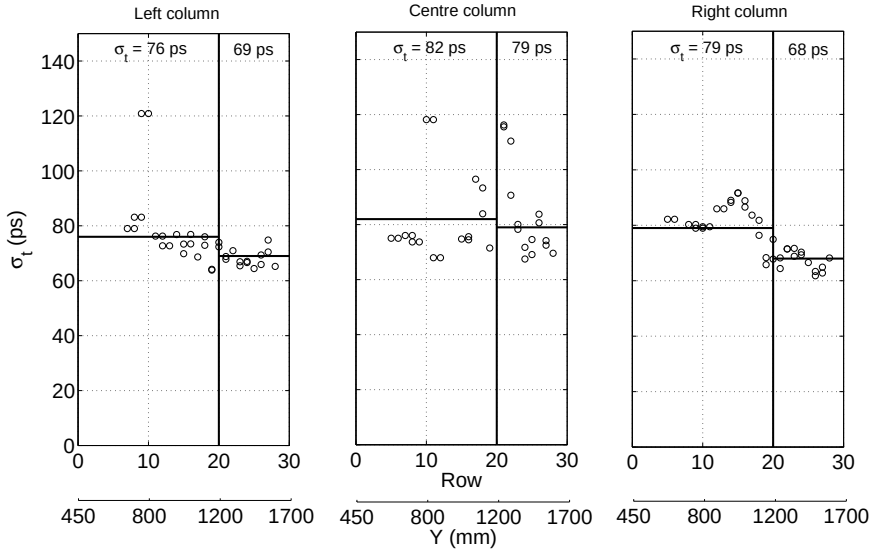

Figure 5.8: σ_t as a function of the row number and Y for the three columns. Numbers on the upper part of the plots correspond to the σ_t of the merged distribution left and right of the vertical line.

on the FEE resolution. This kind of behaviour is not desirable and will be solved on the final sectors by replacing the cells or the FEE channels involved.

5.4.4 Dependence on rate

Fig. 5.9 shows the time resolution, σ_t, as as function of rate; it shows an uniform behaviour, within the available statistics, from a few Hz/cm^2 up to almost 100 Hz/cm^2. The mean value of the data is 73 ps indicating that the parametrization procedure described on sec. 5.3.5 is very robust. Matching and intrinsic efficiencies are also shown at the same rates (the available values for the scintillator only reach 20 Hz/cm^2) showing a constant values of 97.4% and 99% respectively.

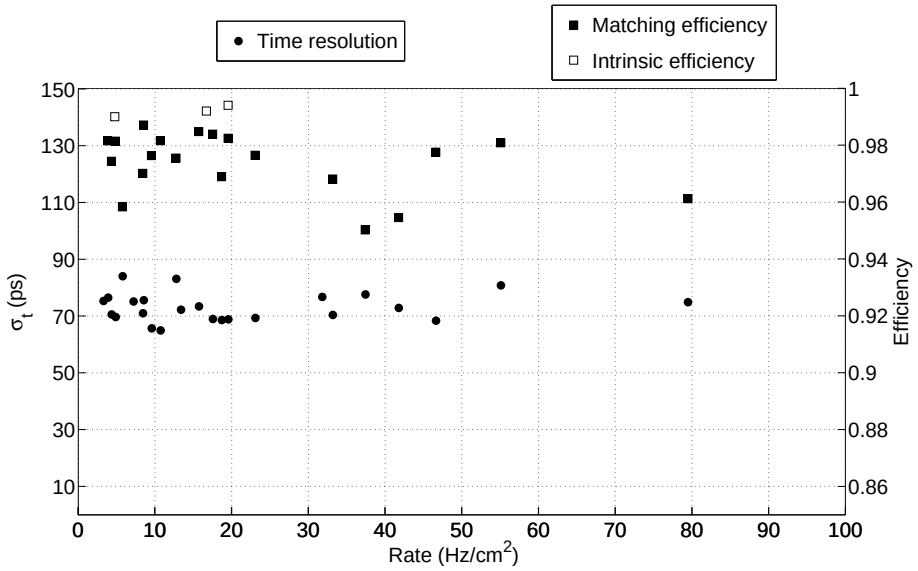

Figure 5.9: Time resolution, matching and intrinsic efficiencies as a function of the rate.

5.5 Conclusions

A full size prototype of the new HADES-TOF wall based on RPCs was mounted and tested successfully in a typical environment (C-Be/Nb) at typical rates ($\sim$ 100 Hz/cm^2).

The measured average matching efficiency was 97.4% in the whole area of the sector and a intrinsic efficiency of 99% in a random spot was also obtained.

The global time resolution was 73 ps σ, exhibiting modest timing tails at a level of 2.2% for 3σ tails, together with an average spatial resolution along the cells of 7.7 mm σ.

No degradation of the efficiency or timing resolution was observed in the range of a few Hz/cm^2 up to almost 100 Hz/cm^2, the typical particle rates present in the HADES environment.

Chapter 6

Performances of the HADES tRPC cells under C^{12} beam

6.1 Introduction

There is a broad range of newly born applications where multi-gap timing RPCs (tRPCs or MtRPCs) need to work in highly ionizing environments. Maybe the most remarkable one is the detection of annihilation γ's for Positron Emission Tomography (PET) [68] (based on the detection of the secondary electron produced either by Compton or photo-electric effect). More recently, in the framework of the R^3B collaboration, two main projects started R&D aimed at building large ToF walls for neutron and ion detection, respectively [69, 70]. Both of them will have to deal with a yet unexplored range of highly ionizing particles.

Remarkable success has been achieved in describing the behavior of these chambers through first principle avalanche simulations, revealing the main role of a very strong avalanche Space-Charge [40, 71, 72]. Despite the presence of this complicated phenomena, a handful of analytical expressions can be obtained if standard avalanche evolution is assumed to happen up to the threshold level [72, 73, 36, 37, 74]. The developed formalisms allow to estimate the

influence of the ionization loss, hereafter referred in mips units ($\Delta E/\Delta E_{mips}$) as:

$$\bar{t}(\Delta E) = \frac{t_{rise}}{\ln 9} \ln \frac{\Delta E_{mips}}{\Delta E} + t_{off}(n_{th}, t_{rise}) \tag{6.1}$$

$$\sigma_T(\Delta E) = K_1 \frac{t_{rise}}{\ln 9} \sqrt{\frac{\Delta E_{mips}}{\Delta E}} \tag{6.2}$$

$$\varepsilon(\Delta E) = 1 - \exp\left[-n_o \left(1 - \frac{\eta}{\alpha} - \frac{\ln(1 + \frac{(\alpha-\eta)}{E_w} n_{th})}{\alpha g} \right) \frac{\Delta E}{\Delta E_{mips}} \right] \tag{6.3}$$

where $\bar{t}$ refers to the average and σ_T to the rms of the time response distribution (for the sake of simplicity it has been assumed to be Gaussian, so that $\bar{t}$ can be thought of as the maximum of the time response distribution and σ_T equals its rms). n_{th} is the electronics threshold in number of electrons, n_o is the total number of primary ionizations for mips, g the gap size, α and η the multiplication and attachment coefficients respectively, E_w the weighting field and K_1 is an adimensional constant of order unity that contains the effect of avalanche multiplication statistics. The signal rise-time t_{rise} is related to the coefficients of the electron swarm as:

$$t_{rise} = \frac{\ln 9}{(\alpha - \eta) v_e} \tag{6.4}$$

in absence of Space-Charge effects (see [37] for a discussion). The average electron drift velocity is denoted by v_e. Typical values of $t_{rise} \simeq$ 200-250 ps at threshold level have been measured with a careful setup [29, 21], for typical operating fields of $E = 100$ kV/cm, and threshold levels of $q_{th} = n_{th} q_e \simeq 10$ fC. It must be noted that, within the models, eq. 6.1 is generally exact, being eq. 6.2 fulfilled in the limit $\Delta E/\Delta E_{mips} \to \infty$ and, contrary, eq. 6.3 for $\Delta E/\Delta E_{mips} \to 1$ (otherwise the latter must be re-interpreted as a lower limit [74]). Despite the development of analytical tools, no systematic attempt was done to clarify these dependences with exception of the controverted data from [75] and [76], that will be re-visited here, and the much too short survey of [73] (only 2 points).

It must be added that the generally worst performance of long counters as compared with small chambers strongly suggests that issues like signal transmission, bandwidth to noise ratio of the electronics and the nature of the time-charge correlation may have a more practical

decisive role in large counters than the above-mentioned considerations, at least resolution-wise. As an example, the much improved time resolution expected for 0.511 MeV photon response [77] (dominated by the highly ionizing Compton electrons ejected from the anode) seems to render too short in describing the observed performances, being those experimentally worst than mips [78].

On the other hand, the energy loss dependence of $\bar{t}$ should keep its integrity with a large independence from the characteristics of the signal transmission and amplifier bandwidth whose effect is anyway common . Actually, such a dependence may have a big impact impact in the overall resolution if the average energy lost ΔE can not be accessed by other means. Part of dependency can be restored if the signal amplitude carries information on the initial ionization, by resorting to the time-charge slewing correction. Unfortunately, the intrinsic non-proportional nature of parallel geometries together with the presence of a very strong avalanche Space-Charge makes this correlation between the initial ionization and the signal amplitude much weaker than in plastic scintillators, for instance, were standard CFD reduce this effect to a large extent. It is very difficult to address these questions regarding energy loss dependence from a theoretical point of view and no study regarding these issues remains undisputed.

The detection of ions up to $A = 200$ ($Z \simeq 100$) over large surfaces ($\simeq 5$ m^2) at relativistic kinetic energies $E_K = 700$ GeV/A has recently brought attention in the R^{3}B experiment, proposed within the new Facility for Anti-proton and Ion Research (FAIR) at Darmstadt, Germany [69]. In view of this potential new application, we conducted systematic measurements at GSI-SIS18 for evaluating the detector response under ions up to charge state $Z = 6$. Complementary, measurements with a highly mono-energetic diffuse proton beam ($E_K = 1.76$ GeV, $\sigma_{E_K}/E_K = 4\%$) and cosmic rays were also performed. Spare cells from the HADES system were used [30] and comparisons to previous results will be referred when appropriate.

Importantly, parallel plate geometries (of the kind of PPACs) have been used for many years for detecting ions at the 100 MeV energy scale or below with great success [79, 80, 81]. Apart from extending the time resolution below 100 ps, the introduction of the RPC tech-

nology should greatly improve the chamber stability and make easier its construction, being intrinsically 'spark-protected' at ambient pressure. As shown in this work, these features are already provided by typical tRPC designs if ions have enough energy to penetrate in a relatively bulky detector ($\simeq 20\%X_o$ here) and ion fluxes are below 1 kHz/cm^2.

In this chapter, the three different experimental setups are explained (section 6.1), the behavior as a function of HV and rate is presented in section 6.3, while section 6.4 is devoted to the behavior as a function of particle type, a discussion follows in section 6.5 about the practical use of such a counter in a highly ionizing environment and finally section 6.6 summarizes the conclusions.

A compact version of this chapter has been already published in [82].

6.2 Experimental setup

6.2.1 The tRPC cells

Two 22 $\times$ 140 mm^2 (width $\times$ length) tRPC cells from the new HADES tRPC wall have been used and allocated inside their corresponding shielding profiles (acting as Faraday cages) in a custom designed aluminum gas box, as it is shown in Fig. 6.1. As compared with the HADES system, the gas box was lacking of an optimized PCB for signal feed-through of $Z_o = 50\Omega$ (characteristic impedance) while the routing of the signals inside the box was such that they could be read out from the same box side. Electrical isolation of signal cables was ensured whenever possible in order to reduce cross-talk. A full description of the HADES tRPC cells can be found in section 3.2.3, and more technical details can be found in [54].

The read-out was based on the HADES FEE electronics mentioned is section 3.2.4. The detector was read out in single-ended mode, with a signal being taken from the central electrode (anode) after filtering the HV level. No special care was taken for matching the detector impedance ($Z_d = 12 \pm 2\Omega$) to the coaxial LEMO cables used for signal transmission ($Z_o = 50\Omega$), while the FEE built-in dead-time of the order of 50-70 ns provided stability to

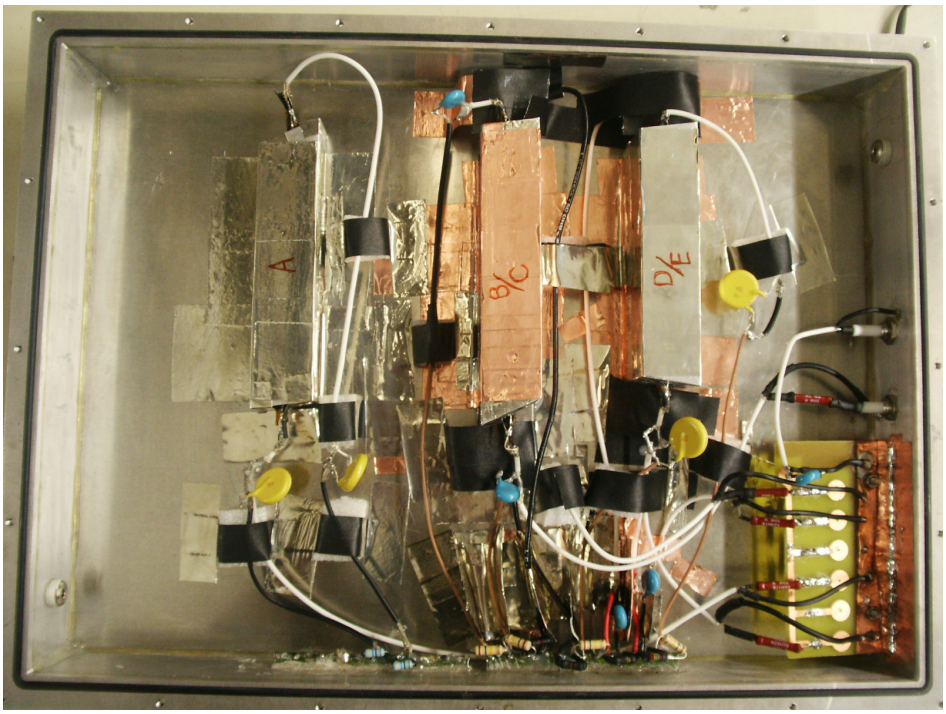

Figure 6.1: Detail of the box containing the HADES tRPC cells and their corresponding electronics. Although five cells were allocated inside the box, only two of them were used for data taken.

the electronic chain by avoiding re-triggers caused by reflections. 2 MBs (Mother-Boards) and 2x2 DBs (Daughter-Boards) [83] fed by the customized low-ripple distributed LV system from section 3.3.2 were used for reading-out 8 electronic channels (2×2 tRPC cells and 2×2 reference scintillators). The tRPC-FEE thresholds were set to $v_{th} = 50$ mV (equivalently $v_{th} = 50/40 = 1.25$ mV and $q_{th} \simeq 30$ fC at the pre-amplifier input) and were not changed during the measurements. The gas box was used as a central ground node being the FEE, HV and cathode strips connected to it by screws and/or conductive meshes. With this grounding scheme the external noise levels were still modest and indeed for $v_{th} < 20$ mV some chan-

nels were unstable. The digitization and event building was done with the TRB treated in section 3.3.4.

The oxygen content measured at the output of the gas box was below 200 ppms (measured with an Oxygen Transmitter O2X1 of GE Infrastructure Sensing) for a gas flow of 150 cc/min of an isobutane-free gas mixture based on $C_2H_2F_4/SF_6$ (90/10). Due to the high electronegativity of the gas mixtures used for timing such ppm levels are not expected to influence the detector behavior.

6.2.2 The trigger and reference system

The arrangement of the tRPC cells and reference scintillators is shown in Fig. 6.2. Two fast Bicron scintillators BC-420 and BC-422 read out in both ends by Hamamatsu H6533 photo-multipliers (PMs) were used for providing trigger, reference time and track selection for efficiency studies. The scintillator-PM assembly was placed inside PVC tubes of 50 mm diameter and optical silicone was applied to the contact surface scintillator-PM while the scintillator was wrapped in silver paper to improve light transmission. Such a detector choice had previously yielded $\sigma_T = 35$ ps per counter for mips [26].

For the scintillators readout the HADES FEE was also used with the pre-amplifier being by-passed in virtue of the PM amplification. The PMs were operated at a nominal voltage $V = -2.2$ kV for which the average signal amplitude was just slightly higher than that of tRPC signals after amplification. Variations around the nominal voltage were introduced to account for slight differences in the characteristic gain curves of the different PMs. The same threshold as in the tRPC-FEE was used.

A setup with the 4 counters (2 tRPCs and 2 scintillators) being placed vertically along their longest side was chosen. The scintillators, being prisms of dimensions $10 \times 20 \times 100$ mm^3 (BC-422) and $10 \times 30 \times 120$ mm^3 (BC-420) were stacked over their narrower faces (10×100 mm^2 and 10×120 mm^2, respectively). They could be aligned with an estimated precision of the order of ± 2 mm. A similar procedure was followed with the tRPC cells.

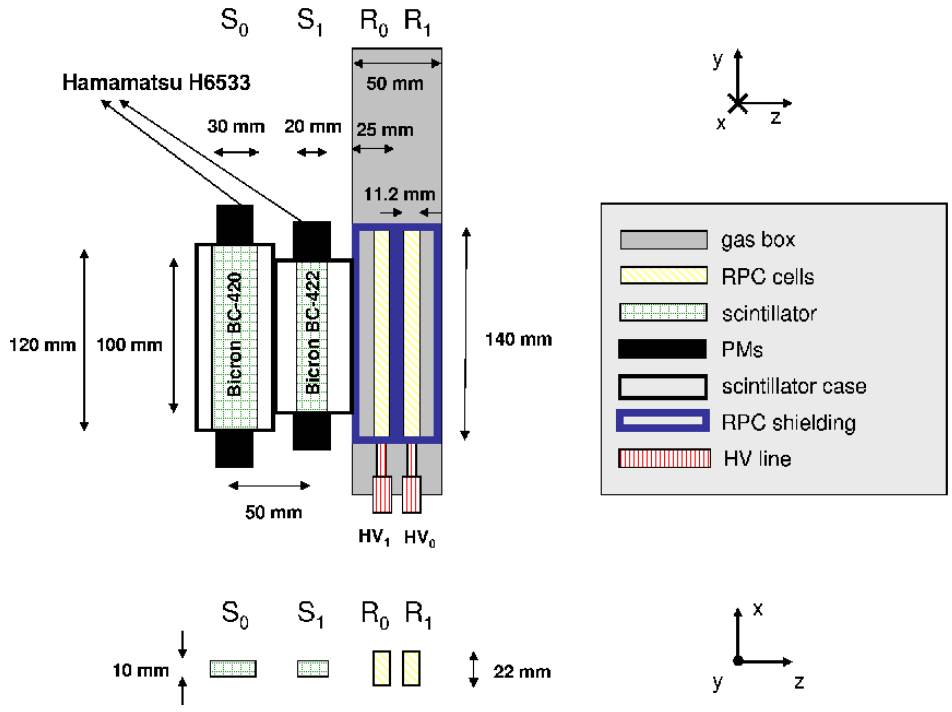

Figure 6.2: Different views of the arrangement of the reference scintillators and tRPC cells used for the measurements.

Being mechanically identical and placed inside aluminum profiles, both tRPC cells can be easily stacked with a mutual alignment better than 1 mm. The reference system was carefully centered with respect to the tRPCs in order to provide a good reference for efficiency estimates. Requesting an additional coincidence with one of the ('reference' in such case) tRPC is expected to compensate for any error on the aforementioned procedure and was done when possible (measurements of section 6.2.5.2).

For all the measurements the trigger was provided by a coincidence of the 4 PM output signals. In order to do that the PM outputs were split, with one being sent to a Leading

Edge Discriminator (LED) while the other was fed directly into the FEE after by-passing the amplifier, both discriminators having the same threshold.

Additionally to the scintillator reference system, two diamonds of the HADES START detector were operative and placed 14 m upstream, roughly at the focal plane of the last HADES beam-line quadrupole. The surface dimensions of the detectors were 4.7×4.7 mm^2 and 3.5×3.5 mm^2 and their individual time resolutions in the range 100-150 ps [84]. Although not in the trigger because of technical reasons, a coincidence probability of 10% was observed off-line, allowing for an improved track selection and energy spread determination. Those were used only in a reduced set of the measurements (section 6.2.5.2).

6.2.3 Prompt charge determination

The electron induced (prompt) charge q_p was codified in the width of the FEE (LVDS) output signal through the 'charge to width' algorithm mentioned in section 4.2.3.2 and is referred as $QtoW$. Despite the non-linearity of the method, avalanches and streamers can be well resolved (Fig. 6.3-right) and appear separated at around $q_p \simeq 5$ pC ($QtoW = 250$ ns). This 'QtoW method' can indeed accommodate a very large dynamic range while keeping the charge resolution below 10%-σ for avalanche-like pulses with $q_p > 50$ fC.

The bi-linear behavior of the average signal width ($\overline{QtoW}$) as a function of the average prompt charge ($\bar{q}_p$) can be embodied in a simple parameterization as [33]:

$$\overline{QtoW} = a(1 - e^{-b\bar{q}_p}) + c\bar{q}_p + QtoW_{min} \tag{6.5}$$

after which the resolution of the 'QtoW method' can be obtained:

$$\frac{\sigma_{q_p}}{\bar{q}_p} = \frac{\partial \bar{q}_p}{\partial \overline{QtoW}} \frac{\sigma_{QtoW}}{\bar{q}_p} \tag{6.6}$$

$$\frac{\sigma_{q_p}}{\bar{q}_p} = \frac{1}{abe^{-b\bar{q}_p} + c} \frac{\sigma_{QtoW}}{\bar{q}_p} \tag{6.7}$$

where $QtoW_{min}$ (53 ns for the channel shown in Fig. 6.3) is the minimum output signal width, corresponding to the minimum time during which the comparator is being self-latched. By

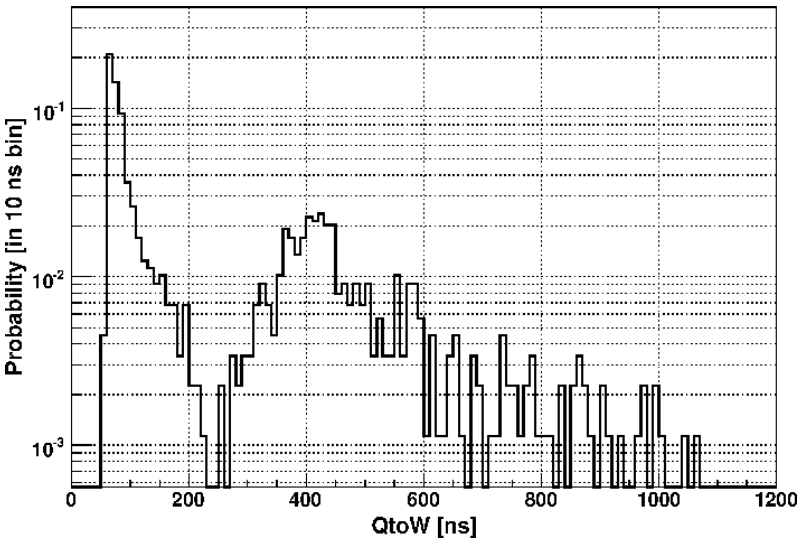

Figure 6.3: *QtoW* distribution measured in one of the tRPC cells used under cosmic rays for an operating voltage $V = 6.0$ kV. The two separate distributions (before and after 250 ns) can be attributed to avalanches and streamers.

numeric integration of the signal amplitude, a close agreement for the *QtoW* vs q_p curves was observed when analyzing avalanches originated inside the detector as compared with pulser data, while streamers clearly deviate from the pulser behavior (up to a factor 1/2 less in the reconstructed q_p). The fluctuations of the signal width are of the order of $\sigma_{QtoW} = 200$ ps and no dependence with the input charge was observed. A detailed description of the performances of the final HADES-FEE can be found in [33].

Eq. 6.5 provides an accurate phenomenological description and illustrates the different behavior of the algorithm for low and high charges, but cannot be inverted, so in practice a 6^{th} order polynomial was used to obtain the 'calibration curve' $q_p(QtoW)$. To avoid errors resulting from an incorrect extrapolation, values of the signal width in excess of 290 ns are considered as an 'overflow' and the maximum pulser charge of $q_p = 25$ pC is assigned to

them. Such big charges are rarely achieved under ordinary circumstances and they occurred seldom even in the very harsh environment studied here.

6.2.4 Total charge and rate determination

The dynamic behavior of an tRPC at high rates is bound to the average total avalanche charge $\bar{q}_T$ [85, 86]. Being readily obtainable by a direct current measurement (after dividing by the avalanche rate), its value is directly related to the average gap voltage once the stationary (DC) situation is reached, as:

$$\bar{V} = V - \bar{I}R = V - \bar{q}_T \Phi \rho d \tag{6.8}$$

with Φ the avalanche flux [in Hz/cm^2], ρ the electrode resistivity and d its thickness. V is the applied voltage, $\bar{I}$ the average current and R the electrode resistance. As compared with the stationary (DC) situation described by eq. 6.8, the interpretation of $\bar{q}_T(t)$ during the stabilization of the field in the gap is more intricate [87].

Although it is not the main focus of the present work to study the transient behavior of the tRPC cells, proper means for determining the average avalanche charge as a function of the irradiation time were devised as follows. The particle rate was measured from scintillator S_1 as the coincidence of signals from its two PMs. This provides an unbiased rate estimate by suppressing single electron noise. The coincidence signal was sent to the scaler input of a commercial LabJack U3 acquisition board connected to a computer, and its value stored every 0.2 s. Complementary, the tRPC current was measured via the analog output of a 2-channel CAEN N471A HV supply, after calibration. Although the HV-display resolution is ± 1 nA, by averaging the analog output the resolution could be improved down to $\simeq 0.5$ nA. Due to the presence of environmental noise, the measured current had to be averaged over a pretty large time interval of $\simeq 0.8$ s being stored every 0.2 s, and read-out with the same acquisition board. With the help of a second scaler input in the LabJack U3, the cycles of an external 40 kHz clock were counted in order to provide a stable time estimate.

6.2.5 The physical environment

6.2.5.1 C^{12} beam

Measurements were performed with three different setups. In a first one (Fig. 6.4a) C^{12} was injected in the experimental area at a kinetic energy $E_K = 1.8$ GeV/A directly from SIS18. The beam was focused at the usual HADES target position, 14 m upstream our reference detectors. The latter were placed close to the beam dump and optically aligned with respect to the beam-line. A typical beam profile at the level of few mm^2 was expected in the target transverse (XY) plane, from which experience tells that the transverse dimension of the primary beam amounts to some cm^2 at the beam dump. The accelerator was operated in the so-called slow extraction mode that allows for a fairly sustained beam intensity along 8 seconds spill (effectively) with a duty cycle close to 50%. Typical spill time-profiles are shown in Fig. 6.5 (left).

The non-perfect detector-beam alignment resulted in a position distribution over the reference scintillator system characterized by a narrow peak (1 cm$-\sigma$) close to one of the detectors ends, submersed in an uniform background (Fig. 6.6-left). After selection based on the signal width in the reference scintillators (Fig. 6.7), the peak could be attributed to the primary C^{12} beam while the uniform background was largely populated by secondary protons and He together with species with $Z = 3,4,5$ (either Carbon charge states or Li, Be, B species), the latter at a much lower yield. Particles different from Carbon must have been originated along the roughly 14 meters downstream from the exit of the vacuum pipe to the detector setup. Due to the different shape of the scintillator signals as compared with tRPC avalanches, the absence of amplifier and the eventual saturation of the PMs at the higher charges, the calibration curve from Fig. 6.3 could not be used and we present in Fig. 6.7 the raw values of the signal width ($QtoW$). Based on them, the identification can be performed with little ambiguity.

The position in the scintillators was determined by constraining the width of the time difference distribution (left-right) to the known detector dimensions. In such a case the prop-

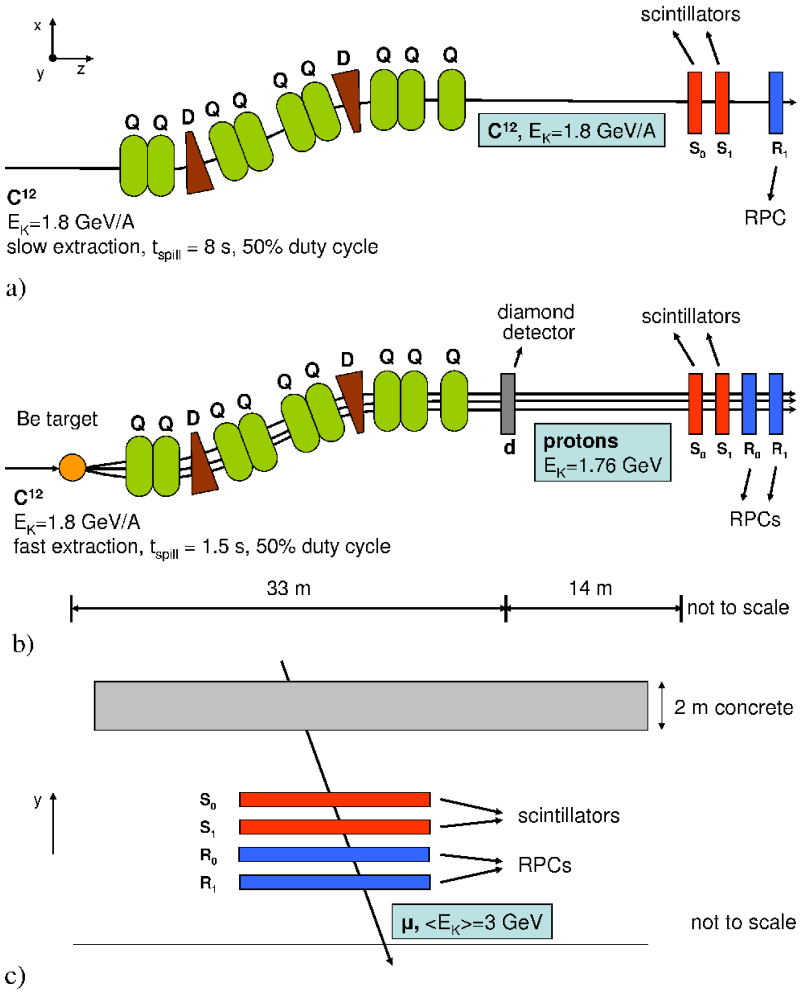

Figure 6.4: a) Setup for focused C^{12} irradiation (kinetic energy $E_K = 1.8$ GeV/A, $\sigma_{E_K}/E_K < 1\%$). b) Setup for diffuse proton irradiation ($E_K = 1.76$ GeV, $\sigma_{E_K}/E_K = 4\%$) after C^{12} reactions in a secondary Beryllium target placed 33 m upstream the experimental hall. Diamond detectors have been added and also a second tRPC (R_o). c) Setup for cosmic muon detection.

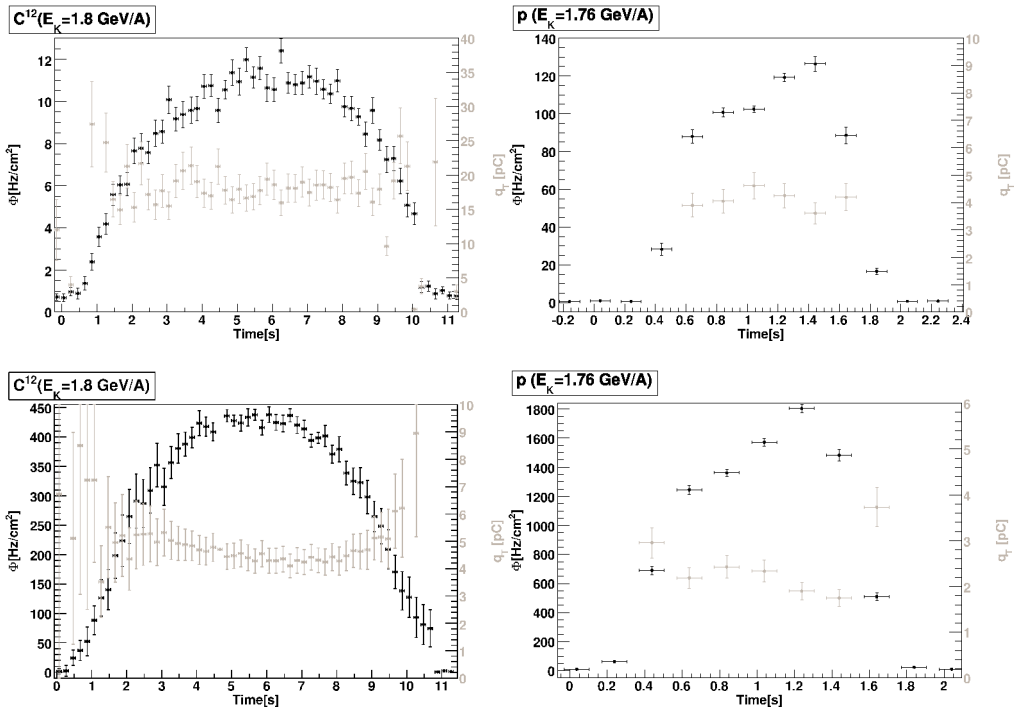

Figure 6.5: Illustration of characteristic spill time-profiles. The left column shows the average flux profile (over many spills) and the average total charge $\bar{q}_T$ behavior (right axis) for illumination with C^{12} (kinetic energy $E_K = 1.8$ GeV/A) at two different beam intensities. Right column shows similar plots for diffuse proton illumination ($E_K = 1.76 \pm 4\%$ GeV). The extraction time was about a factor 5 smaller in such a case. The transient behavior is hardly visible since the measured current had to be averaged over a pretty large time-interval of 0.8 s due to external noise.

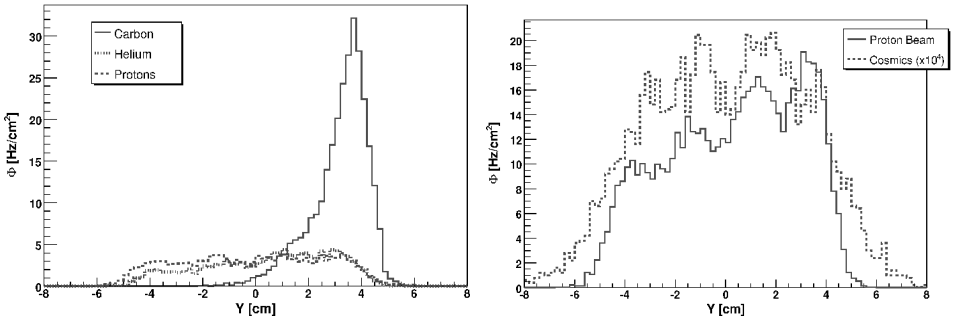

(a) (b)

Figure 6.6: (a) Position distribution along the reference scintillator S_o under C^{12} illumination. The proton, He and C^{12} curves are shown after charge selection, manifesting the primary C^{12} beam (kinetic energy $E_K = 1.8$ GeV/A) close to the border of the reference counters. (b) Position distribution under diffuse proton illumination ($E_K = 1.76 \pm 4\%$ GeV) and cosmic ray profile (overlaid). The slightly bigger profile under cosmic rays stems from the larger angular spread (see text).

agation velocity can be obtained as:

$$v_{prop} = 2\frac{L}{(t_L - t_R)_{50}} \tag{6.9}$$

where $(t_L - t_R)_{50}$ refers to the width of the time difference profile at 50% drop from the flat top. The effective light propagation velocities obtained were $v_{prop,s_o} = 0.385c$ and $v_{prop,s_1} = 0.380c$, being c the speed of light. Finally, the detectors were mutually aligned by software by imposing that the average position difference $(\bar{y}_{s_o} - \bar{y}_{s_1})$ was centered at zero.

Only one tRPC cell (R_1) was used during these measurements since R_o could not be powered up due to technical reasons. A constant voltage $V = 5.6$ kV was applied to the tRPC, while the primary flux ranged from 10 to 1000 Hz/cm^2.

6.2.5.2 Proton beam

In a second setup (Fig. 6.4b), C^{12} at $E_K = 1.8$ GeV/A was collided into a Beryllium secondary target placed 33 m upstream the experimental area. The magnetic field of the following dipoles and quadrupoles in the beam line was adjusted for accepting forward protons from the

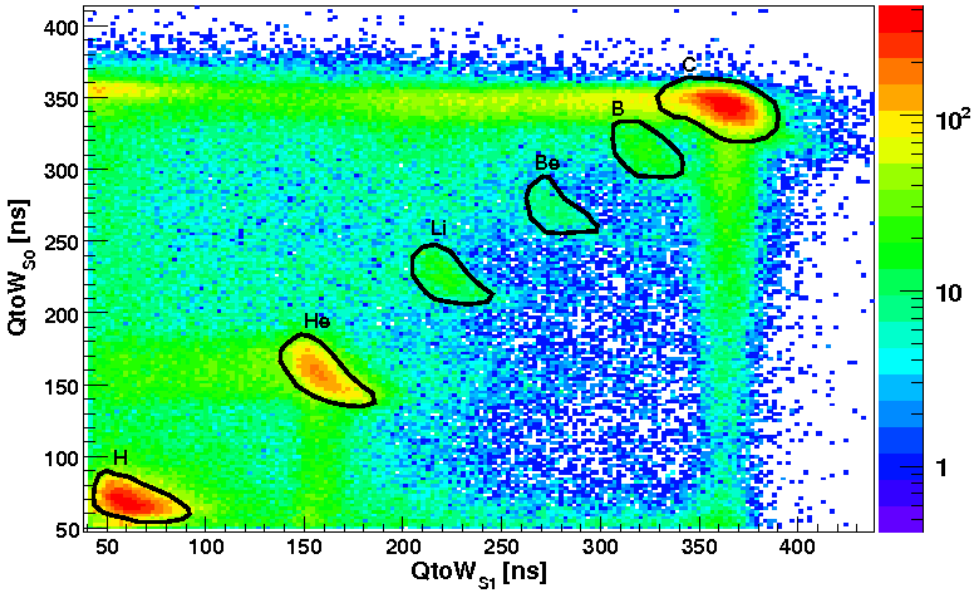

Figure 6.7: Two-dimensional correlation plot between the raw signal widths obtained in the reference scintillators after offset subtraction (color on-line). Six blobs can be identified being the most prominent ones attributable to protons, He and C^{12}. The other 3 blobs with a much lower yield must be Li, Be and B or charge states of the C^{12} ion.

reaction at an average energy $E_K = 1.76$ GeV (that accounts for energy losses in the Be target itself). As a consequence of Fermi motion, protons had still a sizeable angular straggling that rendered a much more uniform irradiation than for the C^{12} beam (Fig. 6.6-right).

In this setup, auxiliary mono-crystalline diamonds were placed 14 m upstream the scintillator reference system. From the time spread between the diamond detector and the first scintillator, $\sigma_{T(D-S_o)} = 248$ ps, and the simultaneously measured scintillator and diamond resolutions ($\sigma_{T(D)} = 150$ ps, $\sigma_{T(S_o)} = \sigma_{T(S_1)} = 40$ ps) the energy spread of the proton beam after

propagation over $D = 14$ m could be determined as:

$$\frac{\sigma_{E_K}}{E_K} = \frac{m_p}{E_K} \frac{\beta^2}{^{3/2}\sqrt{1-\beta^2}} \frac{\sigma_{tof}}{\text{tof}} \tag{6.10}$$

being

$$\text{tof} = \frac{D}{\beta c} \tag{6.11}$$

$$\sigma_{tof} = \sqrt{\sigma^2_{T(D-S_o)} - \sigma^2_{T(D)} - \sigma^2_{T(S_o)}} \tag{6.12}$$

resulting in a value for $\frac{\sigma_{E_K}}{E_K} = 4\%$. The energy losses due to the presence of 14 m of air are much below 4% for protons at this energy, supporting that the energy straggling is indeed originated in the production at the Be target.

The accelerator was also operated in slow extraction mode but at a reduced extraction time (1.5 seconds), resulting in a slightly asymmetric spill time-profile (Fig. 6.5-right). Two tRPCs (R_o, R_1) were powered up and measurements were taken as a function of the particle flux in the range 10-1000 Hz/cm^2 at voltages from 5.0-5.8 kV.

6.2.5.3 Cosmic rays

Once the measurements of the previous two sections were performed, a 'reference setup' with a cosmic stand where the scintillators and tRPC cells were assembled according to the previous section but horizontal with respect to the ground was built up, and data was taken. From the 2 meters of concrete that cover the HADES experimental area it can be estimated that the main source of particles traversing the 4 detectors are mainly muons at an average energy $\bar{E}_K = 3$ GeV ($\simeq$ 1GeV energy loss) [88]. The position profile obtained from scintillator S_o as shown in Fig. 6.6-right is fairly uniform but a bit broader than for proton irradiation, due to the larger angular straggling (since S_1 is a bit smaller than S_o and is also in trigger, for perpendicular incidence the measured S_o length is very close to the S_1 one and therefore $\simeq 2$ cm smaller than its true length). The HV was varied in the range 5.6-6.0 kV.

6.3 Results

6.3.1 Performance of the reference system

The use of LED discriminators for the reference scintillators requires of time-charge slewing corrections in order to obtain the best timing. The correlation of the time-of-flight between S_o and S_1 ($\Delta t_{S_o-S_1}$) with the average signal width is shown in Fig. 6.8, being:

$$\Delta t_{S_o-S_1} = \left.\frac{t_L+t_R}{2}\right|_{S_o} - \left.\frac{t_L+t_R}{2}\right|_{S_1} \tag{6.13}$$

The different species from Z=1-6 could be cleanly separated as shown in Fig. 6.7 and a time-width correction was performed individually for each specie on the basis of multi-linear segments. After this procedure, a combined time resolution of $\simeq 55$ ps was obtained for $\Delta t_{S_o-S_1}$ that, assuming both detectors to perform equally, yielded per counter $\sigma_T = 40$ ps for C^{12}, $\sigma_T = 39$ ps and $\sigma_T = 42$ ps for secondary He and p. The final time-of-flight distributions after corrections are shown in Fig. 6.8 for different particle species, showing a strong Gaussian behavior with $\sigma_T \simeq 40$ ps per counter, while the position resolution obtained from the position difference between the counters was $\sigma_y = 6$ mm. No dependence with the particle specie was observed. Being the values for σ_T consistent with the electronic resolution of the mean-time obtained with pulsed signals [56] and not depending on the primary ionization, provides a strong evidence that the performance of the reference system was indeed limited by the TDC resolution.

6.3.2 tRPC performance

The track selection was based on graphical cuts on the 2-dimensional signal width distribution in the scintillators (Fig. 6.7) for selecting the particle species corresponding to Z=1-6. Due to the energy regime, either secondary forward protons from C^{12} up-stream reactions or primary ones with $E_K \simeq 1.76$ GeV can be highly regarded as mips ($\gamma\beta \simeq 2.7$), the latter having additionally very little energy spread. On the other hand, an estimate of the energy loss from the

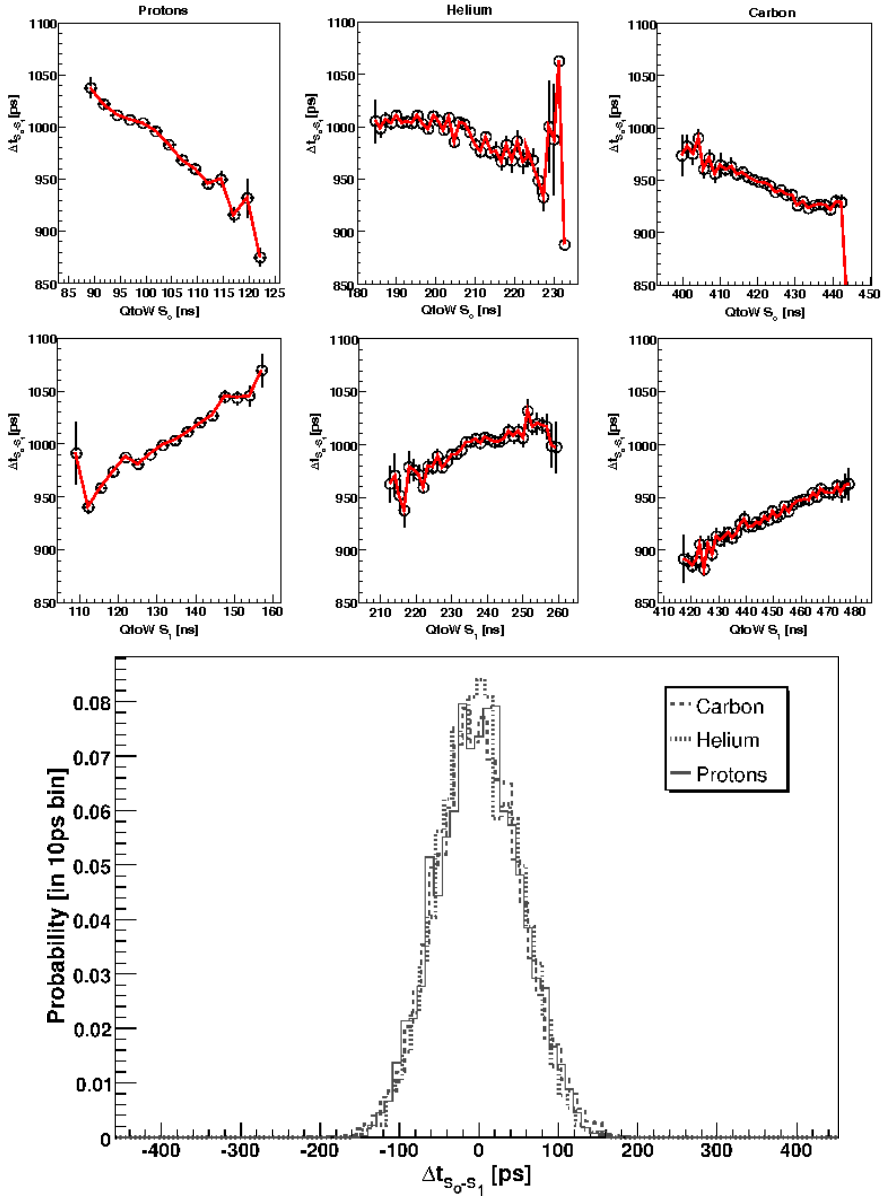

Figure 6.8: Up: multi-linear fit used for correcting the walk of the time of flight between the reference scintillators ($\Delta t_{S_o-S_1}$) as a function of the signal width ($QtoW$) for p, He and C^{12}. Down: distribution of times of flight between scintillators after the correction procedure for the three species.

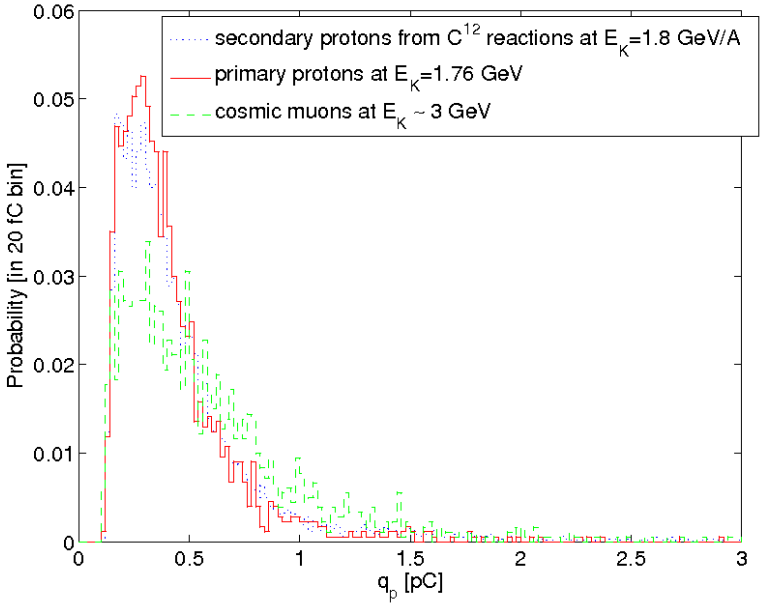

Figure 6.9: Comparison of the charge distribution measured in the tRPC under a diffuse proton beam at a kinetic energy $E_K = 1.76$ GeV $\pm 4\%$ (continuous line), secondary forward protons from C^{12} interactions at $E_K \sim 1.8$ GeV (dotted) and cosmic muons at $E_K \sim 3$ GeV (dashed).

Bethe-Bloch formula (eq. 6.18) indicates that cosmic muons with $E_K \simeq 3$ GeV ($\gamma\beta \simeq 30$) can ionize 30% more in the tRPC gas than mips. A normalized charge distribution after cuts is shown in Fig. 6.9 where indeed a very small difference is seen between the 3 different cases, being the average charge released by cosmic muons a bit higher than that for mips.

After particle identification, the last 1 cm from the border of the scintillators was disregarded. Furthermore, a 'co-linearity' cut of ± 2-σ in the distribution of the position differences between scintillators ($y_{s_o} - y_{s_1}$) was applied for improving the track quality selection. In order to reduce the effect of the non-uniform irradiation, C^{12} ions were additionally selected by a cut at $y > 2$ cm and other species by $y < 0$ cm. After these cuts for enhancing the purity and quality of the reference tracks, the time of flight between the two overlapping tRPCs ($\Delta t_{R_o - R_1}$)

was defined:

$$\Delta t_{R_o-R_1} = \left.\frac{t_L+t_R}{2}\right|_{R_o} - \left.\frac{t_L+t_R}{2}\right|_{R_1} \tag{6.14}$$

and the time resolution per counter was obtained as $\sigma_T = \sigma_{\Delta t_{R_o-R_1}}/\sqrt{2}$. Correction curves with respect to the charge of both tRPCs (slewing correction) and the position as given by the scintillators were performed. This is discussed in detail in section 6.5.2. A typical time-of-flight distribution for protons at an uniform flux of 150 Hz/cm^2 is shown in Fig. 6.10, yielding $\sigma_T = 87$ ps per tRPC. The usual recursive fit around ± 1.5-σ was applied to reduce the influence of tails in the fit [26], but for this set of measurements the value of σ_T changed little indeed if a direct fit was performed.

In the C^{12} experiment, due to the absence of the tRPC cell R_o, the time difference with respect to scintillator S_o was calculated in a similar manner:

$$\Delta t_{R_1-S_o} = \left.\frac{t_L+t_R}{2}\right|_{R_1} - \left.\frac{t_L+t_R}{2}\right|_{S_o} \tag{6.15}$$

and the tRPC resolution obtained after subtracting the contribution of the reference system:

$$\sigma_T = \sqrt{\sigma^2_{\Delta t_{R_1-S_o}} - \sigma^2_{\Delta t_{S_o-S_1}}/2} \tag{6.16}$$

6.3.2.1 Charge distribution

Normalized charge distributions are shown in Fig. 6.11 for $Z = 1$-6 at $V = 5.6$ kV at low rates ($\phi < 10$ Hz/cm^2). A phenomenological fit to 4-parameter Landau-like distributions

$$\mathscr{P} = a\exp(-bq_p - ce^{-dq_p}) \tag{6.17}$$

provides a good description and partially captures the high charge tails. Fig. 6.11 shows that there is indeed a strong correlation between the charge initially released and the final avalanche charge, but clearly not proportional, as one would expect if Space-Charge would be strong. Nevertheless, specific experimental situations where protons must be separated from Carbon, for instance, can be certainly addressed with these counters. These issues are

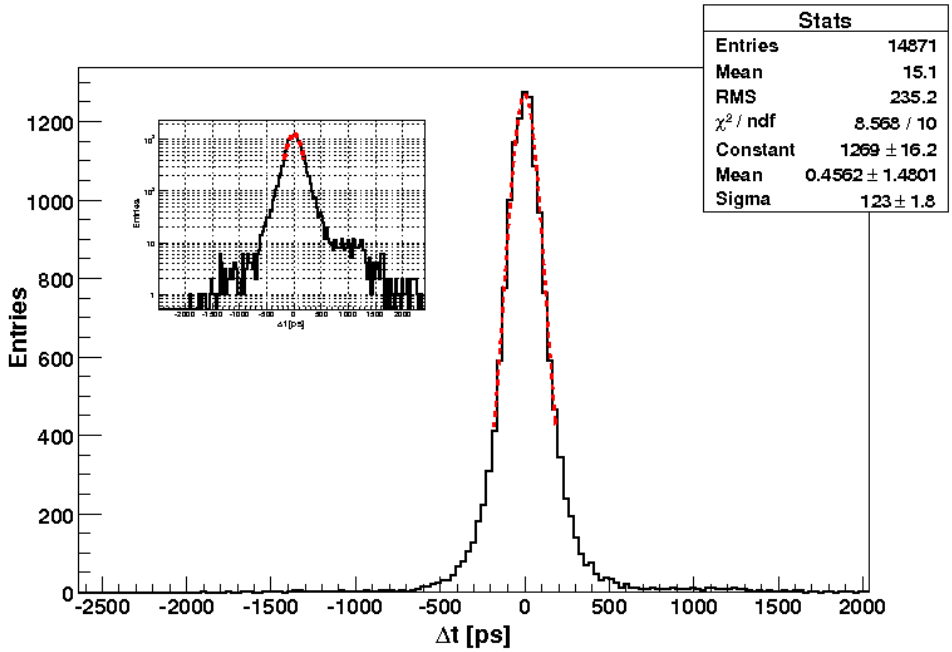

Figure 6.10: Time of flight distribution between tRPCs for a diffuse proton beam (kinetic energy $E_K = 1.76$ GeV $\pm 4\%$) at 150 Hz/cm^2 and V=5.6 kV. The inset shows the same distribution in logarithmic scale, indicating the presence of tails at 1% level. The counter resolution from the fit is $\sigma_T = 123/\sqrt{2} = 87$ps.

further discussed in section 6.4. Remarkably, it seems not to exist a clear separation between avalanches and streamers at high initial ionizations (contrary to the case when increasing HV, see Fig. 6.3). This fact cannot be firmly attributed to the tRPC dynamics since our charge calibration is sensitive to the signal shape and is therefore different for streamers, as pointed out in section 6.2.3. As a consecuence, the region $q_p > 5$ pC can be probably not assessed precisely here.

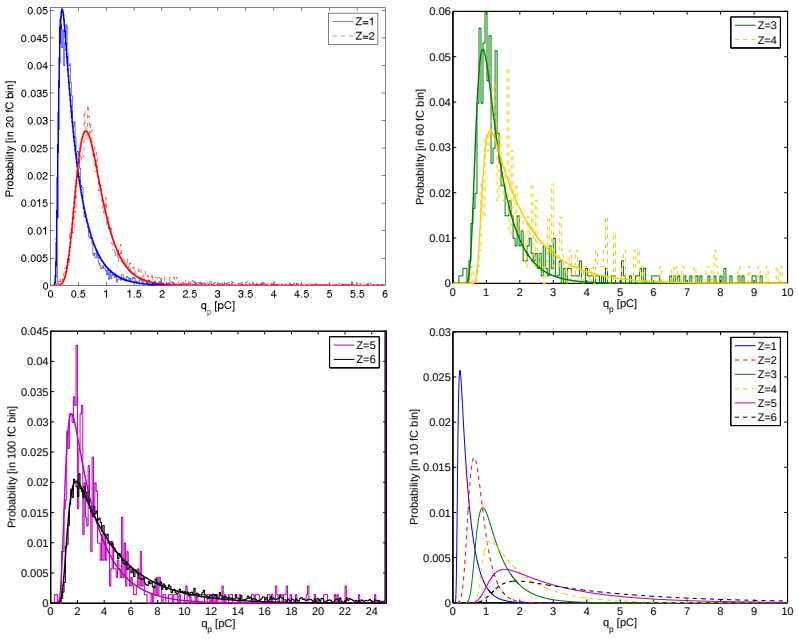

Figure 6.11: Up-left: tRPC charge distributions for fully stripped ions with atomic charges $Z = 1,2$ together with a fit to a Landau-like function. Up-right: $Z = 3,4$. Down-left: $Z = 5,6$. Down-right: Fitted curves for $Z =$ 1-6. The normalized momenta is $\gamma\beta \simeq 2.7$ in all cases, V=5.6 kV and $\phi < 10$ Hz/cm^2.

6.3.2.2 Dependence with HV

A scan in HV was performed for $E_K = 1.76$ GeV diffuse protons and cosmic muon irradiation. A particle flux of 150 Hz/cm^2 was chosen for the former while a much lower one was observed for the latter. The behavior of the time resolution and efficiency is shown in Fig. 6.12. Closed an open circles represent the efficiency when at least one or when both detector ends collect a valid signal, respectively, showing little difference.

As compared with [30] the behavior is slightly (but consistently) worst. While the resolution at the plateau is $\sigma_T \simeq 90$ ps both for protons (diamonds) and cosmic muons (triangles), and the efficiency $\varepsilon = 92\%$ (squares) and $\varepsilon = 96\%$ (circles) correspondingly, the

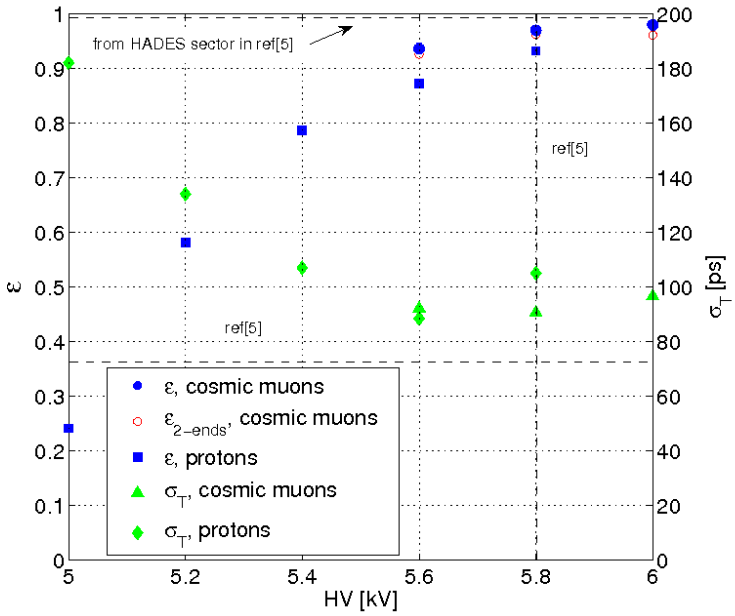

Figure 6.12: Efficiency for cosmic muons as a function of High Voltage when requiring a valid hit in at least one detector end (full circles) or in both (open circles), together with the efficiency for $E_K = 1.76 \pm 4\%$ GeV protons (squares). Time resolution for cosmic muons (triangles) and $E_K = 1.76 \pm 4\%$ GeV protons (diamonds) is also shown with scale on the right axis. A comparison with the system values from [54, 30] (efficiency, resolution and working point) is indicated by dashed lines.

values reported for the in-beam test at section 5.4.3 were $\sigma_T = 73$ ps, $\varepsilon = 99\%$ (intrinsic) and $\varepsilon = 98\%$ (system). Nevertheless, in such a case, no particle identification was available and actually a fraction of the impinging particles is expected to be more ionizing than mips. This, together with the slight redundancy of the HADES system ($\simeq 30\%$ cell overlap) may explain the slightly worse efficiencies observed here for mips. The worse resolution may be attributed to the grounding scheme and overall noise, routing and signal feed-through (unproperly matched) as compared with [30]. The multi-peak structure observed in the time response for the lowest voltage run ($V = 5.0$ kV, ε=24%) suggests that the noise level was abnormally

high, eventually influencing the response when the signals were very close to the threshold. This effect disappears at the nominal voltages $V = 5.6 - 6.0$ kV but a residual contribution to the overall resolution can certainly not be excluded.

The chambers showed dark rates of 0.05 Hz/cm^2 ($V = 5.6$ kV) and 0.15 Hz/cm^2 ($V = 6.0$ kV). Few minutes were needed after applying the HV before such values were reached, exceeding those by a factor 10-20 otherwise. Dark current was generally at the level of 1 nA or below.

6.3.2.3 Dependence with particle rate

The rate capability of 4-gap tRPCs with metallic electrodes and 2 mm glass plates has been studied under mip irradiation before [27], yielding a 5% efficiency drop ($-\Delta\varepsilon$) at 350 Hz/cm^2 and slight deterioration of timing performances. Another study in [67],[78] consistently showed that a moderate 10 °C temperature increase allows to keep the time resolution up to 1 kHz/cm^2 at least. Here is presented once again the behavior of the time resolution and efficiency as a function of the particle flux in Fig. 6.13 for a typical field $E = 100$ kV/cm, together with the fit from previous work [27] (dashed lines) and added the behavior under C^{12} ions. In this last case the non-uniform irradiation is taken into account from the measured position profile (Fig. 6.6) through an average over ± 1 cm around the peak value. For the proton case the study was performed with a diffuse beam (section 6.2.5.2).

Indeed the behavior for protons as seen in Fig. 6.13 is similar to the one reported in [27] but with a slightly worst resolution at low rates. Clearly, the efficiency for C^{12} is unaffected even at 600 Hz/cm^2 since the effective field drop is overcompensated by the largest initial charge (see Fig. 6.11). In this particular situation the resolution is expected to be more sensitive to the effective field (eq. 6.2) through $t_{rise}(\bar{E})$ and so a deterioration of the rate capability for C^{12} by a factor $\times 5$ with respect to protons can be inferred from the figure (if the flux at $\sigma_T = 100$ ps is compared, for instance). Note that from eq. 6.8 one expects (at moderate rates, when $\bar{q}_T$

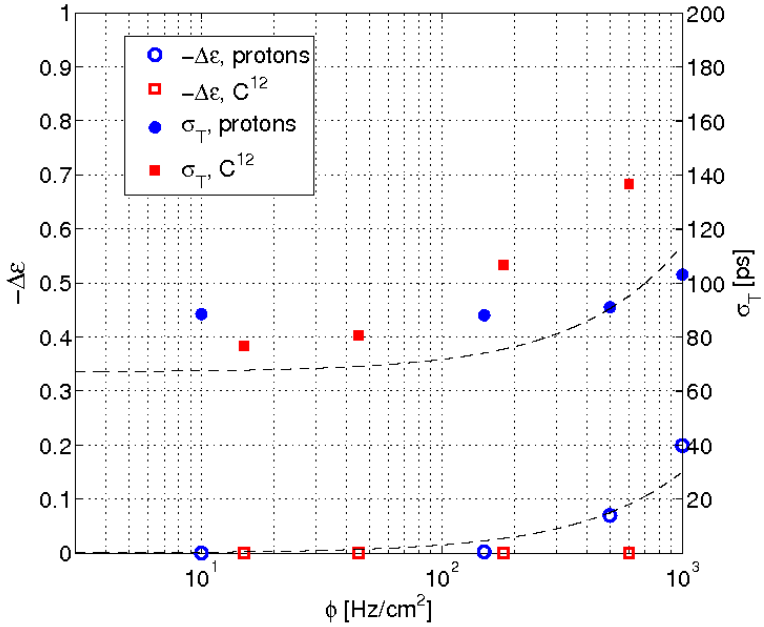

Figure 6.13: Time resolution σ_T and decrease in efficiency $-\Delta\varepsilon$ in the tRPCs for protons at $E_K = 1.76 \pm 4\%$ GeV (circles) and fully stripped Carbon ions at $E_K = 1.8$ GeV/A (squares) as a function of their flux. The operating voltage was V = 5.6 kV.

changes little) this factor to be directly the ratio of the total avalanche charges $\bar{q}_{T,C^{12}}/\bar{q}_{T,p}$. If the tRPCs would work in the proportional regime this ratio would be $Z^2 = 36$.

A remarkable fact is that for multi-gap tRPCs under mip irradiation both ε and σ_T begin to deteriorate at a similar value of the flux while for higher initial ionizations the former can be kept at reasonable values even at high particle fluxes and mainly σ_T is affected.

Fig. 6.13 shows that the detection of relativistic ions up to $Z = 6$ is feasible with 4-gap tRPCs operated at typical fields ($E = 100$ kV/cm), with a resolution $\sigma_T \simeq 80$ps, and $\varepsilon \simeq 100\%$. A more detailed differential study as a function of the energy loss is presented in the next section.

6.4 Dependence with particle type

6.4.1 Introduction

At fixed momentum per nucleon ($\gamma\beta$ constant), heavy charged particles lose energy due to electromagnetic interactions in square proportion to its electric charge according to the Bethe-Bloch formula:

$$\frac{dE}{dx} = K\left(\frac{Z_m}{A_m}\right)Z^2\frac{1}{\beta^2}\left[\frac{1}{2}\ln\frac{2m_e c^2\beta^2\gamma^2 T_{max}}{I^2} - \beta^2\right] \tag{6.18}$$

where Z_m, A_m are the atomic and mass number of the medium, m_e is the electron mass, I the mean excitation energy, and $K = 0.307075$ MeVg^{-1}cm^2. A prescription for calculating Z_m/A_m and I in mixtures according to [88, 89] will be used in the following.

Using fully stripped ions of charge Z is a practical alternative to study the energy loss dependence of a counter over a very broad dynamic range. Moreover, as long as measurements are performed in the forward beam direction any low-Z fragment is likely to proceed from spallation reactions, roughly keeping its energy per nucleon (E_K/A) and so β. Therefore in the present experimental situation, having a primary C^{12} beam with $Z = 6$, it is reasonable to assume that ions with Z=1-6 will have a primary ionization in a relative proportion close to 1, 4, 9, 16, 25, 36. Additionally, for the energies $E_K/A = 1.8$ GeV used here, even in the very unlikely case that a secondary proton (for instance) would travel forward with a kinetic energy as low as $E_{K,p} = 1/4(E_K/A)$, it would release only 20% more energy than mips according to eq. 6.18. The above considerations are true only for electromagnetic interactions with hadronic interactions expected to happen only residually. In this setup, there was no way to separate contributions from hadronic interactions, but with another reference detector placed RPC downstream, one could separate those by vetoing on it. The effect of hadronic interactions is disregarded for the latter discussion and so, being $\gamma\beta \simeq 2.7$ it will be useful to re-express the Z-dependence as $\Delta E/\Delta E_{mips} = Z^2$.

6.4.2 Charge distribution

To the author knowledge, there is only one published work on the energy loss dependence of multi-gap tRPCs [75], whose conclusions yet remain disputed, specially regarding the very high shifts observed for the average time of flight $\bar{t}$ as compared with the expected one [76]. The situation was revisited starting from the dependence of the average prompt charge $\bar{q}_p$ with the energy loss. For that it was taken the average charge for protons as a function of the momentum p from Fig. 8 in ref. [75] and pad-ring 3 that corresponds to perpendicular incidence, according to the authors. The Bethe-Bloch formula for the HARP gas mixture was evaluated from eq. 6.18 and used for re-calculating $\Delta E/\Delta x$, re-normalizing its value to the value for mips. Since the average prompt charge is referred in arbitrary units in [75] it was arbitrarily re-scaled to provide the best agreement with the data presented here. Note that the geometry of the HARP cells is very close to the HADES one, having also 4 gaps and a very similar gap spacing ($g = 0.3$mm and $g = 0.28$mm, respectively). Values for HARP are shown in Fig. 6.14-left (squares).

When increasing the energy loss the probability of streamers also increases [21]. The above fact makes the interpretation of the charge spectra difficult since a theoretical description of streamers in tRPCs is not yet available. In order to simplify this task, fits to Landau-like functions of Fig. 6.11 were used to extract the charge at maximum $q_p(\max)$ whose energy loss dependence is expectedly dominated by the avalanche dynamics and little dependent on the streamer mechanism. The values for $q_p(\max)$ together with the direct charge average $\bar{q}_p$ are shown in Fig. 6.14-left. The trends of $q_p(\max)$ and $\bar{q}_p$ are indeed similar up to $\Delta E/\Delta E_{mips} = 4$ but diverge afterwards, pointing to the influence of streamers for $\Delta E/\Delta E_{mips} > 4$. Note the reasonable good agreement in the trend of $\bar{q}_p$ when comparing with the HARP data. The following phenomenological curves could be found:

$$q_p(\max) \propto \sqrt{\frac{\Delta E}{\Delta E_{mips}}} \tag{6.19}$$

$$\bar{q}_p = \bar{q}_p(1) + 0.2\left(\frac{\Delta E}{\Delta E_{mips}}\right) \tag{6.20}$$

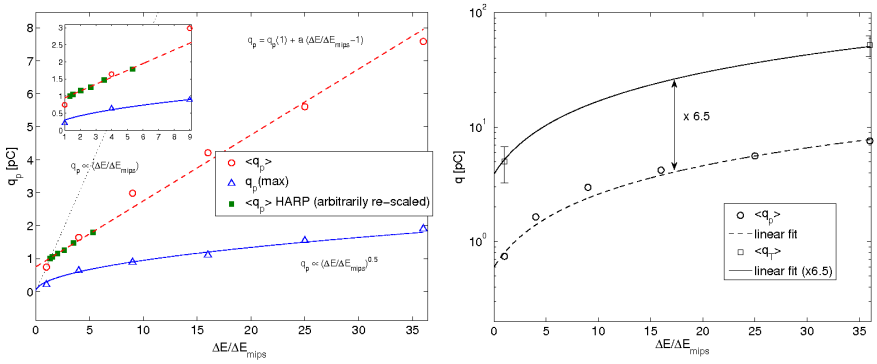

(a) (b)

Figure 6.14: (a) Average prompt charge $\bar{q}_p$ (circles) and charge at maximum $q_p(\max)$ (triangles) from the tRPC as a function of the energy loss expressed in mips units. Data from HARP is shown by squares for comparison. Different trend curves are indicated. (b) Average prompt $\bar{q}_p$ and total $\bar{q}_T$ charge (circles, squares) as a function of the energy loss expressed in mip units. A linear fit is shown (dashed line) together with the same curve re-scaled by a factor 6.5 to meet the $\bar{q}_T$ data.

As a result of Space-Charge, neither $q_p(\max)$ nor $\bar{q}_p$ show a proportional behavior with the primary ionization.

Since the total current and particle rates were continuously monitored (Fig. 6.5) the total average charge $\bar{q}_T$ could be determined to be $\bar{q}_T = 5 \pm 1$ pC under proton irradiation and $\bar{q}_T = 53 \pm 10$ pC for C^{12} under C^{12} irradiation. The latter calculation requires to re-estimate the proportion of C^{12} ions in the measured rate, and is done from Fig. 6.6, yielding 3/5 of the total. The contribution of He and proton ions to the measured current is neglected. Note that if one assumes the same scaling with the energy loss for $\bar{q}_T$ than for $\bar{q}_p$ the He and p rates (2/3 of the total) contribute to the measured current in less than 10%. From run to run variations it was estimated in 20% the error in $\bar{q}_T$ for protons and the same uncertainty was taken for the C^{12} value. Data for $\bar{q}_p$ and $\bar{q}_T$ is shown as a function of $\Delta E/\Delta E_{mips}$ in Fig. 6.14-right together with a linear fit to the $\bar{q}_p$ data. The same function can describe the trend of the $\bar{q}_T$ points after multiplying by a factor $\times 6.5$. If a model of the kind of [40] would be

used for describing avalanche multiplication under strong Space-Charge, the ratio $\bar{q}_T/\bar{q}_p$ is indeed expected to depend on the initial energy loss, because the higher the initial charge the earlier the avalanche enters in the Space-Charge regime and the more the released electrons drift before arriving to the anode, resulting in a higher electron-induced charge for the same avalanche charge. Because of that, and because of the different behavior of $\bar{q}_p$ and $q_p(\max)$ with $\Delta E/\Delta E_{mips}$, the scaling observed in Fig. 6.14-right could be strongly affected by the presence of the streamers.

6.4.3 Time distribution

A striking observation in [42] was the existence of very strong drifts of the average time-of-flight as a function of the energy loss. The much larger range of ionizations present here allows to discuss this point in high detail. First, in Fig. 6.15-left the time resolution after slewing correction is shown for the different species at $V = 5.6$ kV. The analytical scaling from eq. 6.2 is illustrated by fixing $\sigma_T(1)$ to be 80 ps. Unfortunately, the scaling of σ_T is not visible in data, pointing to the fact that a limitation to the resolution different from avalanche dynamics is present in the measurements. In connection with this observation it must be recalled that despite the solid derivation of eq. 6.2 there is no systematic experimental study so far on the behavior of σ_T with the energy loss. Proving (or disproving) the scaling of eq. 6.2 by systematic measurements would be extremely important in order to better understand the practical limitations of these counters for timing. An experimental confirmation of this scaling would allow to understand why, in practice, the difference between 1-gap counters and multi-gap can be as little as $\sigma_T = 55$ ps (1 gap, [60]) and $\sigma_T = 40$ ps (10 gaps, [43]), when operated in very similar conditions of gas mixture and field. No data from the HARP collaboration is available on this important aspect. Since our system is limited to a resolution of $\sigma_T = 40$ ps for the mean-time (Fig. 6.8) a much more accurate FEE+TDC chain would be needed, nevertheless, in order to evaluate the theoretical prediction for C^{12} ions.

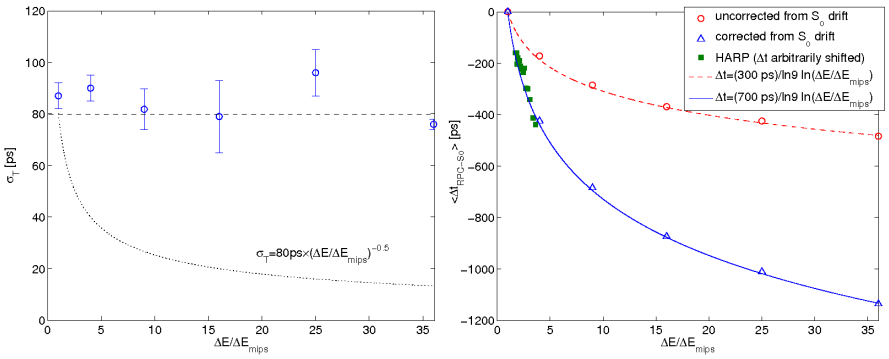

(a) (b)

Figure 6.15: (a) Time resolution σ_T as a function of the energy loss expressed in mips units together with the approximate $1/\sqrt{\Delta E}$ scaling. (b) Average time of flight between tRPC and scintillator S_o as a function of the energy loss expressed in mips units together with the approximate $\ln(1/\Delta E)$ scaling before (circles) and after (triangles) correcting for the scintillator drift. HARP data is shown as full squares. Two theoretical curves are fitted in each case with a single parameter $t_{rise} = 300$ ps (dashed line) and $t_{rise} = 700$ ps (continuous line).

Fig. 6.15-right shows the average behavior of $<\Delta t_{RPC-S_o}>$ (eq. 6.15) before corrections and referred to the case of mips (circles), together with the analytical scalings from eq. 6.1 assuming $t_{rise} = 300$ ps (dashed line). Despite the reasonable value obtained for t_{rise} this is indeed the minimum value consistent with the observations: if a sizeable drift is present in the reference scintillators part of the drift originated in the tRPC would be effectively shadowed after taking the difference. In the absence of constant fraction discriminators the best practical approach to estimate this effect in the scintillators is by looking at the $\Delta t_{S_o-S_1}$ distributions when the particle releases charges corresponding to Z=1-6 in S_o and keeping a narrow cut around Z=1 in S_1. The above value can be used to correct $<\Delta t_{RPC-S_o}>$ from the scintillator drifts and provide an estimate of the time drift caused by the tRPC alone (triangles). The latest HARP data from [76] are also overlaid (squares) after an arbitrary shift. According to the authors the values have been obtained after a re-analysis based on a direct determination of the momentum p by physical constraints (elastic scattering) and are expected to be free from

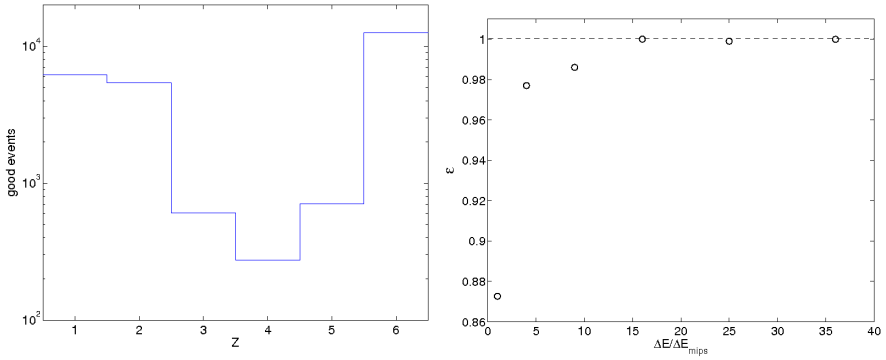

(a) (b)

Figure 6.16: (a) Population of ions with charge states $1-6$ after cuts ('good events'). (b) Detection efficiency as a function of the energy loss expressed in mips units. The points have being obtained for $V = 5.6$ kV at low particle rates ($\phi < 10$ Hz/cm^2).

artificial drifts that previously arose from an incorrect momentum reconstruction. In order to compare with present data the energy loss was re-calculated from eq. 6.18, as in previous subsection. Several things can be noted: i) despite the different FEE band-widths the corrected values for Δt_{RPC-S_o} agree with latest HARP data and can be described with a logarithmic dependence if $t_{rise} = 700$ ps; ii) surprisingly, the authors in [76] implicitly assumed a value for $t_{rise} = 100$ ps for the discussion in the paper, presumably inspired by theoretical values for $(\alpha - \eta)v_e$, despite this seems to be largely inconsistent with their own measurements; iii) the previously reported '500 ps' effect from [75] can also not be confirmed by the present measurements; iv) a lower limit for $t_{rise} > 300$ ps readily arises from the present data.

For the sake of completeness, fig. 6.16-right shows the detector efficiency as a function of the energy loss. The fact that for $Z > 1$ the efficiency is almost 100% indicates that the trigger geometry is reasonable, being the lower values for $Z = 1$ partly attributable to the slightly low operating voltage (Fig. 6.12). Fig. 6.16-left presents the specie population after cuts.

6.5 Discussion

6.5.1 Element identification

When aiming at ion identification a time of flight measurement provides the ratio $\gamma\beta = p/A$ while momentum (p) and element (Z) identification must be done by independent means [70]. So it is interesting to see at which extent a multi-gap tRPC has resolving power in Z by using the q_p information. In order to evaluate this, the purity P against ion Z_2 for a 90% identification efficiency of ion Z_1 is defined by:

$$P_{90} = \left(\frac{N_{Z_1} - N_{Z_2}}{N_{Z_1}} \right)_{\varepsilon_{Z_1}=90\%} \tag{6.21}$$

where the condition $\varepsilon_{Z_1} = 90\%$ imposes a fixed cut in the prompt charge. Taking all the populations from the normalized distributions of Fig. 6.11 the suppression factor Π_{90} for specie Z_2 when aiming at detecting Z_1 with 90% efficiency can be defined as:

$$\Pi_{90} = \left(\frac{N_{Z_1}}{N_{Z_2}} \right)_{\varepsilon_{Z_1}=90\%} = \frac{1}{1 - P_{90}} \tag{6.22}$$

Π_{90} is shown in Fig. 6.17 for the different ions.

The overall suppression is modest, but a strong suppression already exists for $Z = 4$ ions when aiming at proton detection ($\sim \times 65$). Contrary, the suppression of alpha particles for proton detection as well as that of $Z = 6$ ions for $Z = 4$ ion detection is only slightly higher than 1.

6.5.2 Time-Charge correlation

Slewing correction is the procedure after which the time of flight walk as a function of the signal amplitude is corrected for. The nature of this correlation is not yet clear, but it seems to be dominated by the electronic response at low charges [71]. Indeed very little correlation, if any, remains in the present case for $Z = 6$, where the signals are largely above threshold (Fig. 6.18-up), unlike protons. Moreover, the measured time for high charges is systematically shifted by roughly 400 ps when comparing protons and Carbon, as already discussed in

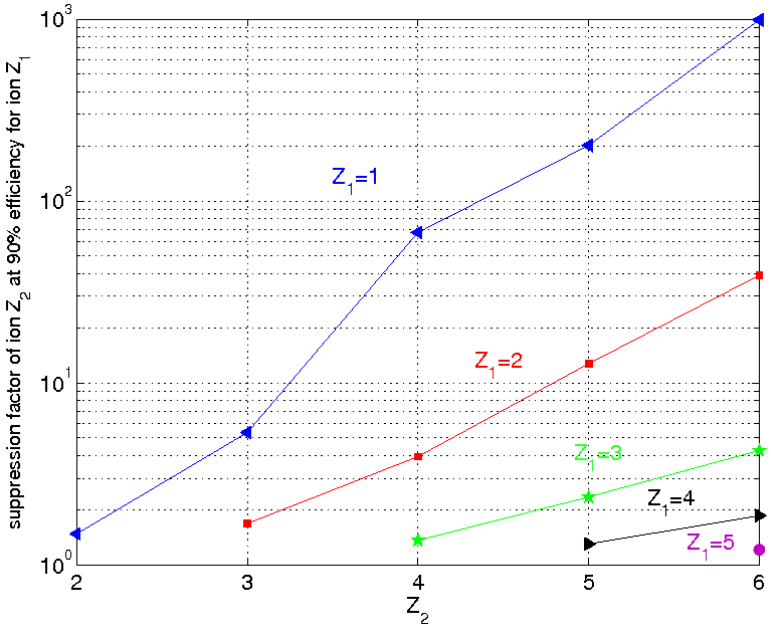

Figure 6.17: Suppression factor of element in charge state Z_2 when imposing a cut in the RPC charge for a 90% identification efficiency of element in charge state Z_1. The suppression factor has been obtained after fitting the charge distributions to Landau-like functions.

connection with Fig. 6.15. In this particular case the external detectors provide a clean separation in Z so that the time distributions corresponding to the different ions can be identified and the drift of the average time becomes a trivial systematic effect. Now, if Z is not known (or, generally, if $\Delta E/\Delta E_{mips}$ is not known), this systematic dependence of the average time can not be fully corrected for and these variations enter effectively in the measured response function.

The worsening of the time resolution due to variations in the average time due to different primary ionizations is known since time ago [36] but has only been applied to account for the Poisson fluctuations in the initial number of clusters. Following the spirit of this work, a simple although more experimentally-driven approach is devised here to estimate this effect

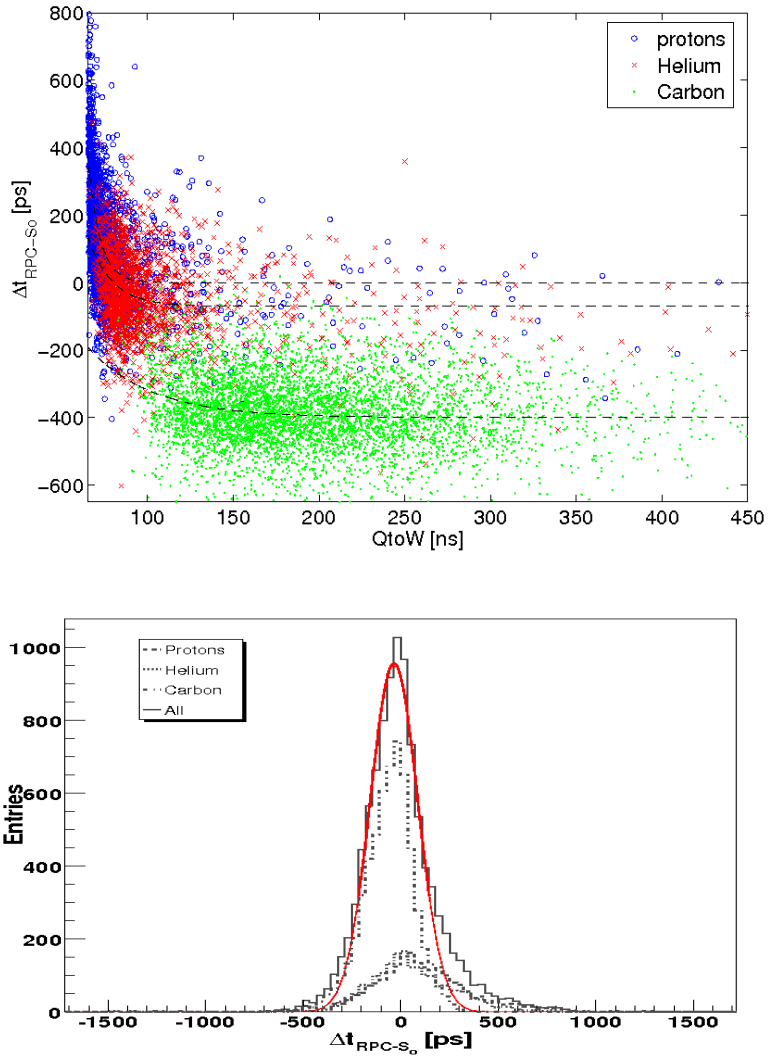

Figure 6.18: Up: Scatter plot showing the walk of the time-of-flight between RPC and scintillator S_o as a function of the signal width ($QtoW$) for protons, Helium and Carbon. Tendency curves are shown in each case. Down: time-of-flight distribution after applying an unique slewing correction for all species (ignoring external identification in Z). Identification is applied at the end of the procedure to evaluate the result in such conditions. A resolution $\sigma_T = 115$ ps is obtained for the combined fit, with increased tails towards delayed times as compared with the case where identification in Z is provided.

in practice. Let's assume first that the time resolution does not depend or depends little on the average ionization. This assumption is not supported by avalanche models, but would be the case if the measured resolution is not dominated by the detector response function but by an external source (FEE jitter, noise and/or TDC resolution). Such a case is practically relevant. Further, a flat distribution of possible energy losses over a range $\Delta E_{max} - \Delta E_{mips}$ is assumed. The rms of the resulting distribution can be estimated from the relations:

$$\bar{t}_{\Delta E} = \frac{1}{\Delta E_{max} - \Delta E_{mips}} \int_{\Delta E_{mips}}^{\Delta E_{max}} \frac{t_{rise}}{\ln 9} \frac{\Delta E_{mips}}{\Delta E} d\Delta E \tag{6.23}$$

$$\sigma_T^2 = \frac{1}{\Delta E_{max} - \Delta E_{mips}} \int_{\Delta E_{mips}}^{\Delta E_{max}} \left[\left(\frac{t_{rise}}{\ln 9} \frac{\Delta E_{mips}}{\Delta E} \right)^2 - \bar{t}_{\Delta E}^2 \right] d\Delta E \tag{6.24}$$

that yield:

$$\sigma_T(\Delta E_{max}) = \frac{t_{rise}}{\ln 9} \sqrt{1 - \frac{1}{(\frac{\Delta E_{max}}{\Delta E_{mips}} - 1)^2} \frac{\Delta E_{max}}{\Delta E_{mips}} \ln^2 \frac{\Delta E_{max}}{\Delta E_{mips}}} \tag{6.25}$$

Eq. 6.25 has the curious property of tending asymptotically to $t_{rise}/\ln 9$ for high energy deposition. Since the intrinsic detector resolution is expected to be of this order (eq. 6.2) in the limit of low ionization, one may conclude that energy spread cannot modify the detector resolution by a large factor.

Actually, two things can happen:

1. that the intrinsic detector resolution from eq. 6.2 is reached, and then from eq. 6.25 the worsening due to the energy loss will be of the same order than the resolution itself, being the latter partially compensated by the improvement in the intrinsic resolution for every value of ΔE (eq. 6.2) or

2. that it is not reached, and then the deterioration from eq. 6.25 will be smaller than the resolution itself, anyway. So it seems that the variations on the initial ionization are called to be 'second order' for the counter resolution.

The above considerations cannot account for all the possible ΔE distributions and must be taken with care when a highly Gaussian response is needed. Relevant cases where this effect should be taken into account are neutron or γ detection due to interaction in the electrodes, where a secondary particle with its corresponding energy distribution is released, and also ion detection. So, the usual assumption that a higher ionization renders a better time resolution can not be considered universally true for this kind of detectors, on the basis of the existing knowledge. A detailed discussion on this effect can be found in [77].

Another relevant situation would be the dependence of the average ionization with Z, assuming the energy per nucleon to be the same for all the particle species. Let's further assume that $2N+1$ species are present in the same amount, centered around specie $\bar{Z}$. If a detector providing identification in Z would not exist an extra jitter will appear in the form:

$$\bar{t}_{\bar{Z}} = -\frac{t_{rise}}{\ln 9}\left(\sum_{i=1}^{N}\frac{\ln(\bar{Z}+i)^2+\ln(\bar{Z}-i)^2}{2N+1}+\frac{\ln\bar{Z}^2}{2N+1}\right) \tag{6.26}$$

$$\sigma_T^2 = \left(\frac{t_{rise}}{\ln 9}\right)^2\sum_{i=1}^{N}\frac{\left(\ln(\bar{Z}+i)^2-\frac{\ln 9}{t_{rise}}\bar{t}_{\bar{Z}}\right)^2+\left(\ln(\bar{Z}-i)^2-\frac{\ln 9}{t_{rise}}\bar{t}_{\bar{Z}}\right)^2}{2N} \tag{6.27}$$

in the limit where $\bar{Z}$ and N are big, but still $\bar{Z} \gg N$, eq. 6.27 yields:

$$\sigma_T(N,\bar{Z}) = \sqrt{\frac{8}{6}}\frac{t_{rise}}{\ln 9}\frac{N}{\bar{Z}} \tag{6.28}$$

so the practical influence of the uncertainty in Z in the measured resolution is also little for high $\bar{Z}$ values. However, for cases where $\bar{Z} \simeq N \simeq 1$ (the present case) the jitter arising from a bad identification in Z will be as high as 500 ps, as illustrated in Fig. 6.18. As a benefit, the Z-resolving power of the tRPC itself will be also much higher, resulting in a time-charge correlation curve different from the usual one for mips (compare circles in Fig. 6.18 with all the three species together). In particular, if only Carbon and protons would be present in the sample they can be very easily identified and corrected for, and only few events (Carbon with $QtoW < 100$ ns and protons with $QtoW > 100$ ns) would be wrongly identified. If one would

have ignored for a while, in this particular experimental conditions, the existence of secondary particles arising from the primary C beam, and would have used a single correlation curve the net result would have been a deterioration of the estimated time resolution for C ions from $\sigma_T = 73$ ps to $\sigma_T = 115$ ps, with large tails towards delayed times.

6.5.3 Space-Charge

There is a simple analytical model that accounts for Space-Charge effects, and that is based on the avalanche equations in the presence of a charge-dependent Townsend coefficient [40]. This model is analytical for each avalanche and depends on its position and initial ionization, but the solution to the general problem can only be treated numerically. It is not the purpose of the present work to quantitatively describe Space-Charge, but do some clarifying attempt by evaluating formulas in [40] for three typical avalanche positions in the gap. Further, the simplifying assumption that all the charge is released at the position of the avalanche is done. The values $\alpha^* = 73$ mm^{-1}, n_o/gap$= 3\Delta E/\Delta E_{mips}$, $q_{sat} = 10^5$ (number of electrons for a 50% drop of α^*) were taken and leave the overall normalization as a free parameter to match the data. Finally, it was looked at three situations (Fig. 6.19): i) the avalanche is produced in the cathode ($x_o = 0$, dotted line), ii) in the center of the gap ($x_o = g/2$, dashed) and iii) 20μm separated from the anode (dot-dashed).

Clearly, one cannot conclude from the comparison shown in Fig. 6.19 by such a simplified model, but it can illustrate how Space-Charge works. For avalanches produced close to the cathode there is almost no sensitivity to the initial ionization, since its evolution is anyway doomed to a similar end once the critical value of q_{sat} is reached. For avalanches produced close to the anode, the resulting charge will be obviously rather small (an effect absorbed here in the overall normalization) but essentially proportional to the initial one, since the avalanche charge is then much smaller than q_{sat} and Space-Charge plays no role. For the center of the gap, an intermediate situation is reached, where the avalanche growth is modified but some

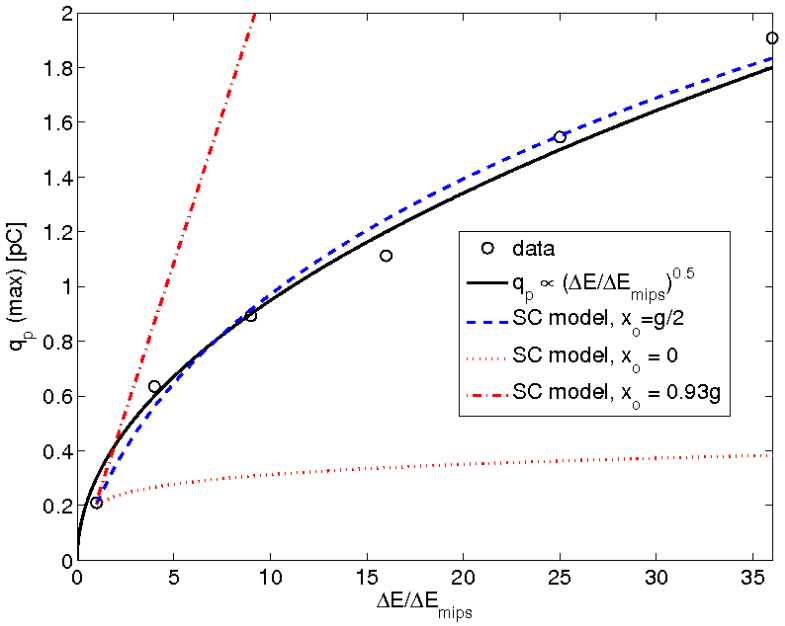

Figure 6.19: Measured charge at maximum $q_p(\max)$ as a function of the energy lost in mips units (circles). The $\sqrt{\Delta E}$ experimental scaling is shown together with the evaluation of the model of [40] under the assumptions of the text, for three different positions x_o of the avalanche inside the gap (center, close to the cathode and close to the anode).

sizeable correlation with the initial charge is still present. Remarkably, this latter situation matches well the trend of the experimental points.

6.5.4 Streamers

From the experimental point of view when aiming at ion detection it would be probably convenient to operate the detector in absence of streamers. It is possible to perform a semi-quantitative evaluation of what is the practical implication of this fact by using some classical arguments: if it is denoted by α_c^* the effective gain threshold at which streamers would arise, then following the approximate derivation of [38] it can be seen that this value will depend on

the initial ionization as:

$$\alpha_c^*|_Z = \alpha_c^*|_{mips} - \frac{\ln Z^2}{g} \tag{6.29}$$

so, the critical value of the Townsend coefficient for an ion with charge Z is naturally lower than that of mips, and the same will happen for the field at which streamers will appear in one case and the other. Now one can further assume a dependence of $\alpha^*(E) \simeq \frac{d\alpha}{dE}E - b$ (inspired by transport codes [71]) and obtain the necessary decrease in the field to operate the chamber in the absence of streamers that would simply be, for a given ion Z:

$$E[\text{kV/cm}] = \frac{dE}{d\alpha}\left[\alpha_c^*|_{mips} - 1/g \ln Z^2 + b\right] \tag{6.30}$$

If the natural assumption $\alpha_c^*|_{mips} \simeq \alpha^*(E_o = 100\ \text{kV/cm})$ is made, then:

$$E_Z[\text{kV/cm}] = E_o[\text{kV/cm}] - \frac{dE}{d\alpha}\left[\frac{\ln Z^2}{g}\right] \tag{6.31}$$

By directly substituting the simulated value for $\frac{dE}{d\alpha}$ [71] it can be expected that even for the most extreme case of Au detection ($Z = 79$) a mere decrease of a 10% in the field would be sufficient to operate the chamber in pure avalanche mode. The anticipated decrease of performances resulting from the lower field would be over-compensated if the scalings with Z illustrated through eqs. 6.2 and 6.3 hold:

$$\sigma_T(Z) \simeq \frac{K_1}{Z}\frac{t_{rise}}{\ln 9} \tag{6.32}$$

$$\varepsilon(Z) > 1 - \exp\left[-n_o\left(1 - \frac{\eta}{\alpha} - \frac{\ln(1 + \frac{(\alpha-\eta)}{E_w}n_{th})}{\alpha g}\right)Z^2\right] \tag{6.33}$$

since t_{rise} and α have approximate linear dependences with the field E.

6.6 Conclusions

A time resolution $\sigma_T \simeq 80$ ps at $\varepsilon \simeq 100\%$ has been consistently measured for relativistic ions with charge states Z=2-6 for the first time by just using standard 'off the shell' Multigap timing RPCs from the HADES wall.

The energy loss dependence of the avalanche charge and detector-related time-of-flight systematic shifts have been compared with previous data and extended over a much larger range of primary ionizations, showing a reasonable agreement. The measured time drifts cannot be accommodated in the existing theoretical framework unless a value for the signal rise-time 2.5 times bigger than current experimental estimates is assumed. The observed behavior of the prompt charge with the initial ionization seems to provide a stringent benchmark for the parameters of Space-Charge models and a simple comparison was attempted, showing a reasonable agreement.

Operation capabilities with Carbon fluxes up to 100 Hz/cm^2 was demonstrated with time resolution $\sigma_T < 100$ ps and $\varepsilon \simeq 100\%$ under an 8-second spill (50% duty cycle) and $\simeq 2 \times 2$ cm^2 irradiated area. Above 100 Hz/cm^2 the time resolution deteriorates rapidly but the efficiency was kept up to 600 Hz/cm^2 (at least) due to the much higher initial ionization as compared with mips. The behavior of the resolution as a function of the flux is similar to that of mips, when re-scaling the rate by a factor $\times 5$. This value is very similar to the measured ratio of the total charges $\bar{q}_{T,C^{12}} / \bar{q}_{T,p} = 6.5$, as expected from a simple DC modelling of the detector. Based on this observation, the measured trend of $\bar{q}_T(Z)$ can be extrapolated to high Z, yielding an approximate dependence for the rate capability as $\Phi_{max}(Z) = \frac{1\text{kHz}}{0.2Z^2}$, that would severely limit the operating rate to barely 1 Hz/cm^2 for Au ions. Based on the present measurements, it is likely that the very high initial charge will not affect the chamber stability in such situation but it will largely reduce its rate capability. In a realistic application, the working voltage should be chosen taking this fact into account.

The nature of the time-charge correlation and the practical timing limitations when the energy loss of the ionizing particle can not be addressed by external means have been discussed. It has been shown that under reasonable assumptions the detection of particles through secondary processes (in case of neutron or γ-photons, for instance) would yield an extra time jitter of the order of the detector intrinsic resolution for mips, therefore the good timing characteristics of these devices will be preserved even in such a situation. A practical example has being given based on the present data. Nevertheless, the intuition that higher ionization yields

better results does not seem to be a trivial statement for these counters and every physical case should be probably addressed experimentally.

Despite the large dynamic range explored here the chamber+electronics performed stably during the whole experiment, underlining the superior performance of float glass Multi-gap timing RPCs in highly ionizing environments when high rates are not required. Always depending on the Z of the species of interest, a Multi-gap configuration does not seem to be mandatory for ion detection. A more practical RPC design could be probably based on 1-gap RPCs (single or mirrored [90]).

Chapter 7

HADES tRPC Cosmic Test

During three different periods in 2009, all assembled and fully instrumented tRPC sectors were tested by pairs, at GSI, under cosmic rays radiation, prior to the final installation in the spectrometer. The most important results obtained in such test, as well as a description of the setup, are presented in this chapter. It is also published in [91].

All sectors were tested with the final Front-End Electronic (FEE) and Data Acquisition System (DAQ) together with Low Voltage (LV) and High Voltage (HV) systems. Results confirm a very uniform average system time resolution below 77 ps sigma together with an average multi-hit time resolution of 83 ps. Crosstalk levels below 1% (in average), moderate timing tails along with an average longitudinal position resolution of 8.4 mm sigma are also confirmed.

7.1 Setup

As already mentioned, the six final tRPC sectors described in Chapter 3 were evaluated under cosmic rays at GSI, Darmstadt, Germany, and subsequently validated for the final installation in the nominal position within the HADES Spectrometer.

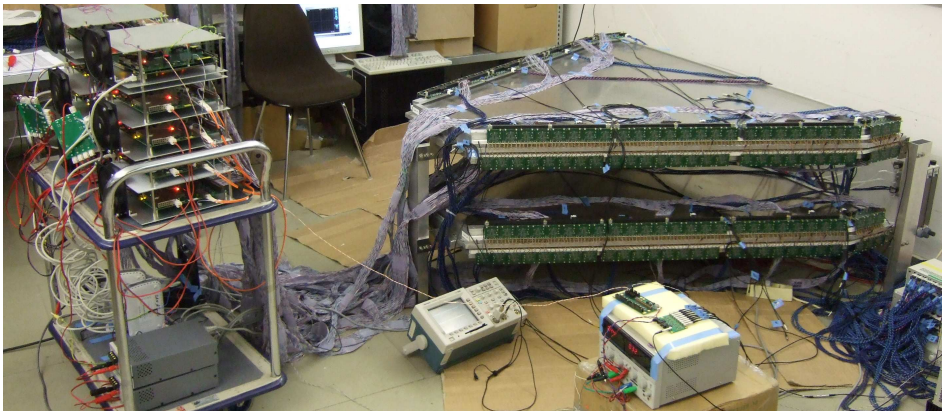

Figure 7.1: Setup for testing two sectors, including the Data Acquisition System (on the table) and the custom made Low Voltage power supply (bottom right).

Fig. 7.1 shows the setup used to evaluate the sectors performance. Basically, each pair of sectors was vertically stacked at a distance of around 350 mm. Data were taken (around 200 Mevent / sector, @ 150 Hz) when, at least, one cell fires (hit) in each sector, which eventually corresponds to the passage of a cosmic ray through the sectors.

The RPCs were operated with a gas mixture composed of 90% $C_2H_2F_4$ and 10% SF_6 under a continuous gas flow of 50 cc/min at a nominal High Voltage (HV) of 5600 V. All sectors, named as S_i with $i = 1...6$, were tested with the final subsystems, namely: Front-End Electronics (FEE), Data Acquisition System (DAQ), Low Voltage (LV) and HV power supply, already described in Chapter 3.

7.2 Methods

In order to evaluate the individual sector performance, the acquired data was analysed separately for each sector, despite they were taken simultaneously in two sectors. The two sectors were only stacked to trigger each other.

7.2.1 Time resolution and timing tails

The time resolution is calculated for those particles with hits in overlapping cells by characterizing the distribution of Eq. 5.4 following the same procedure as already described in Section 5.3.4. Entries beyond ± 700 ps are also reported, as this is the characteristic π and K TOF difference [66]. The final results are already corrected by charge and longitudinal position as well. The average time resolution, e.g., average time resolution for a sector or for all sectors, is calculated as the mean of a Gaussian fit to the distribution of individual σ_t.

7.2.2 Multi-hit time resolution

The time resolution was also calculated in a multi-hit environment (more than one particle per event). The same analysis described in Sec. 7.2.1 was repeated on S_2 for a restricted set of data, in which it was required that each primary hit (two hits in overlapping cells) had at least one another hit, secondary, at a distance D (this distance refers to rows). So, $D = 0$ means that each primary hit in a given row has at least other secondary hit in the same row. $D = 1$ means that each primary hit in a given row, n, has at least one other secondary hit in row number $n-1$ and $n+1$ and no secondary hits are present in the same row, etc. It has been also analysed a set of data with only a primary hit in the sector, which would correspond to a distance $D = \infty$, in contrast with the standard analysis, Sec. 7.2.1, which include events with primary hits and eventually one or more secondary hit.

7.2.3 Position resolution

The longitudinal position resolution is calculated as descibed in Section 5.3.3 as well.

7.2.4 Crosstalk

When a cell fires, due to the passage of a particle (real hit), there is a certain probability of firing a neighbour cell due to the influence of the first. These “fake” hits are called crosstalk

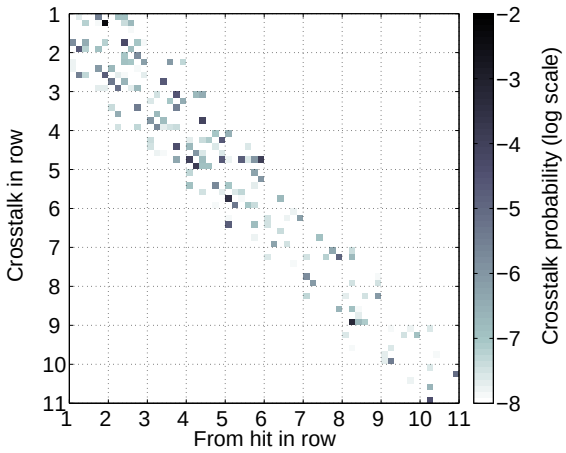

Figure 7.2: Detail of crosstalk in one of the current sectors.

hits. The sectors were built trying to minimize this effect but despite of all the precautions [54], it is impossible to eliminate it completely. The crosstalk hits can be identified because these are hits with a physically impossible longitudinal position along the cell or a charge measurement compatible with zero.

The crosstalk between all pairs of cells in a prototype sector has been already studied [54], showing that the crosstalk is a short range effect influencing fundamentally the cells in the same, previous and next rows, as can be appreciated in Fig. 7.2 (detail of crosstalk in one of the current sectors, S_2). Here, it is calculated, for all sectors, the average number of crosstalk hits per real hit, as a function of the cell where the real hit took place.

7.3 Results

7.3.1 Time resolution and timing tails

Fig. 7.3 shows the time resolution, σ_t, for the entire chain (cell + FEE + DAQ), as a function of cell for all sectors (different columns in each sector are superimposed). Out of a total of 1116 cells, 1115 are operative along with the corresponding 2230 FEE (one cell on S_2

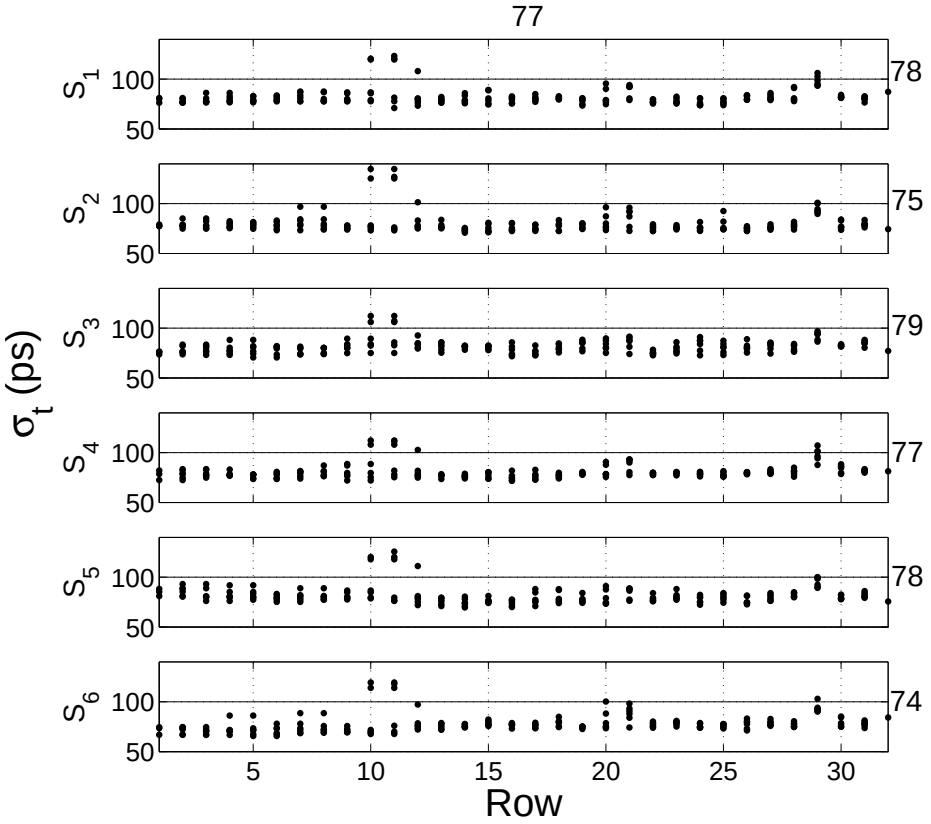

Figure 7.3: Time resolution σ_t as a function of cell (row) for all sectors. The average resolution is written in the right side for each sector, and an whole average of 77 ps is obtained.

was accidentally disconnected during the transport to GSI). All channels have a resolution under 100 ps, without noticeable correlation with cell position, except 36 channels with a resolution large than 100 ps (points above black line in Fig. 7.3). These channels are affected by the integral non-linearity of the Time to Digital Converter (TDC) and it is expected that the degradation will vanish once this effect is corrected. The values to the right of each axis are the average time resolution for each sector (excluding the channels affected by the integral non-linearity), while the value at the top of the figure is the average time resolution for all cells in all sectors, 77 ps.

The timing tails, symmetric both right and left, have an average value for all cells in all sectors of 3.6% for 3σ tails while entries beyond $\pm$700 ps have an average value of 0.6%.

7.3.2 Multi-hit time resolution

Fig. 7.4 shows the multi-hit average time resolution for S_2 as a function of D (see Sec. 7.2.2). The time resolution degrades up to a value of 105 ps when a secondary hit is in the proximity of the primary hit (same row, $D = 0$ or previous / next row $D = 1$). In the rest of scenarios ($D > 1$) the average time resolution is basically not affected and shows the same value as in the standard analysis. The time resolution for the $M2$ set of data is also shown, exhibiting roughly the same value when compared with the standard analysis. For all scenarios, the multi-hit average time resolution is 83 ps

7.3.3 Position resolution

Fig. 7.5 shows the position resolution, σ_x, as a function of cell for all sectors (different columns in each sector are superimposed). σ_x would be the intrinsic longitudinal position resolution of the RPCs if all the acquired cosmic rays were perpendicular (which is not the case). There is a dependence with the row (increasing from around 8 mm for the lower rows up to 10 mm for the upper rows), which can be attributed to the larger polar angle accepted by the trigger as the row and the longitudinal dimension of the cells increases. Despite this

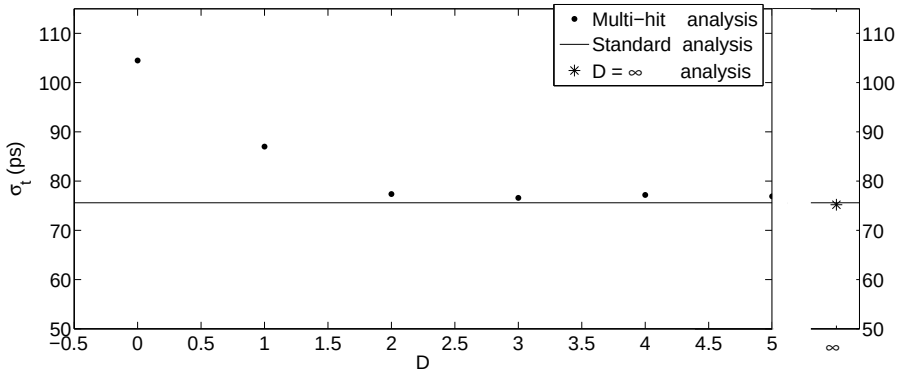

Figure 7.4: Multi-hit average time resolution for S_2 as a function of D, distance in rows from the primary to the secondary hit (see text).

geometrical contribution (inherent to this setup), the average position resolution for all sectors is 8.4 mm (individual values for each sector are shown to the right of each axis) with all cells under 12 mm.

7.3.4 Crosstalk

Fig. 7.6 shows the average number of crosstalk hits as a function of the cell where the real hit takes place. The values to the right of the axis are the average number of crosstalk hits for each sector and the value at the top of the figure is the average number of crosstalk hits for all cells in all sectors, 0.4%. Most of the cells do not produce noticeable crosstalk, except a few cells (twelve) -mostly located in the lower rows-, which show maximum values of around 10%. The reason for this is not understood at present.

7.4 Conclusions

The six sectors of the new HADES-TOF wall based on RPCs were tested successfully with cosmic rays prior to the final installation in the spectrometer at the end of 2009.

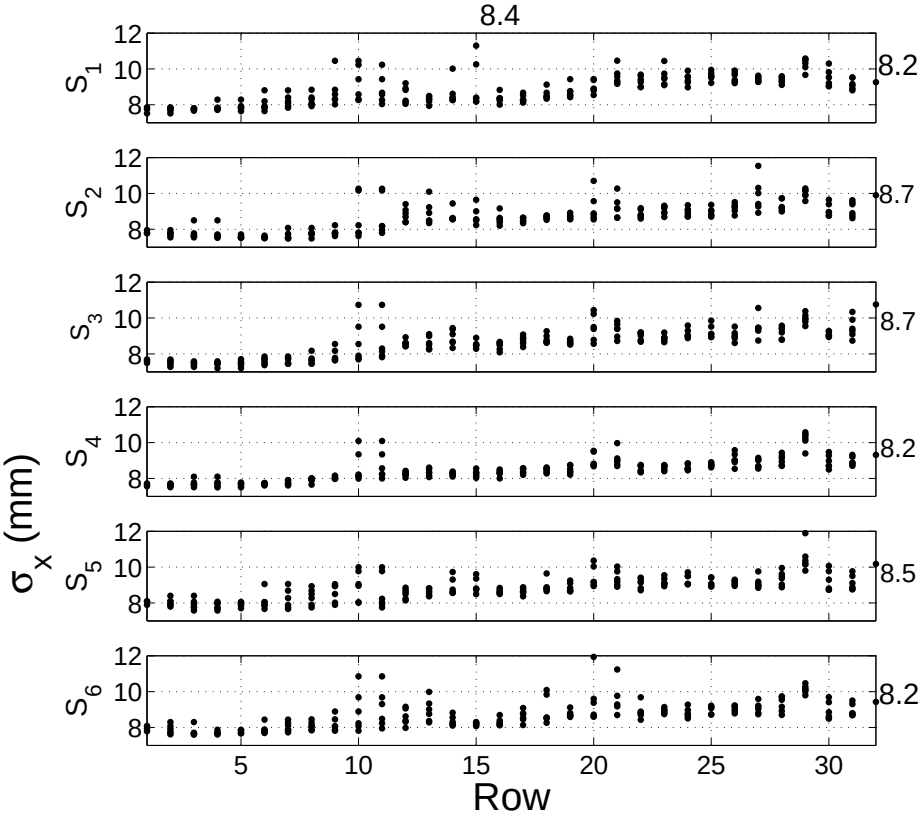

Figure 7.5: Position resolution σ_x as a function of cell (row) for all sectors. The average resolution is written in the right side for each sector, and an whole average of 8.4 mm is obtained.

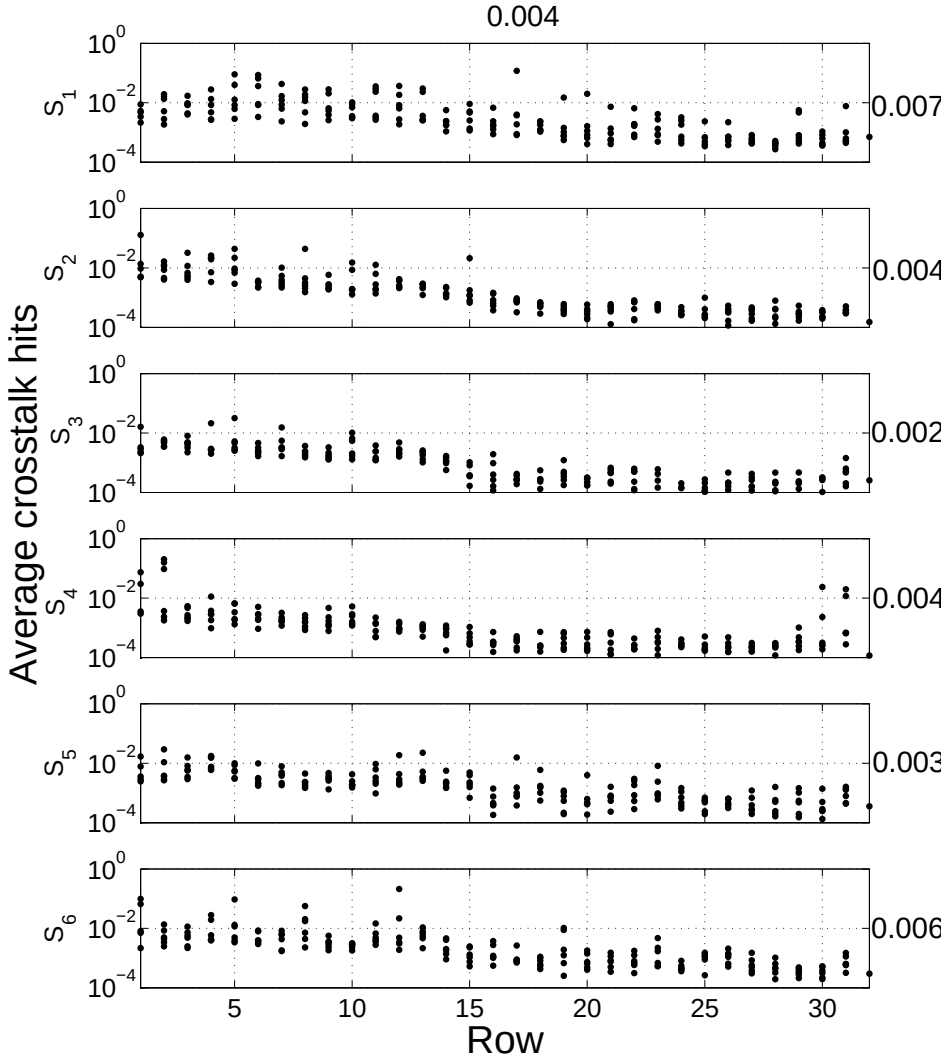

Figure 7.6: Average number of crosstalk hits per real hit as a function of cell where the real hit takes place.

All cells, 1116, together with the corresponding FEE are operative (except one cell that was disconnected accidentally in the transport). A time resolution better than 100 ps was measured for all cells in all sectors with an average value of 77 ps together with symmetric timing tails at a level of of 3.6% for 3σ tails and 0.6% for entries beyond $\pm$700 ps. If necessary, the timing tails could be decreased for a fraction of all particles crossing the detector, thanks to the redundant double layer configuration [92].

The multi-hit time resolution has also been measured showing a degradation up to 105 ps when a secondary hit is in the same row as the primary hit. Hits located beyond the first neighbouring row do not show any appreciable degradation. For all scenarios, the multi-hit average time resolution is 83 ps.

The average longitudinal position resolution for all cells and sectors is 8.4 mm with a maximum value of 12 mm, affected by geometrical specificities of this setup.

The crosstalk was measured between all pairs of cells showing that it is a short range effect confirming previous measurements in a prototype. The average number of crosstalk hits per real hit for all cells in all sectors shows a modest value of 0.4%.

Chapter 8

The HADES tRPC Beam Commissioning

In November of 2009, all tested and fully instrumented sectors of the HADES tRPC wall were mounted in their nominal position in the Spectrometer (as shown in Fig. 3.16). During the first months of 2010 the installation was completed with the remaining issues, like DAQ and trigger systems, Slow Control hardware, etc, and the full wall was once again validated.

For the HADES Upgrade commissioning, including the tRPC wall, four main beamtime periods were schedule by the collaboration: July 2010 (*jul10*), September 2010 (*sep10*) and October 2010 (*oct10*) beamtimes, all with success in the corresponding improvements, and November 2010 (*nov10*) beamtime, which was schedule by the time of writing this document.

The three first beamtimes are here described; the data from the tRPC have been analyzed in detail for the *sep10* and *oct10* beam periods, and the most important features and results are presented in this chapter. They are also commented some basic features for the *jul10* beamtime. Finally, very recent results from *nov10* beamtime are presented.

8.1 July 2010 Beam Time Analysis

From July 19^{th} to 25^{th} 2010, two kind of beams were delivered to the HADES cave. As the HADES Collaboration was not the main user, there were only a few hours of data taken per day.

Prior to beam data, the tRPC wall was fully checked and validated with cosmics. It was almost the definitive setup. Only the BLR trigger board described in Section 3.3.5 was not available, and therefore a previous and simpler version was used instead for delivering the trigger signal from the tRPC. The dark rate of the wall was measured working at nominal HV (5.6kV) and nominal FEE thresholds of -40 mV [35]. The measured rates were about 2 kHz for sectors 0 and 1, 3 kHz for sector 5, 4 kHz for sector 3 and about 12 kHz for sectors 2 and 4. These two high counting sectors are known to be a bit noisy but their performances are anyhow good. Thus, the full multiplicity 1 (M1) for the tRPC was about 35 kHz. By increasing the discriminator threshold of the trigger signal, higher multiplicities were selected, yielding values of 1.1 kHz for M2, 0.4 kHz for M3 and 0.14 kHz for M4.

The first beam was a $48Ca^{+20}$ at 1.25 *A*GeV hitting over a segmented Au target, consisting on 15 thin gold slices of 2.5mm diameter, with a total length of 53.6 mm (including gaps between slices). The beam intensity in SIS ranged from $0.5{\cdot}10^6$ ions/spill up to 10^8 ions/spill, with a 4 s spill duration. In the mid-range, data with intensity of $2{\cdot}10^7$ ions/spill in SIS were taken. This meant up to $750{\cdot}10^3$ tRPC triggers per spill ($2.5{\cdot}10^6$ tRPC+FW triggers per spill). The power consumption of the tRPC wall was about 8 μAmps per layer (while the dark current consumption is about 5-10 nAmps per layer). The DAQ system acquisition rate was of about 60 kHz (peak), while about 200 MB/s (280 MB/s peak) were written to the disk, running in parallel several event builders.

A heavier system was scheduled for the second beam, and a $238U^{+78}$ beam at 900 *A*MeV, on the same Au target, was delivered for the first time into the HADES cave (even a heavier system than the foreseen Au-Au system). The beam intensity was up to $0.65{\cdot}10^7$ ions/spill in SIS, with a 4 s spill duration. Up to about 10^6 reactions per spill were triggered. The power

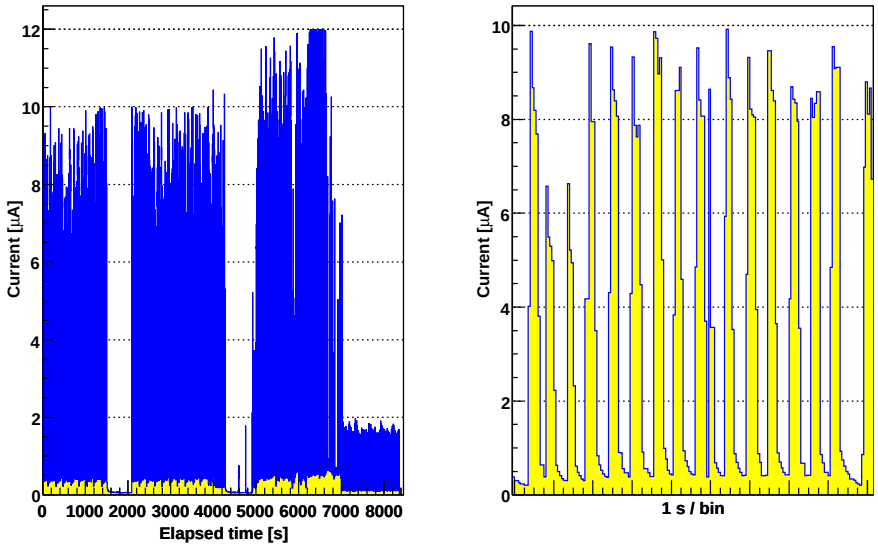

Figure 8.1: Current consumption per layer for different Ca beam intensities (left) and a zoom of that (right), where the 4 s spill is shown. Note that it is plotted in 1 s/bin

consumption of the tRPC reached 10 μAmps per layer at maximum beam intensity. Although and the average multiplicity per event was about 50 over the tRPC wall, the rate was about 100-200 Hz/cm^2, still far from the critical point for a proper operation [30].

During this beamtime period, no major operations were performed with the tRPC wall besides the full validation of the wall. Also the system stability was checked. No data was analyzed in detail.

Fig. 8.1 left shows the typical current consumption per tRPC layer at different Ca beam intensities during more than two hours, operating at nominal HV of 5.6 kV. At high intensity, the current consumption was greater than 12 μAmps per layer, while at very low intensity, that was not greater than 2 μAmps. Fig. 8.1 right shows a zoom where the 4 s spill structure is visible.

8.2 September 2010 Beam Time Analysis

In September 2010, a $64Ni^{+26}$ at 1.25 *A*GeV beam was delivered into the HADES cave and hit the segmented Au target. Some new features were tested in the spectrometer: among others, the BLR board described in Section 3.3.5 was used for the tRPC trigger distribution and also for the Central Trigger System (CTS), collecting the trigger signals coming from the tRPC, the TOF and the FW.

The new Start detector described in Section 1.3.3 was also tested. A second polycrystalline diamond detector was also installed but it was not operational.

The tRPC was usually operated at nominal HV of 5.6 kV and FEE thresholds of -40 mV. The stability of the wall was checked once again, and some features were measured.

As the magnetic field was switched on at full intensity (3200 Amps) during one day of data taken, their results are treated separately from those without magnetic field.

8.2.1 No Magnetic Field data

The beam intensity was up to $2{\cdot}10^6$ ions per spill in SIS (4 s spill), which meant about $2{\cdot}10^5$ M2 tRPC triggers per spill (runs with much lower beam intensity were taken). The average multiplicity per event was at the order of 15 in the tRPC (see Fig. 8.2 (a)) so that the maximum rate over the wall was about 100 Hz/cm^2. The DAQ was running up to 30 kHz and up to 300 MB/s were written to the disk.

In order to set the tRPC working point, some data were taken at different applied HV, and the rates and current consumptions were recorded. Fig. 8.2 (b) shows the average current per layer under low intensity beam versus the applied HV. Although in the plot are represented the averages over the data taken (that is, 4 seconds spill, 4 second any), peaks of some μAmps were reached easily at HV=6000 V for sectors 2 and 4 (counting from 0). Note that the picture is in logarithm scale.

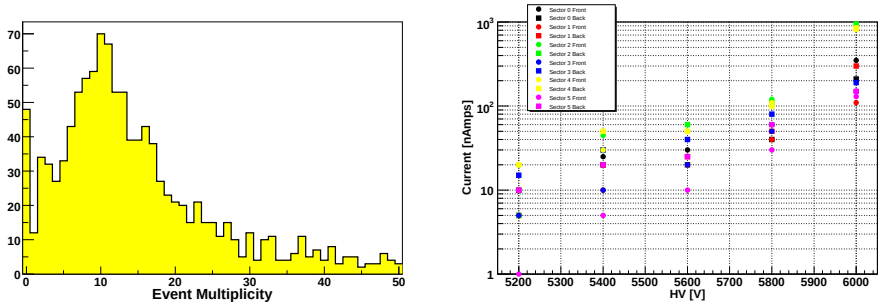

(a) (b)

Figure 8.2: (a) tRPC event multiplicity for sep10 no field beam data. (b) Average current per layer versus the HV for low intensity beam (values from EPICS Archiver)

8.2.1.1 Raw Time Resolution

The *raw* time resolution (without charge and position corrections) was calculated for the tRPC in the usual way by means of the existing cell overlap (see Section 5.3.4), giving a value of 110 ps (σ) in average, with a very regular behaviour over the whole wall, as it is shown in Fig. 8.3. As the raw time resolution is here calculated independently through the two overlaps of a single cell, those geometrically smaller overlaps give a bit worst result. This effect occurs in the lower polar angle region, as it can be clearly devised in the picture.

8.2.1.2 Matching Efficiency

For the *sep10* no field data, the tRPC track matching efficiency was calculated. A similar procedure as that from Section 5.3.2 was applied. Nevertheless, a couple of eventual features made this analysis stronger than that. On the one hand, as the Shower detector was not fully operative all the time, the amount of collected statistics was in the limit to perform a valid analysis. On the other hand, the working point of the MDCs was not optimum: inner chambers were operated at low efficiency, and outer chambers were not used at all. Besides, there wasn't any kind of detectors alignment. Thus, the track direction was obtained from the hit cluster in

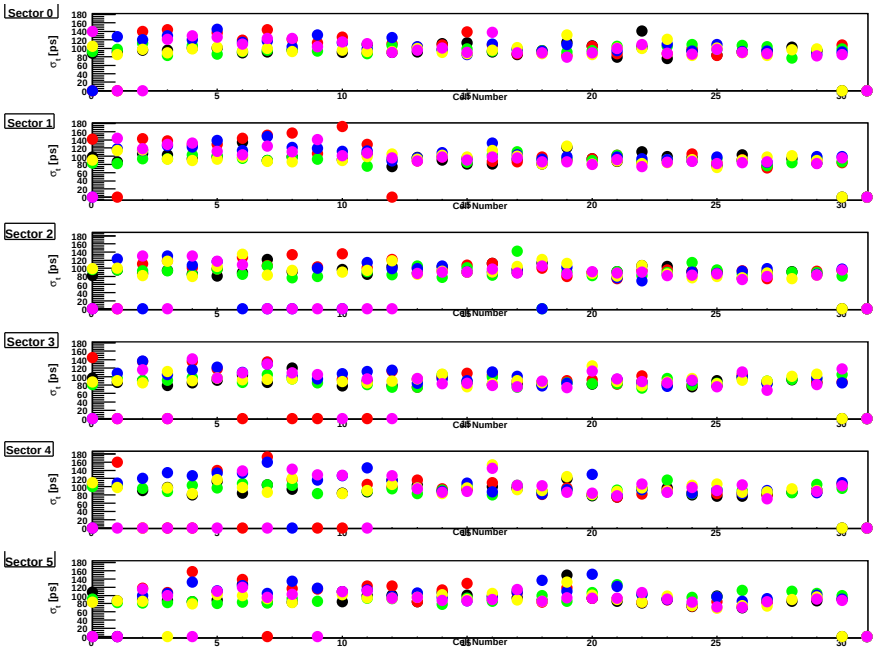

Figure 8.3: tRPC raw time resolution for no field data. The time resolution is calculated independently through the two overlaps of a single cell.

MDC plane II and the target point. The track was then extrapolated to the Shower and tRPC planes. As only a fraction of the reconstructed tracks came really from the target, a narrow searching window of ± 20 mm was open between the MDC and the Shower in order to define a valid track. Note that such window is basically the size of the bigger Shower pads.

Once a valid track was defined (matching MDC-Shower), the efficiency was calculated by looking at that track in the tRPC. Fig. 8.4 shows the matching efficiency distribution per each tRPC sector. An average matching efficiency of 94 $\pm 1\%$ was obtained (excluding geometric dead regions). The small asymmetry observed (less counting in right side of each sector) can be attributed at the lack of alignment. All the six sectors showed the same behavior.

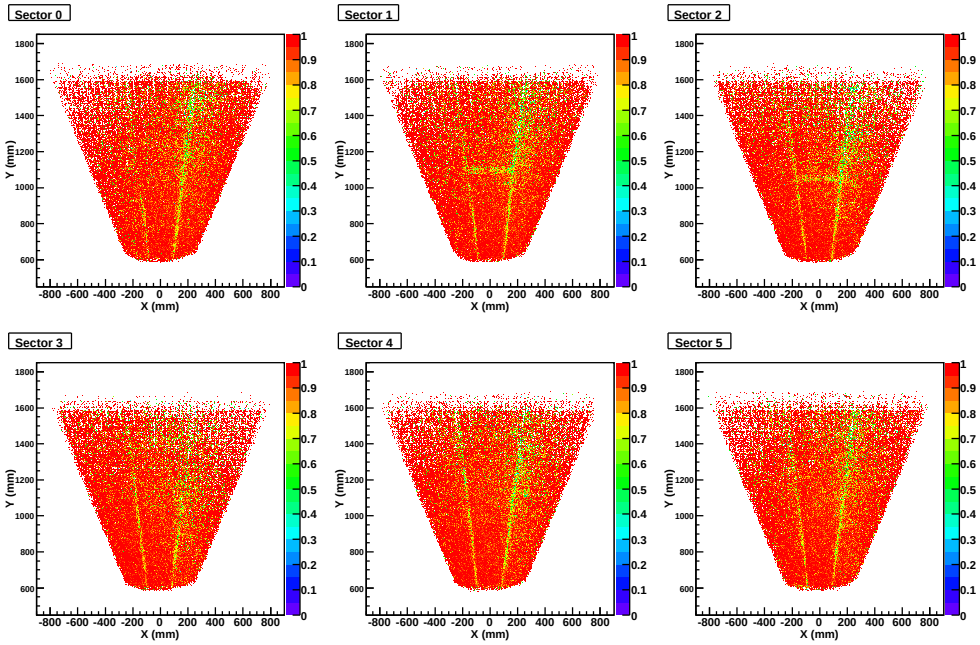

Figure 8.4: Matching efficiency distribution for all tRPC sectors with *sep10* no field data. The average efficiency was obtained to be $\sim 94\%$.

Fig. 8.5 (a) shows the X residuals for the tRPC-MDC track matching, that is, there it is plotted the distribution of the difference $X_{tRPC} - X_{MDC}$. From that, averaging over the six sectors, a matching resolution of $\sim$14 mm (σ) is obtained. Taking into account the low MDC efficiency and resolution and the lack of alignment in this run, the matching resolution obtained here is in agreement with the previous measurement with the prototype already reported in Chapter 5, where a value of 10.2 mm (σ) was reported but in better working conditions.

As the Y position in the tRPC is given only by the geometry of the fired cell, it makes no sense to perform any kind of fit to the Y residuals distribution. Nevertheless, the RMS of the distribution was of about 20 mm, as it is shown in Fig. 8.5 (b).

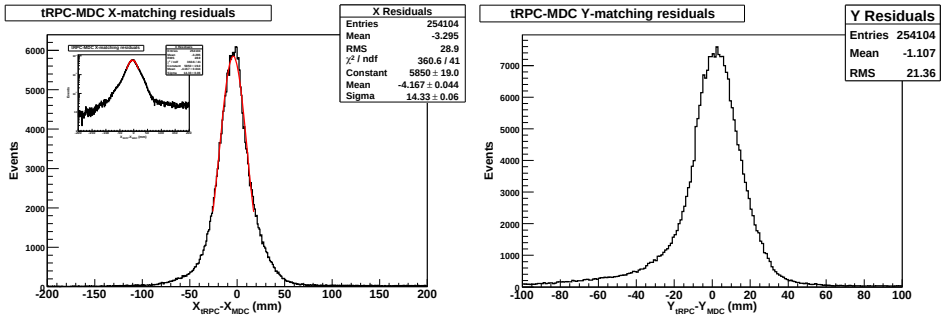

(a) (b)

Figure 8.5: (a) X residuals for tRPC-MDC track matching (also in logarithm scale), where a resolution of $\sim$14 mm (σ) is obtained. (b) Y residuals for the same matching

8.2.2 High Magnetic Field data

Under the same beam conditions as for no magnetic field runs, the same basic features were checked for the tRPC with high magnetic field data for the first time, and no degradation was observed at all in terms of system performances.

The system was calibrated following the methods described in Section 4.2.3 and the preliminary *tof* spectrum was obtained (see Fig. 4.4 (b)), not applying yet the second setup of *tof* calibration. A dst with particle identification (PID) purposes is currently under development, and the whole *tof* calibration is foreseen.

Nevertheless, a first effort has been done in order to do PID with the tRPC with such "rough" calibration. Fig. 8.6 shows the typical spectrum of momentum times particle polarity versus β, for minimum bias and very low statistics sample. The β is calculated from the tRPC *tof* measurement while track reconstruction is performed with the HADES tracking programs [93, 15] and momentum is reconstructed with the so-called *Spline* method [94]. In the negative polarity side, electrons and negative pions are identified, while protons, positive pions and positrons are visible in the positive polarity side. The picture is shown both in linear and logarithm Z color scale for a better visualization.

The hit distribution over the wall is shown in Fig. 8.7.

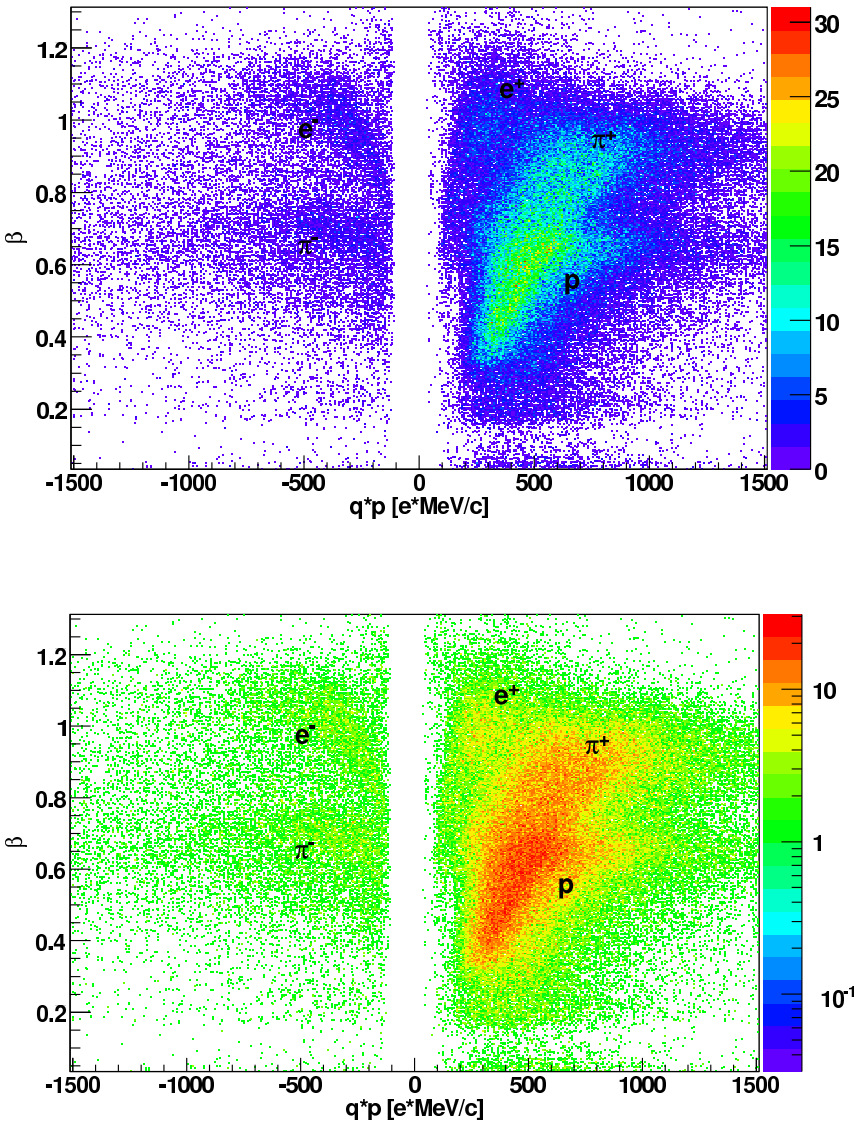

Figure 8.6: Momentum times polarity versus β spectra for *sep10* full magnetic field beam data with the tRPC, both in linear and log Z scale. Protons, π^+, π^-, and e^+, e^- species can be identified.

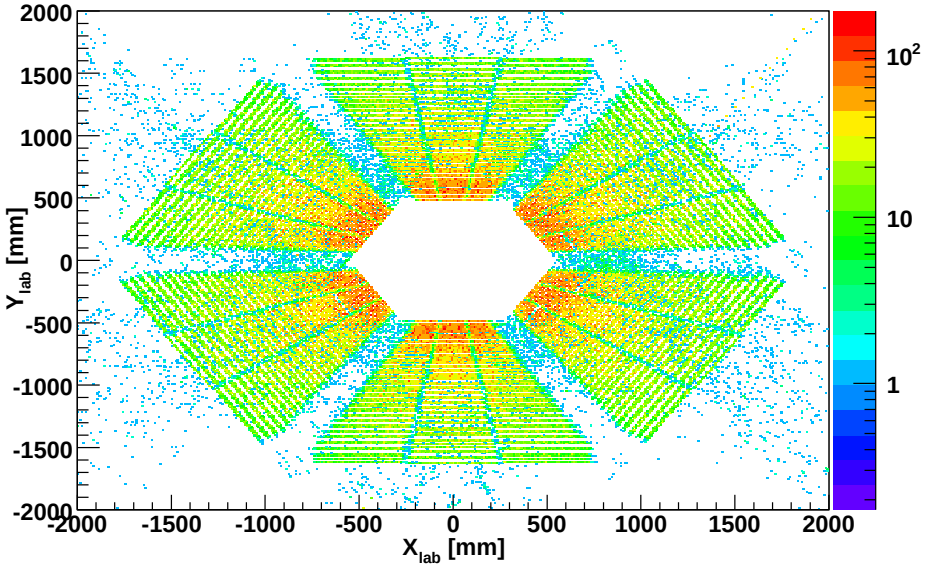

Figure 8.7: tRPC Hit Distribution in laboratory for high magnetic field data

8.3 October 2010 Beam Time Analysis

238U^{+78} beam at 1 *A*GeV, intensity of 2·10^6 ions per spill, with 3 s spill duration (70% of time flat top); 1% interaction probability in the target. The intensity was increased by a factor 4, up to 8·10^6 ions per spill, but high fluctuations were observed in the beam. M30 trigger rate of ∼55kHz

Although there were no problems in terms of current consumption, it was observed an amount of streamers greater than 1% when the tRPC was operated at a HV of 5.6 kV. So, it was decided to operated the wall at a HV of 5.5 kV, and that value can be taken as nominal from then on. According to Section 6.3.2.2, this can decrease the intrinsic efficiency for mips up to 90%. Nevertheless, such efficiency for beam is expected not to affected. The FEE thresholds were -40 mV.

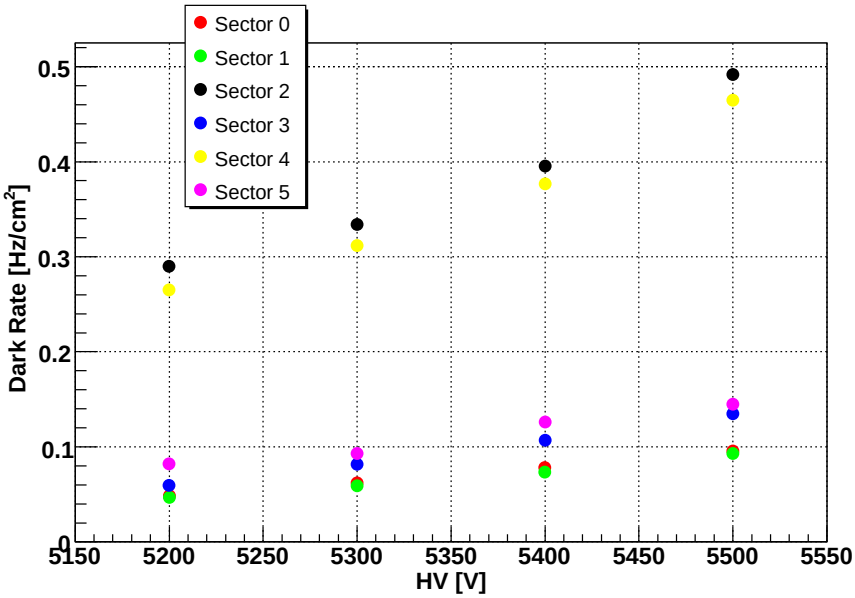

Figure 8.8: tRPC Sectors Dark Rate (M1) versus the HV, being the sectors placed in their nominal position

The multiplicity one (M1) rate for cosmics (or dark rate) was measured with the full setup (including new BLR and CTS), being the tRPC sectors in their nominal position. The results are shown in Fig. 8.8 as a function of the HV. These results are, in average, lower than those obtained from cosmic tests (see Chapter 7) and for *jul10* measurements (see Section 8.1). This can be attributed at two different factors: on the one hand, the effective area for cosmics is much lower being the sectors in their nominal position, and on the other hand, it is known that detector performances are getting better and better while the chambers are fed at nominal HV and gas flux. The two noisy sectors are clearly differentiated in the picture.

Fig. 8.9 shows two shots for the EPICS HV current monitor when no beam was in the cave (Left) and medium intensity U beam was delivered (Right). The tRPC was operated at a HV of 5.5 kV.

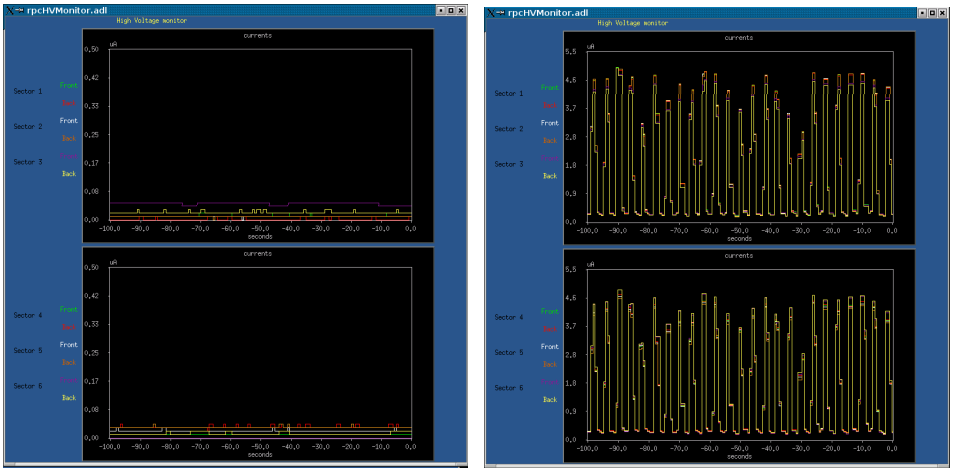

(a) (b)

Figure 8.9: Current Monitor for the tRPC working at HV = 5.5 kV. Left: no beam was in the cave; Right: medium intensity U beam. Note that the vertical scale is different in both pictures.

One of the important tRPC features to be checked with that U beam was the multiplicity recorded by the wall. As the new CTS was fully operative, different trigger multiplicities could be set independently, and data was taken. Fig. 8.10 shows the normalized multiplicity distribution both for TOF and tRPC when the analog multiplicity trigger was set to M>=30 in the CTS and asking for a coincidence with the Start detector. Events with multiplicity up to 150 in the tRPC were recorded (which means an occupancy of 14%), while the average was close to 70 (with the peak of the distribution placed at M30).

8.4 November 2010 Beam Time Analysis

The same conditions as for *sep10* beamtime were reproduced in the *nov10* beamtime setup. The magnetic field was also operative, and the Collaboration aims to do Physics with time resolution below 100 ps for the first time.

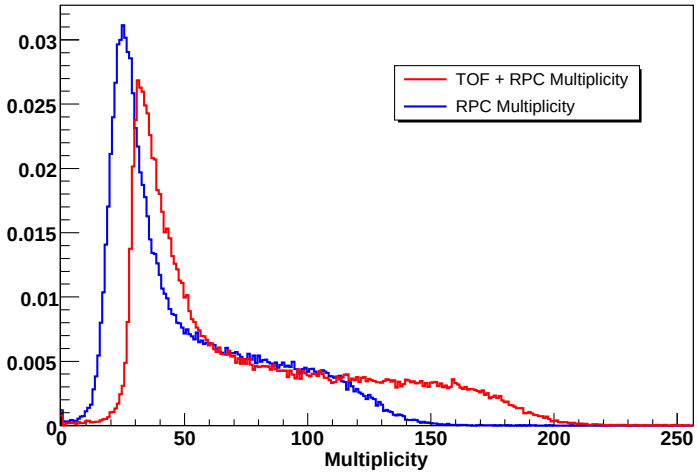

(a)

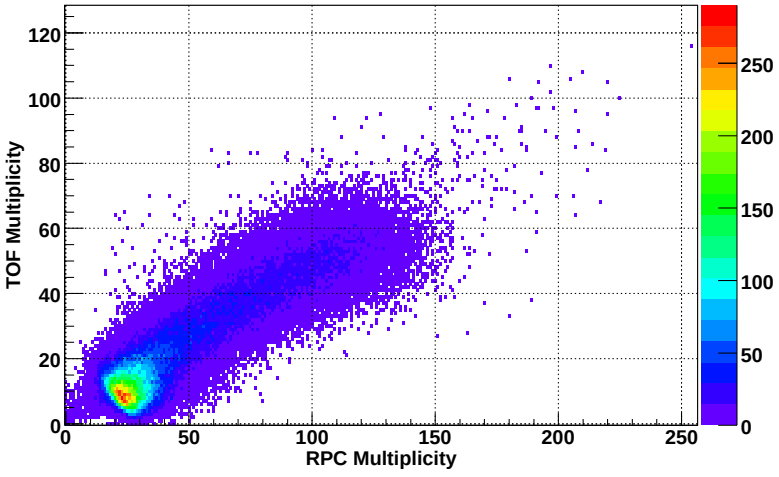

(b)

Figure 8.10: (a) Normalized TOF + RPC multiplicity and (b) TOF versus RPC multiplicities for U beam with analog multiplicity trigger in the CTS set to M>=30 (PT3) in coincidence with the START detector. The beam has about 1.3 Mions of U per spill on Au target. DAQ shows 8-10 kHz of accepted triggers

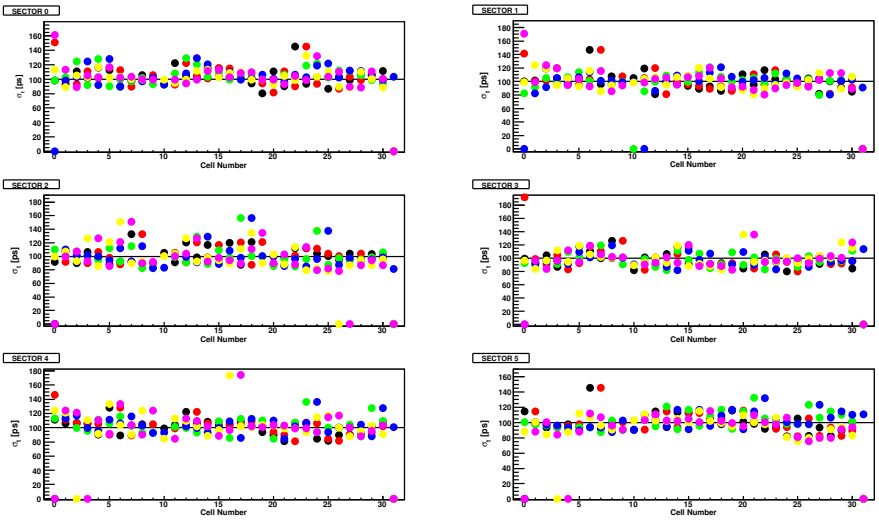

Figure 8.11: tRPC Raw time resolution for nov10 magnetic field data. An average value of 110 ps is obtained. The black line corresponds to the expected threshold of 100 ps.

For that goal, a great effort has been done and some improvements were reached concerning calibration and time resolution in the tRPC wall. A dst is under development.

8.4.1 Raw time resolution

The raw time resolution has been calculated in the same way as it is in section 8.2.1.1 but the worsening produced by the small geometric overlap in the lower angle region was simply avoid by removing those overlaps from the analysis. Nevertheless, an average value close to 110 ps is again obtained, as it is shown in Fig. 8.11 for magnetic field data.

8.4.2 Corrected time resolution

Fig. 8.12 shows the time resolution obtained with the tRPC after applying a Integral non-linearity (INL) correction in the TDC data and once the Slewing Correction from section

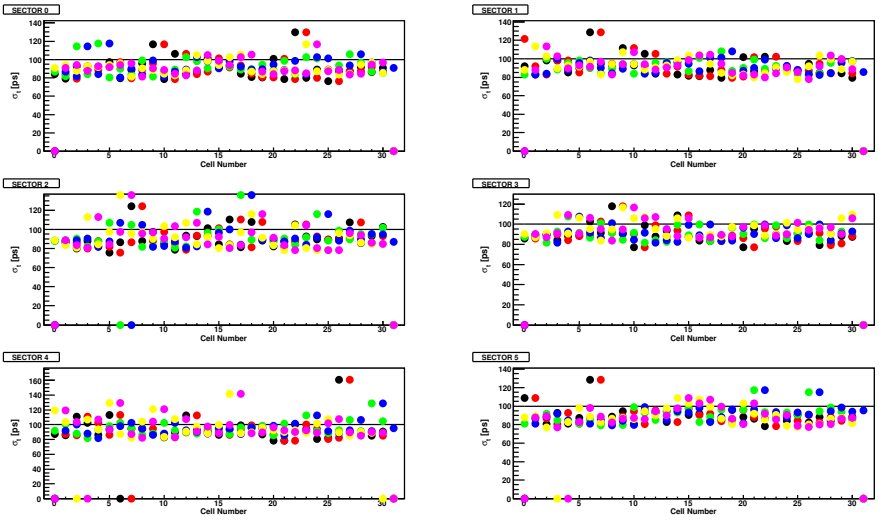

Figure 8.12: Time resolution for the tRPC once the INL and Slewing corrections were applied to the data. An average of 90 ps is obtained with high regularity for magnetic field data. The black line corresponds to the 100 ps value.

4.2.4.1 was included in the data chain analysis. With this, an average value of 90 ps is obtained and even with much more uniformity. The Slewing Correction gives a typical improvement of 20 ps, and the TDC INL correction helps significantly in those pairs of overlapped cells which do not share the same TRB; as expected, the degradation related with the INL effect was removed (see section 7.3.1).

8.4.3 Particle Identification

8.4.3.1 tRPC Calibration

For the first generation of *nov10* dst, data from RICH detector was not available due to some problems with RICH's data analysis. Besides, only Sector 3 (lowermost) was full operative for tracking devices. Therefore, no lepton selection was possible for *tof* calibration purposes and the second step of the method in 4.2.3.3 was not done. Instead, a proper calibration

method based on fast pions selection was developed for these data. Thus, negative charged tracks with momentum above 300 MeV/c^2 were selected.

The proper value of β for past pions was used to calibrate the first cells of the three front layer columns in the operative sector, and the reminder cells were calibrated with respect to those by means of the existing overlap. At the end, three isochronous regions were done in the tRPC sector.

8.4.3.2 Track Selection and Identification

Once the wall was calibrated, only the center columns in the tRPC were selected for analysis. Besides, they were selected low multiplicity events and tracks with good quality of matching between mdc system and META detectors.

Fig. 8.13 shows the typical PID plot of β versus momentum both for tRPC and TOF detectors. Positive and negative pions, protons and deuterons are clearly identified. Also tritium can be made out. No leptons are identified. The PID capabilities of the tRPC seem to appear better than those of the TOF detector, but we must keep in mind that such data represents only the first iteration in analysis. It is expected that both tRPC and TOF give even better results in PID in further analysis (next generations of dst).

From the picture, one can also see how higher momentum particles are focused in the lower polar angle region (tRPC) due to the Lorentz boost, as the average momentum in TOF is lower than in tRPC. Since the histograms are not normalized to the number of events, and represent only a small fraction of the solid angle, we can not see nothing about the density distribution of different species (one can expect more heavy hadrons in the lower polar angle region).

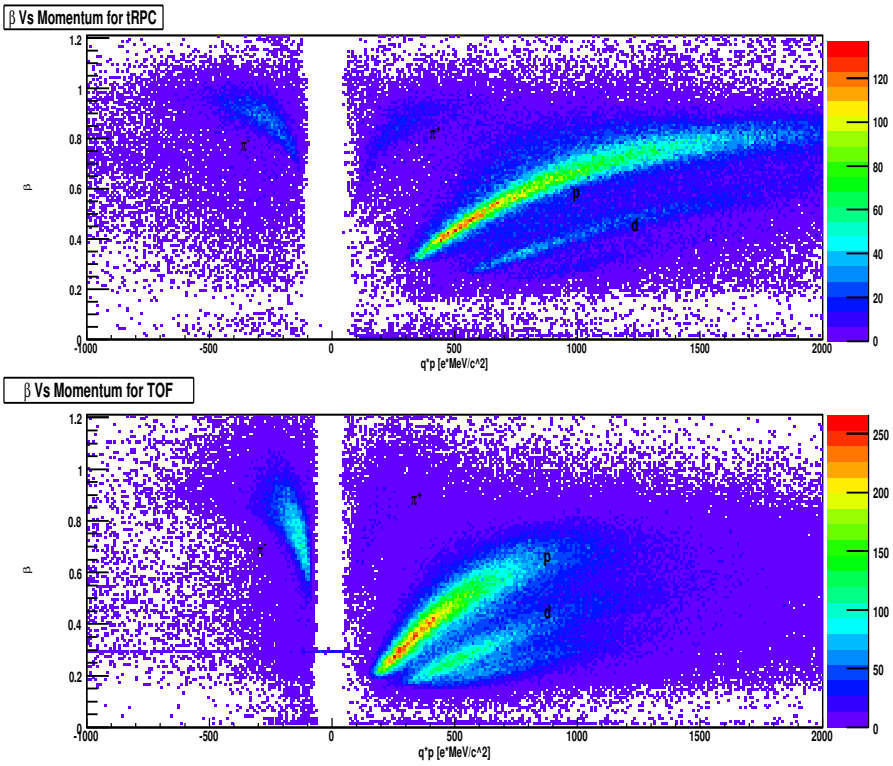

Figure 8.13: Momentum times polarity versus β spectra for *nov10* full magnetic field beam data both with the tRPC (up) and the TOF detector (down). Protons, Deuterons, π^+ and π^- species can be identified.

Conclusions

The work presented in this memory summarizes all the tasks the author has done related with the development, construction, testing, commissioning, and installation of the timing Resistive Plate Chamber (tRPC) Time-of-Flight wall of the HADES spectrometer at the GSI in order to extract from it the best possible performances.

Here, the main contributions and conclusions are reported.

All the needed software related with the integration of the tRPC wall in the HADES Spectrometer was developed. The full data reconstruction chain was completed: starting in the lower level of data, the unpacking, calibration, hit finding and cluster finding tasks were written. The corresponding algorithms were developed and tested with real data. Together, a realistic digitization of simulated data was also written. All the code for the on-line tRPC monitoring and QA plots was developed as well. The auxiliary code needed to perform the analysis of data was also written. As a consequence, the tRPC is fully integrated within the HADES software framework.

We participated in the testing of a first tRPC prototype sector. The results of a technical analysis of data contributed significantly to the final design. Time resolutions, intrinsic and matching efficiencies and spatial resolution, and performances as a function of the rate and HV were measured. Started from an overall *raw* time resolution of 100 ps (σ), a final time resolution of 73 ps (σ) was achieved after applying the charge and position corrections, which fulfilled the design requirements. The intrinsic efficiency and position resolution were of 99%

and 7.7 mm respectively and matching efficiency and position resolution were at the level of 97% and 12 mm. No degradation was observed operating at nominal HV under rates up to 100 Hz/cm^2, with negligible timing tails and crosstalk.

We performed a dedicated experiment with a C^{12} beam to analyze the performances of the final tRPC cells under realistic highly-ionizating conditions. The cell behaviour and element identification capabilities were studied, as well as the influence of ions up to Z=6 in the time-charge and space-charge correlations. A good operation up to C^{12} fluxes of 100 Hz/cm^2 was demonstrated with time resolution $<$100 ps (σ) and $\varepsilon \simeq$100%. Above 100 Hz/cm^2 the time resolution deteriorates rapidly but the efficiency was kept up to 600 Hz/cm^2 due to the much higher initial ionization as compared with minimum ionizating particles.

All the six fully instrumented tRPC sectors were later tested and validated with cosmic rays, using a dedicated setup at GSI. Their performances regarding the time resolution and timing tails, position resolution, crosstalk between channels and long-term stability were checked, showing comparable features as those obtained with the prototype. In November 2009, the six sectors were installed in their nominal position in the HADES Spectrometer.

The tRPC wall contributed to the HADES upgrade commissioning beamtimes started in July 2010. The performances of the wall were measured under collisions coming from different beam species on a Au target. A matching efficiency for the tRPC wall of 95% was obtained in a non-optimum tracking system environment, and a time resolution below 100 ps (σ) was corroborated after the *slewing correction*. In September 2010, the full wall operated for the first time under maximum intensity magnetic field, and same conditions were set in November 2010. The analysis showed no degradation, and its behaviour was reported. The wall was calibrated and DST processes have started for analyzing the recorded data. We have shown for the first time the Particle Identification (PID) capabilities of the tRPC to separate protons, pions and electrons, as it is shown in the picture.

The performances reached with the HADES tRPC (and its evolution) are summarized in Table C.1.

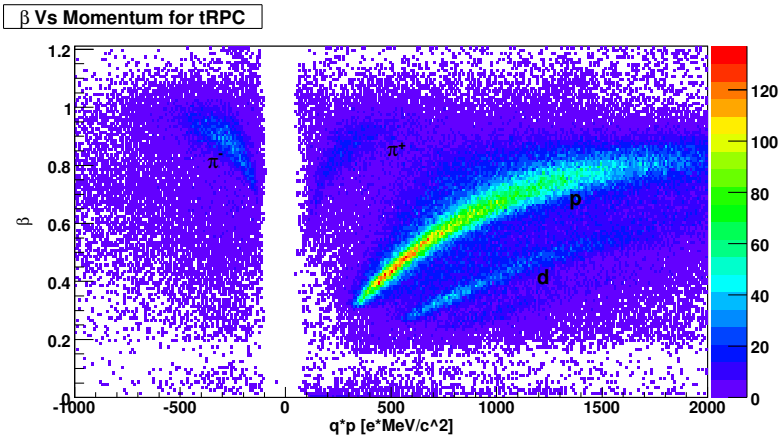

(a)

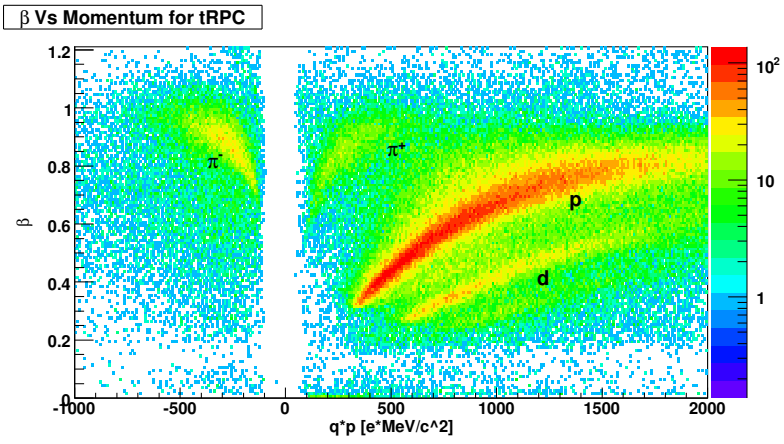

(b)

Figure C.1: Momentum times polarity versus velocity β for full magnetic field *nov10* data with the tRPC, both in linear (a) and logaritmic (b) scale. Protons, deuterons, π^+ and π^- are clearly identified. No lepton selection was performed yet to the *nov10* data.

Detectors	Year	Phys. Enviroment	HV (V)	Max. Rate (Hz/cm^2)
Sector Prototype	2007	Beam	5800	80
Individual cells	2008	Beam/Cosmics	5600	100
6 Sectors	2009	Cosmics	5600	10^{-2}
Full Wall	2010	Beam	5500	100
Intrinsic Eff. (%)	Matching Eff. (%)	Raw σ_t (ps)	Corrected σ_t (ps)	σ_{pos} (mm)
$\sim$99	97.5	96	73	7.7
$\sim$99/$\sim$ 95	-	-	$\sim$80/$\sim$100	-
-	-	-	77	8.4
-	94 ± 1	110	90	-

Table C.1: Summary of tRPC performance evolution: results from the four main data taken periods are presented together with the working conditions.

Seven years after starting the project, the whole tRPC wall detector has been finished and is already installed in the Hades spectrometer. The detector keeps ready to contribute to the oncoming Physics challenges of the HADES Collaboration both at its present programme and as a part of the future FAIR Project. We have directly contributed to the fact that the performances expected during the design have been reached and even improved. The reconstruction software and the analysis tools developed are perfectly working and ready to be used by the collaboration. A big effort have been done in order to keep all the information and documentation available.

Bibliography

[1] G.Agakichiev et al. *Physical Review Letters*, 98:052302, 2007.

[2] G. Agakichiev et al. *Physical Review C*, 80:025209, 2009.

[3] `http://www-hades.gsi.de`.

[4] `http://pdg.lbl.gov`.

[5] G. E. Brown and M. Rho. *Physical Review Letters*, 66:2720, 1991.

[6] R. Rapp and J. Wambach. *Adv. Nucl. Phys.*, 25:1, 2000.

[7] G.Agakichiev et al. *Eur. Phys. J. C*, 41:475, 2005.

[8] R. Arnaldi et al. *Physical Review Letters*, 96:162302, 2006.

[9] S. Afanasiev et al. *nucl-ex*, 0706.3034.

[10] R.J.Porter et al. *Physical Review Letters*, 79:1229, 1997.

[11] D. Trnka et al. *Physical Review Letters*, 94:192303, 2005.

[12] M. Naruki et al. *Physical Review Letters*, 96:092301, 2006.

[13] L. Fabbietti et al. *J. Phys. G: Nucl. Part. Phys.*, 36:064005, 2009.

[14] G. Agakichiev et al. *Physical Review C*, 82:044907, 2010.

[15] G.Agakichiev et al. *Eur. Phys. J. A*, 41:243, 2009.

[16] B. Spruck et al. *Scintillating fiber detectors for high intensity pion beams at HADES. GSI Scientific Report*, 2004.

[17] HADES Collaboration. *e-Print: arXiv:0906.0091 [nucl-ex]*, 2009.

[18] `http://www-aix.gsi.de/~kaos/html/kaoshome.html`.

[19] M. Palka et al. *Presented at 2008 IEEE Nuclear Science Symposium (NSS)*, doi:10.1109/NSSMIC.2008.4774677, 2008.

[20] J. Michel et al. The new hades data acquisition network. *GSI Scientific Report*, 2009.

[21] D. González Díaz. *Research and Developments on Timing RPC's. Aplication to the ESTRELA Detector of the HADES experiment at GSI.* PhD thesis, USC, 2006.

[22] D. Pérez Loureiro. *Conceptual Design of a Large Area Time-of-Flight Wall for the R^3B experiment at FAIR.* Diploma Thesis, USC, 2005.

[23] R. Santonico and R. Cardarelli. Development of resistive plate counters. *Nucl. Instr. and Meth.*, 187:377, 1981.

[24] R. Cardarelli, R. Santonico, A. Di Biagio, and A. Lucci. Progress in resistive plate counters. *Nucl. Instr. and Meth. A*, 263:20, 1988.

[25] E. Cerron Zeballos et al. A new type of resistive plate chamber: The multigap rpc. *Nucl. Instr. and Meth. A*, 374:132, 1996.

[26] A. Blanco et al. A large area timing rpc. *Nucl. Instr. and Meth. A*, 485:328, 2002.

[27] H. Álvarez Pol et al. A large area timing rpc prototype for ion collisions in the HADES spectrometer. *Nucl. Instr. and Meth. A*, 535:277, 2004.

[28] P. Fonte, A. Smirnitski, and M.C.S. Williams. A new high-resolution tof technology. *Nucl. Instr. and Meth. A*, 443:201, 2000.

[29] P. Fonte. Applications and new developments in resistive plate chambers. *IEEE Transactions on nuclear science*, 49:881, 2002.

[30] A. Blanco, P. Cabanelas et al. *Nucl. Instr. and Meth. A*, 602:691, 2009.

[31] F. Giannini et al. *Nucl. Instr. and Meth. A*, 432:440, 1999.

[32] P. Moritz et al. *Diamond and Related Materials*, 10:1765, 2001.

[33] D. Belver et al. *IEEE Transactions on nuclear science*, 57:5, 2010.

[34] A. Blanco, N. Carolino, P. Fonte, and A. Gobbi. A new front-end electronics chain for timing rpcs. *IEEE Nuclear Science Symposium Conference Record*, 2:242, 2000.

[35] D. Belver. *The Front-End Electronics of the HADES timing RPCs wall: design, development and performances analysis*. PhD thesis, USC, 2009.

[36] A. Mangiarotti, P. Fonte, A. Gobbi. *Nucl. Instr. and Meth. A*, 533:16, 2004.

[37] A. Mangiarotti et al. *Nucl. Phys. B (Proc. Suppl.)*, 158:118, 2006.

[38] H. Raether. *Electron avalanches and breakdown in gases*. Butterworths, London, 1964.

[39] P. Camarri, R. Cardarelli, A. Di Ciaccio, R. Santonico. *Nucl. Instr. and Meth. A*, 414:317, 1998.

[40] P. Fonte. *Nucl. Instr. and Meth. A*, 456:6, 2000.

[41] W. Riegler, C. Lippmann, R. Veenhof. *Nucl. Instr. and Meth.*, 500:144, 2003.

[42] V. Ammosov et al. *Nucl. Instr. and Meth. A*, 578:119, 2007.

[43] A. N. Akindinov et al. *Nucl. Instr. and Meth. A*, 533:93, 2004.

[44] W. Yi et al. *Nucl. Instr. and Meth. A*, 538:425, 2005.

[45] A. Shuettauf. *Nucl. Phys. B (Proc. Suppl.)*, 158:47, 2006.

[46] P. Senger. *Phys. Part. Nucl.*, 39:1055, 2008.

[47] A. N. Akindinov et al. *Nucl. Instr. and Meth. A*, 602:658, 2009.

[48] J. Wu et al. *Nucl. Instr. and Meth. A*, 538:243, 2005.

[49] M. Ciobanu et al. *IEEE Transactions on nuclear science*, 54:1201, 2007.

[50] A. Gil. *Electronic Developments for the HADES RPC Wall*. PhD thesis, IFIC, Valencia, 2010.

[51] The HADES Collaboration. *Vector meson production in pA and πA collisions*. HADES Internal Report, 2006.

[52] A. N. Akindinov et al. *IEEE Transactions on nuclear science*, 48:2135, 2001.

[53] P. Cabanelas. *New Contributions to the Momentum Reconstruction Methods and First Analysis with Proton-Proton Elastic Collisions in the HADES Experiment*. Diploma Thesis, USC, 2005.

[54] D. Belver et al. The HADES RPC inner TOF wall. *Nucl. Instr. and Meth. A*, 602:687, 2009.

[55] A. Blanco et al. *Nucl. Instr. and Meth. A*, 535:272, 2004.

[56] A. Gil et al. *IEEE Transactions on nuclear science*, 56:382, 2009.

[57] I. Froehlich et al. *IEEE Transactions on nuclear science*, 55:59, 2008.

[58] `http://www.epics.org`.

[59] A. Gil et al. *Nucl. Instr. and Meth. A*, doi:10.1016/j.nima.2010.08.033, 2010.

[60] A. Blanco et al. Development of large area and of position-sensitive timing rpcs. *Nucl. Instr. and Meth. A*, 478:170, 2002.

[61] M. Sánchez García. *Momentum Reconstruction and Pion Production Analysis in the HADES Spectrometer at GSI*. PhD thesis, USC, 2003.

[62] R. Brun and F. Rademakers. Root-an object oriented data analysis framework. *Nucl. Instr. and Meth. A*, 389:81, 1997.

[63] `http://root.cern.ch`.

[64] Geant-detector description and simulation tool. CERN, 1993.

[65] D. Gonzalez-Diaz et al. Contribution to the XVIII HADES Collaboration Meeting, Ayia Napa, Cyprus, 2007.

[66] A. Mangiarotti et al. *Nucl. Instr. and Meth. A*, 602:830, 2009.

[67] P. Fonte et al. *Advances in gaseous time-of-flight detectors*. Proceedings of HEP2005, International Europhysics Conference on High Energy Physics, Lisbon, 2005.

[68] A. Blanco et al. *IEEE Trans. Nucl. Sci.*, 53:2489, 2006.

[69] R^3B Collaboration. *Technical Proposal, GSI Report*, 2005.

[70] H. Alvarez-Pol et al. *Nucl. Phys. B (Proc. Suppl.)*, 158:186, 2006.

[71] C. Lippmann, W. Riegler. *Nucl. Instr. and Meth. A*, 517:54, 2004.

[72] M. Abbrescia. *Nucl. Instr. and Meth. A*, 431:413, 1999.

[73] A. Gobbi, A. Mangiarotti. *Nucl. Instr. and Meth. A*, 508:23, 2003.

[74] W Riegler, C. Lippmann. *Nucl. Instr. and Meth. A*, 518:86, 2004.

[75] M. Bogomilov et al. *IEEE Transactions on nuclear science*, 54:2, 2007.

[76] V. Ammosov et al. *Nucl. Instr. and Meth. A*, 602:639, 2009.

[77] C. Lippmann, H. Vincke, W. Riegler. *Nucl. Instr. and Meth. A*, 602:735, 2009.

[78] D. Gonzalez-Diaz et al. *Nucl. Instr. and Meth. A*, 555:72, 2005.

[79] H. Stelzer. *Nucl. Instr. and Meth.*, 133:409, 1976.

[80] A. Breskin, N. Zwang. *Nucl. Instr. and Meth.*, 144:609, 1977.

[81] R. Ganz et al. *Nucl. Instr. and Meth.*, 432:379, 1999.

[82] P. Cabanelas et al. *JINST (Journal of Instrumentation)*, 4-P11007, 2009.

[83] A. Gil et al. *T11001 JINST*, 2, 2007.

[84] W. Koenig, J. Pietraszko. Comunication at DPG spring meeting, Bochum, 2009.

[85] G. Aielli et al. *Nucl. Instr. and Meth. A*, 456:82, 2000.

[86] D. Gonzalez-Diaz, P. Fonte, J. A. Garzon, A. Mangiarotti. *Nucl. Phys. B (Proc. Suppl.)*, 158:111, 2006.

[87] D.Gonzalez-Diaz, M. Morales et al. *Nucl. Instr. and Meth. A*, 602:713, 2009.

[88] S. Eidelman et al. Passage of particles through matter. *Phys. Lett. B*, 592:1, 2004.

[89] Sternheimer et al. *Atomic and nuclear data tables*, 30:261, 1984.

[90] E. Casarejos. Talk at R3B collaboration meeting, 2008.

[91] A. Blanco et al. *Nucl. Instr. and Meth. A*, doi:10.1016/j.nima.2010.08.068, 2010.

[92] A. Blanco et al. *Nucl. Instr. and Meth. A*, 508:70, 2003.

[93] N. Fariña. *Perfomance Analysis and Improvements of the Santiago Tracking using Simulated and Real Data in the HADES Experiment*. Diploma Thesis, USC, 2005.

[94] A. Rustamov. Momentum reconstruction with spline in hades. *Internal HADES Report, GSI*, 2003.